University of Warwick

Turbulence and Vortices in Classical and Quantum Fluids

Author:
Adam Griffin

Supervisor:
Prof Sergey Nazarenko

A thesis submitted in fulfillment of the requirements for the degree of Doctor of Philosophy in Mathematics

Mathematics Institute

September 2019

List of Figures

UNIVERSITY OF WARWICK

Abstract

Mathematics Institute

Doctor of Philosophy in Mathematics

Turbulence and Vortices in Classical and Quantum Fluids

by Adam Griffin

We present studies of different aspects of turbulence. One main focus is a superfluid turbulence. We focus on how quantised vortices interact with external potentials which could model experimental apparatus. In one chapter, we discuss the deflection of vortices and their overall interaction with vortex like impurities. Following this, the introduction of imbalance and a barrier is explored in the context of how it can be used to control regimes of turbulence in possible experiments. Here, the discussion focusses on how certain by-products of turbulence affect the dynamics of the vortices. In another related work, the affect of particles (which is common in superfluid experiments for measuring vortex position) on the motion of vortices in simple cases is explored. Although some of the systems discussed here do not directly exhibit turbulence, they are models of key components which are present in turbulent flows. Studying such structures is often referred to as a 'bottom up' approach to turbulence. Finally, we study the affect of viscosity on stationary solutions of a diffusion approximation of the Navier-Stokes equation.

List of Abbreviations

BEC	**B**ose **E**instein **C**ondensate
NLS	**N**on**L**inear **S**hrödinger (equation)
ODE	**O**rdinary **D**ifferential **E**quation
NS	**N**avier **S**tokes (equation)
1D	**1 D**imensional
2D	**2 D**imensional
3D	**3 D**imensional
JJ	**J**osephson **J**unction
TF	**T**homas **F**ermi
DNS	**D**irect **N**umerical **S**imulations
MFM	**M**agnus **F**orce **M**odel
SMFM	**S**imple **M**agnus **F**orce **M**odel
BS	**B**iot **S**avart
LIA	**L**ocal **I**nduction **A**pproximation
BKT	**B**erezinskii **K**osterlitz **T**houless (Phase transition)

Chapter 1

Introduction and Theory

I Motivation

Turbulence manifests itself all around us, from trivial things such as boiling a kettle or flushing a toilet to life threatening volcanic erruptions [123] and extra terrestrial hurricanes [125]. One of the greatest challenges facing the world today is the warming of our planet. With increased temperatures corresponding to more energy [122], it is as important as ever to be able to understand turbulence.

Definitions of turbulence vary, with some indicating that fluids with chaotic motion, with randomly changing velocities and even densities is enough to be turbulent. However, others prefer the definition of turbulence to rest on some of the key foundational discoveries of turbulence. That is, the fluid must have some scales separated by an inertial range within which there is a flux of conserved quantities. These ideas were first put forward by Richardson [91] in the 1920s and further developed by Taylor[108] in his papers building a statistical perspective of turbulence. These ideas were then furthered by Kolmogorov in his famous 1941 paper [57]. The famous poem by Richardson paints a nice picture of one of the fundamental ideas in modern turbulence. The poem:

> Big whorls have little whorls
> That feed on their velocity,
> And little whorls have lesser whorls
> And so on to viscosity.
>
> – Lewis F. Richardson

The poem depicts a direct energy cascade from large scales (big whorls) to smaller scales (lesser whorls). In turbulence, the picture can become much more complicated in terms of multiple quantities cascading in different directions [50], or even a lack of locality [35].

The above work was done for classical fluids; however, in nature there are fluids which are inherently different. Some fluids, namely, helium II (helium below 2.19K) and condensed ultra cold atomic gases (Bose-Einstein condensates) do not exhibit viscosity and can flow without dissipation. Superfluidity was first discovered by Kapitza [55] in 1938, interestingly this is the first paper in which the name 'superfluid' was used to describe fluids with such properties. Vortices are quantised in superfluids, that is, they have a fixed circulation and size. Since the conjectures of Onsager [87] and Feynman [37] in the mid 20th century, quantum vortices have attracted much interest - with progress being made analytically, numerically and experimentally. Quantum vortices appear naturally in many systems, from superfluid helium [18] to superconductors [111], neutron stars [14, 118], nonlinear optics and atomic Bose-Einstein condensates (BECs) [70]. The last context, BECs, is particularly relevant to this thesis. Research into these phenomena has revealed new physics as well as interesting analogies and points of contact with classical hydrodynamics (e.g. flows past obstacles, Karman vortex streets, vortex leapfrogging).

Vortices play a pivotal role in turbulence. The added restriction of the quantisation of the circulation along with the lack of viscosity makes quantum turbulence distinct from its classical counterpart. A cascade of energy through scales characterises turbulence. In this sense, large scales in the quantum world can correspond to large clusters of vortices. Mechanisms of energy transfer include vortex interactions and vortex annihilations (vortices of opposing polarity colliding in 2D and cancelling each others out) accompanied by the emission of sound waves.

Even with quantisation, big whorls are still possible, in this sense as a combination of many smaller whorls. It is important to understand how the quantised vortices interact with each other and external objects, and how they are involved in cascades. In 2D (two dimensional) ideal turbulence, there are two cascades at the same time, namely, enstrophy cascading to

small scales (direct cascade) and energy to large scales (inverse cascade). For large numbers of vortices, the tendency to form large-scale clusters can be understood as an inverse cascade of turbulence.

How the vortices are created is important to the type of turbulence; for instance, in a recent paper [41], the authors show that different obstacles in a fluid can create large vortex clusters or a gas of paired vortices. Vortices can be nucleated from the decay of large structures such as shock waves or solitons. How these structures decay can depend on external potentials and experimental apparatus, this is discussed in Chapter 3.

A way to observe the motion of quantised vortices in liquid helium is to place particles in the fluid. The particles are then trapped on the core and are tracked [18]. The effect of the particles on the vortices is not yet fully understood. Many questions remain unanswered on how the measurements should be interpreted. We endeavour to answer such questions by starting with a simple case and explaining the dynamics, then moving forward by increasing the complexity.

Another way to study turbulence is via the global statistics such as the energy spectra. Stationary solutions are ones with constant flux through the inertial range. That is, energy is injected at some scale and cascades at a constant rate, then exits the inertial range by being removed from the system.

II Structure

This thesis consists of two published research articles:

1. **Vortex scattering by impurities in a Bose-Einstein condensate**
   A. Griffin, G. W. Stagg, N. P. Proukakis, and C. F. Barenghi - Journal of Physics B: Atomic, Molecular and Optical 50, 115003 (2017).[44]

2. **Steady states in Leith's model of turbulence**
   V.N. Grebenev, **A. Griffin**, S.B. Medvedev and S.V. Nazarenko - Journal of Physics A: Mathematical and Theoretical 49 (36), 365501 (2016)[42]

and two articles submitted for publication:

3. **The Vortex-Particle Magnus effect**
   A. Griffin, S. Nazarenko, V. Shukla and M. Brachet
   Submitted to Physical Review A (APS)

4. **Breaking of Josephson junction oscillations and onset of quantum turbulence in Bose-Einstein condensates**
   A. Griffin, S. Nazarenko and D. Proment
   Submitted to Journal of Physics A (IOP)

We start with an introduction into some relevant background theory of superfluid turbulence, this is pertinent for papers 1, 3 and 4. This is followed by details of the numerical methods used in said papers. Finally, the foundations of the final chapter based on paper 2 are presented at the end of the introduction. In papers 1, 3 and 4, I am the lead author. In paper 2, as I am not the lead author I have placed my contributions in the main text and work that I contributed to with discussion into Appendix B for completion. Here, the abstracts of each paper are presented as a precursor to the introduction.

II.i Vortex scattering

Understanding quantum dynamics in a two-dimensional Bose-Einstein condensate (BEC) relies on understanding how vortices interact with each others microscopically and with local imperfections of the potential which confines the condensate. Within a system consisting of many vortices, the trajectory of a vortex-antivortex pair is often scattered by a third vortex, an effect previously characterised. However, the natural question remains as to how much of this effect is due to the velocity induced by this third vortex and how much is due to the density inhomogeneity which it introduces. In this work, we describe the various qualitative scenarios which occur when a vortex-antivortex pair interacts with a smooth density impurity whose profile is identical to that of a vortex but lacks the circulation around it.

II.ii Breaking of Josephson junction oscillations and onset of quantum turbulence in Bose–Einstein condensates

We analyse the formation and the dynamics of quantum turbulence in a two-dimensional Bose–Einstein condensate with a Josephson junction barrier modelled using the Gross–Pitaevskii equation. We show that a sufficiently high initial superfluid density imbalance leads to randomisation of the dynamics and generation of turbulence, namely, the formation of a quasi-1D dispersive shock consisting of a train of grey solitons that eventually breakup into chains of distinct quantised vortices of alternating vorticity followed by random turbulent flow. The Josephson junction barrier allows us to create two turbulent regimes: acoustic turbulence on one side and vortex turbulence on the other. Throughout the dynamics, a key mechanism for mixing these two regimes is the transmission of vortex dipoles through the barrier: we analyse this scattering process in terms of the barrier parameters, sound emission and vortex annihilation. Finally, we discuss how the vortex turbulence evolves for long times, presenting the optimal configurations for the density imbalance and barrier height in order to create the desired turbulent regimes which last as long as possible.

II.iii Magnus particle effect

Experimentalists use particles as tracers in liquid helium. The intrusive effects of particles on the dynamics of vortices remain poorly understood. We implement a study of how basic well understood vortex states, such as a propagating pair of oppositely signed vortices, change in the presence of particles by using a simple model based on the Magnus force. We focus on the 2D case, and compare the analytic and semi-analytic model with simulations of the Gross-Pitaevskii (GP) equation with particles modelled by dynamic external potentials. The results confirm that the Magnus force model is an effective way to approximate vortex-particle motion either with closed-form simplified solutions or with a more accurate numerically solvable ordinary differential equations (ODEs). Furthermore, we increase the

complexity of the vortex states and show that the suggested semi-analytical model remains robust in capturing the dynamics observed in the GP simulations.

II.iv Leith model of turbulence

We present a comprehensive study and full classification of the stationary solutions in Leith's model of turbulence with a generalised viscosity. Three typical types of boundary value problems are considered: problem 1 (2) with a finite positive value of the spectrum at the left (right) and zero at the right (left) boundaries of a wave number range, and problem (3) with finite positive values of the spectrum at both boundaries. Formulations of these problems and analysis of existence of their solutions are based on a phase-space analysis of orbits of the underlying dynamical system. One of the two fixed points of the underlying dynamical system is found to correspond to a "sharp front" where the energy flux and the spectrum vanish at the same wave number. The other fixed point corresponds to the only *exact* power-law solution—the so-called dissipative scaling solution. The roles of the Kolmogorov, dissipative and thermodynamic scaling, as well as of sharp front solutions, are discussed.

III Non-Linear Schrödinger Equation

To study turbulence from the 'bottom up' we introduce an equation which can be used as a model for superfluids. The Non-Linear Schrödinger (NLS) equation is usually presented in dimensionless form and can have positive or negative (focusing or defocussing) interaction terms. The NLS equation for the evolution of the complex scalar wave function $\psi(\mathbf{r}, t) \in \mathbb{C}$:

$$i\frac{\partial}{\partial t}\psi\left(\mathbf{r}, t\right) = \left(-\nabla^2 + s\left|\psi\left(\mathbf{r}, t\right)\right|^2\right)\psi\left(\mathbf{r}, t\right), \tag{1.1}$$

where the parameter s here prescribes the focusing or defocussing nature of the equation. This equation is a universal model and encapsulates many

different areas of physics, such as optics [83], water waves [126] and Bose-Einstein condensates [45, 89]. In this report we restrict ourselves to up to 3 spatial dimensions such that $\mathbf{r} \in \mathcal{D} \in \mathbb{R}^d$ where $d = 3$ and $t \in \mathbb{R}^+$, where $\mathcal{D}$ is some domain prescribed with a suitable boundary.

The application to fluid dynamics of this equation can best be demonstrated via the Madelung transformation. The Madelung transformation was first used to show how the probability clouds describing positions and momenta of particles have fluid like properties in the Schrödinger equation.

III.i Madelung Transformation

The wave function can be expressed by its density $\rho(\mathbf{r}, t)$ and phase $\theta(\mathbf{r}, t)$;

$$\psi(\mathbf{r}, t) = \sqrt{\rho(\mathbf{r}, t)} e^{i\theta(\mathbf{r}, t)}. \tag{1.2}$$

The fluid velocity can then be written as,

$$\mathbf{v}(\mathbf{r}, t) = 2\nabla\theta(\mathbf{r}, t). \tag{1.3}$$

Via substitution of the above representation of the wave function into the NLS equation and separation of real and complex terms, we arrive at two familiar equations (calculation shown in section I in appendix A). The equation found by consideration of the real part is the continuity equation,

$$\frac{\partial \rho}{\partial t} = -\nabla \cdot (\rho \mathbf{v}). \tag{1.4}$$

This equation represents the conservation of particle number density within the NLS equation. The equation found by considering the imaginary parts is given by,

$$\frac{\partial \mathbf{v}}{\partial t} + (\mathbf{v} \cdot \nabla)\mathbf{v} = s\frac{\nabla \rho^2}{\rho} + 2\nabla \frac{\nabla^2 \sqrt{\rho}}{\sqrt{\rho}}. \tag{1.5}$$

This is very similar to Euler's equation with a differing pressure term given by,

$$\frac{\nabla p}{\rho} = s\frac{\nabla \rho^2}{\rho} + 2\nabla\frac{\nabla^2\sqrt{\rho}}{\sqrt{\rho}}. \tag{1.6}$$

The first term is similar to the adiabatic pressure $p = -s\rho^2$ found in classical ideal fluids. The second term corresponds to the quantum pressure. The difference of the quantum pressure term is an important one, as the pressure is not constant the fluid will be compressible therefore the flow will host coherent structures such as sound waves.

As the wave function has a corresponding velocity in equation (1.3), one can calculate the circulation. Substitution of (1.3) into the equation for circulation, one will arrive at,

$$\Gamma = \oint_{\mathcal{L}} \nabla\theta \cdot d\mathcal{L}. \tag{1.7}$$

Note here that if we let the value of ψ at the beginning of the closed line integral to be ψ_0 then at the end point of the line integral, ψ_f, we obtain the expression $\psi_f = \psi_0 e^{i\Gamma}$. However, the wave function is single valued implying that $\psi_f = \psi_0$ thus Γ must be equal to some multiple of 2π. This is equivalent to:

$$\oint_{\mathcal{L}} \nabla\theta \cdot d\mathcal{L} = 4\pi q, \tag{1.8}$$

where q is an integer. For a homogeneous condensate $q = 0$, for $q \neq 0$ there must be a phase singularity in the flow. The phase singularity is present when considering the flow around a vortex. This causes the circulation to be quantised where q is the charge of the vortex.

The mass of fluid within the system is conserved (calculation shown in section II in appendix A) under evolution of (1.1),

$$N = \int_{\mathcal{D}} |\psi(\mathbf{r}, t)|^2 d\mathbf{r}. \tag{1.9}$$

Total Momentum, $\mathbf{P}$, is also conserved,

$$\mathbf{P} = -\frac{i}{2}\int_{\mathcal{D}} \left[\psi^* \nabla\psi - \psi\nabla\psi^*\right] d\mathbf{r}. \tag{1.10}$$

It can also be shown that the total energy is conserved in the system (calculation shown in Section II in Appendix A) and that the system can be represented by the following Hamiltonian,

$$H = \int_{\mathcal{D}} \left[|\nabla\psi|^2 + \frac{s}{2}|\psi|^4\right] d\mathbf{r}. \tag{1.11}$$

The first term in (1.11) can be decomposed by using the Madelung transform (1.2) into the kinetic energy and the so called quantum energy

$$|\nabla\psi|^2 = \rho|\nabla\theta|^2 + |\nabla\sqrt{\rho}| = \varepsilon_{kin} + \varepsilon_{quant}. \tag{1.12}$$

Further, the kinetic energy can be decomposed into divergence and curl free parts by using the Helmholtz decomposition. To do this practically we make use of the Fourier transform of the density flux $\hat{\mathbf{j}}$, we use the following formula from [86] for the kinetic compressible energy:

$$E^c_{kin} = \int_{\mathcal{D}} \left(\sum_\alpha \left(\sum_\beta \frac{k_\alpha k_\beta}{k^2}\hat{j}_\beta\right)^2\right)^{1/2} d\mathbf{k} \tag{1.13}$$

where $\alpha = x, y$ and $\beta = x, y$. From this the incompressible energy can be calculated as the difference of the total energy and the kinetic compressible energy.

In the field of condensed gases a re-scaled version of (1.1) is known as the the Gross Pitaevskii (GP) equation [45, 89]. The GP equation describes a Bose-Einstein condensate (BEC) formed in a weakly interacting dilute Bose gas at zero temperature. The GP equation is given by

$$i\hbar\frac{\partial}{\partial t}\psi(\mathbf{r},t) = \left(-\frac{\hbar^2}{2m}\nabla^2 + V_{\text{ext}}(\mathbf{r}) + g|\psi(\mathbf{r},t)|^2\right)\psi(\mathbf{r},t). \tag{1.14}$$

Where $\psi(\mathbf{r},t) \in \mathbb{C}$ is a complex scalar wave function, here $\mathbf{r} \in \mathbb{R}^3$, $\hbar$ is the reduced Planck's constant, m is the mass of a boson and V_{ext} is some spatially dependent confining potential. The magnitude of the non-linear interaction g, is given by

$$g = \frac{4\pi\hbar^2 a}{m}, \tag{1.15}$$

for the scattering length a which characterises the repulsive interaction between bosons. The equation is the defocussing ($s = 1$) NLS with the scaling

$$x = \xi x' \qquad t = \frac{\hbar}{\mu}t' \qquad \psi = \psi_0\psi' \qquad V_{\text{ext}} = V'\mu, \tag{1.16}$$

where

$$\xi = \frac{\hbar}{\sqrt{2mg\rho_0}}, \tag{1.17}$$

is the healing length which is the length scale where the repulsion and diffusion balance within (1.14). The chemical potential μ is the change in energy to a condensate when the number of particles change. Here, ψ_0 is the solution to the steady infinite condensate and $\rho_0 = |\psi_0|^2$. The circulation is also rescaled, in these units it is quantised to multiples of h/m.

It is useful to consider steady solutions to this equation, that is solutions independent of time. The time independent GP equation can be found by considering the evolution of the state,

$$\psi(\mathbf{r},t) = \psi_s(\mathbf{r})\, e^{-\frac{i\mu t}{\hbar}}, \tag{1.18}$$

where ψ_s is a time independent solution. Applying this substitution to equation (1.14) we find the time independent GP equation:

$$\mu\psi_s(\mathbf{r}) = \left(-\frac{\hbar^2\nabla^2}{2m} + V_{ext}(\mathbf{r}) + g\,|\psi_s(\mathbf{r})|^2\right)\psi_s(\mathbf{r})\,. \tag{1.19}$$

III.ii Uniform Solution

One of the simplest solutions can be found by considering the one dimensional time independent GP Equation and for a uniform density such that $\frac{\partial^2\psi}{\partial x^2} = 0$ and no external potential, $V_{\text{ext}} = 0$, then the time independent GP equation (1.19) becomes,

$$g\left|\psi\right|^2\psi = \mu\psi. \tag{1.20}$$

By rearranging,

$$\psi\left(x\right) = \psi_0 = \sqrt{\frac{\mu}{g}}. \tag{1.21}$$

It is simpler to write this in terms of the real valued density,

$$\rho\left(x\right) = \rho_0 = \psi_0^2 = \frac{\mu}{g}. \tag{1.22}$$

For this case the chemical potential, interaction strength and density are trivially linked and the density is constant in space.

III.iii Semi-Infinite Trap

Consider an infinite one dimensional line with a potential defined as,

$$V_{ext}\left(x\right) = \infty \quad \text{when} \quad x < 0 \qquad V_{ext}\left(x\right) = 0 \quad \text{when} \quad x \geq 0 \tag{1.23}$$

The region $x < 0$ is not accessible to the wavefunction due to the potential at the origin. Thus this is equivalent to the boundary condition $\psi\left(0\right) = 0$, We also specify for the other boundary that $\psi\left(x\right) = \psi_0 = \sqrt{\frac{\mu}{g}}$ as $x \to \infty$ due to the limiting case where the wave function will not interact with the boundary the wave function is required to become the solution in an infinite plane as in (1.22). We once again consider the time independent Gross-Pitaevskii equation in the region of zero external potential. Applying

these conditions to equation (1.19), one arrives at,

$$\mu\psi = \left(-\frac{\hbar^2}{2m}\frac{\partial^2}{\partial x^2} + g\left|\psi\right|^2\right)\psi. \tag{1.24}$$

Now using the second constraint we rearrange to find $\mu = \psi_0^2 g$, substituting this into the above equation gives

$$\frac{\partial^2\psi}{\partial x^2} = -\frac{2mg}{\hbar^2}\left(\psi_0^2 - \left|\psi\right|^2\right)\psi, \tag{1.25}$$

which we can solve to give

$$\psi\left(x\right) = \psi_0 \tanh\left(\frac{x}{\xi}\right). \tag{1.26}$$

Here we see clearly how the healing length ψ is a scale at which the wave-function heals to a potential or boundary. This solution also motivates the choice of the tanh function in Chapter 4.

IV Numerical Methods

Here we present a brief overview of the numerical methods used. We use finite difference and pseudo-spectral methods.

IV.i Finite Difference Method

Finite difference is a method for numerically calculating derivatives. The method relies on approximating derivatives at a particular point in space and time by considering nearby points at well defined finite distances. The derivation is a simple exercise in which you take advantage of the cancellations of the forward and backward Taylor expansions. To begin, prescribe a spatial discretisation, for one dimension this is x, into N_x points and temporal domain, t, into N_t points. The points are separated by small finite increments Δx and Δt for space and time respectively. We denote the field at position x_j and time t_j as $\psi_{i,j} = \psi\left(x_j, t_j\right)$. Within the scheme, the two

important derivatives for solving the GP equation are given by:

$$\frac{\partial \psi_{i,j}}{\partial t} = \frac{\psi_{i,j+1} - \psi_{i,j-1}}{2\Delta t} + \mathcal{O}\left(\Delta t\right) \tag{1.27}$$

$$\frac{\partial^2 \psi_{i,j}}{\partial x^2} = \frac{\psi_{i+1,j} - 2\psi_{i,j} + \psi_{i-1,j}}{\Delta x^2} + \mathcal{O}\left(\Delta x^2\right). \tag{1.28}$$

The method also has a stability condition which is $\Delta t/(\Delta x^2) < 1/2$ in 1D and $\Delta t/(\Delta x^2) + \Delta t/(\Delta y^2) < 1/2$ in 2D. To improve the stability and accuracy of the method we can use higher order methods. In particular the fourth order second partial derivative can be written:

$$\frac{\partial^2 \psi_{i,j}}{\partial x^2} = \frac{-\frac{1}{12}\psi_{i+2,j} + \frac{4}{3}\psi_{i+1,j} - \frac{5}{2}\psi_{i,j} + \frac{4}{3}\psi_{i-1,j} - \frac{1}{12}\psi_{i-2,j}}{\Delta x^2} + \mathcal{O}\left(\Delta x^4\right) \tag{1.29}$$

IV.ii The Runge-Kutta Method

The Runge-Kutta 4th order method is used for time-stepping because of its relative ease of use and its high stability. The method works by considering the approximate derivatives at different points and uses symmetry to cancel error terms from the approximations to increase the order of the truncation error. The truncation error of the Runge-Kutta method is of the order $\mathcal{O}\left(\Delta t^5\right)$ therefore the total error for multiple steps is of order $\mathcal{O}\left(\Delta t^4\right)$.

$$\begin{aligned}
\psi_{i+1} &= \psi_i + \frac{1}{6}(k_1 + 2k_2 + 2k_3 + k_4) \\
k_1 &= hf(t, \psi_n) \\
k_2 &= hf(t + \Delta t/2, \psi_n + k_1/2) \\
k_3 &= hf(t + \Delta t/2, \psi_n + k_2/2) \\
k_4 &= hf(t + \Delta t, \psi_n + k_3)
\end{aligned}$$

Where f represents the dimensionless version of the right hand side of (1.14).

IV.iii Imaginary Time Propagation

To study the dynamics of the GP equation, it is often useful to find a ground state given the boundary conditions and external potentials. This state will minimise the kinetic energy, allowing studies with small perturbations such as the addition of vortices or change in potential. To find such a configuration with minimal energy we use a numerical method called Imaginary time propagation [103, 5]. To gain insight into this method, consider wave function, $\psi(x,t)$, in one spatial dimension expressed as a superposition of eigenstates ψ_n with corresponding eigenenergies E_n given by

$$\psi\left(x,t\right)=\sum_{n=1}^{\infty}a_n\psi_n\left(x\right)e^{-\frac{iE_n}{\hbar}t}. \tag{1.30}$$

In the above equation a_n are coefficients of the orthonormal basis functions, such that any initial data can be expressed by choosing suitable coefficients. We can now order the eigenenergies with the condition that $E_n < E_{n+1}$, which implies that E_0 is the ground state energy. To proceed we consider the substitution $t=-i\tau$, which transforms the arbitrary state into the form

$$\psi\left(x,\tau\right)=\sum_{n=1}^{\infty}a_n\psi_n\left(x\right)e^{-\frac{E_n}{\hbar}\tau}. \tag{1.31}$$

The above equation is decreasing in τ and will tend to zero as τ increases. If we numerically enforce conservation of density, $|\psi|^2$, then we ψ no longer can go to zero, instead it will tend to the wavefunction that minimises the energy. To explain this consider Equation (1.31) which can be re-written, by taking the exponential of the lowest eigenenergy outside the sum, as

$$\psi\left(x,\tau\right)=e^{-\frac{E_0}{\hbar}\tau}\left[a_0\psi_0+a_1\psi_1\left(x\right)e^{\frac{(E_0-E_1)}{\hbar}\tau}+a_2\psi_2\left(x\right)e^{\frac{(E_0-E_2)}{\hbar}\tau}+\cdots\right]. \tag{1.32}$$

It is now clear that any term inside the bracket of the form,

$$a_n \psi_n(x)\, e^{\frac{(E_0 - E_n)}{\hbar}\tau}, \tag{1.33}$$

will tend to zero as τ increases due to $(E_0 - E_n) < 0$ for $E_n > 0$. The speed of convergence to zero is increasing in n, thus the ground state will have the slowest convergence. This fact along with the renormalisation imposing a constant density shows us that as τ increases ψ will tend to the lowest energy state. By using the numerical methods discussed in the above sections with the substitution of $t_p = -i\tau_p$ we now have a method for finding the ground state.

IV.iv Model and methods for particles

A modification of the dimensionless GP equation (1.14) will allow us to study particles. We allow the particle to act on the fluid as any external potential. The fluid also acts on the particle by changing its position due to a force calculated from the pressure exerted on the particle due to the density of the surrounding fluid. We present the equation for the wavefunction ψ:

$$i\frac{\partial \psi}{\partial t} = -\frac{1}{2}\nabla^2\psi - \psi + |\psi|^2\psi + \sum_{i=1}^{\mathcal{N}_0} V_{\mathcal{P}}(\mathbf{r} - \mathbf{q}_i)\psi; \tag{1.34}$$

which is coupled with a particle which follows Newtonian mechanics, with

$$m_0 \ddot{\mathbf{q}}_i = \mathbf{f}_{0,i} + \mathbf{f}_{SR,i}, \tag{1.35}$$

where

$$\mathbf{f}_{o,i} = \int_{\mathcal{D}} |\psi|^2 \nabla V_{\mathcal{P}}\, d\mathbf{r}, \tag{1.36}$$

and $\mathbf{f}_{SR,i}$ models the short-range repulsion between the particles and only become significant when particles are close enough to collide. The choice of the function $V_{\mathcal{P}}$ dictates the shape and penetrability of the particle. For our studies we choose a Gaussian particle, which corresponds to a disk shape particle with a small, but not insignificant boundary layer. More details are given in Chapter 4.

The total energy of this system in the absence of any external force is conserved and given by

$$E = E_{GP} + E_{\mathrm{P}} \tag{1.37}$$

is conserved; here, E_{GP}, the energy of the superfluid field calculated by (1.11) with the correct potential and scales, E_P is the total energy of the particles, which can be further separated into contributions from the kinetic energy and potential energy from the short range repulsion $E_P = E_{Pkin} + E_{\mathrm{SR}}$. The GP energy is the same as (1.11) with the correct potential and scales and is defined as

$$E_{\mathrm{GP}} = \frac{1}{\mathcal{A}} \int_{\mathcal{A}} \left[\frac{1}{2}|\nabla\psi|^2 + \frac{1}{2}\Big(|\psi|^2 - 1\Big)^2 \right. \tag{1.38a}$$

$$\left. + \sum\nolimits_{\mathrm{i}=1}^{\mathcal{N}_{\mathrm{o}}} V_{\mathcal{P}}(\mathbf{r} - \mathbf{q}_i)|\psi|^2 \right] d\mathbf{r}; \tag{1.38b}$$

$$E_{\mathrm{Pkin}} = \frac{1}{\mathcal{A}} \sum\nolimits_{\mathrm{i}=1} \frac{1}{2} m_{\mathrm{o}} \dot{\mathbf{q}}_i^2; \tag{1.38c}$$

$$E_{\mathrm{SR}} = \frac{1}{\mathcal{A}} \sum\nolimits_{\mathrm{i,j,i}\neq\mathrm{j}}^{\mathcal{N}_{\mathrm{o}},\mathcal{N}_{\mathrm{o}}} \frac{\Delta_E r_{\mathrm{SR}}^{1/2}}{|q_i - q_j|^{1/2}}. \tag{1.38d}$$

In this model Eqs. (1.34)-(1.35), the total momentum is conserved

$$\mathbf{P}(t) = \int_{\mathcal{D}} \frac{i}{2}(\psi^*\nabla\psi - \psi\nabla\psi^*)\, d\mathbf{r} + \sum\nolimits_{\mathrm{i}=1}^{\mathcal{N}_{\mathrm{o}}} m_{\mathrm{o}} \dot{\mathbf{q}}_i \tag{1.39}$$

The total density is still also conserved

$$N = \int_{\mathcal{D}} |\psi|^2\, d\mathbf{r}. \tag{1.40}$$

We model the particles by specifying the potential $V_{\mathcal{P}}$ which is discussed in Chapter 4. We use the pseudo-spectral method for calculating the spatial derivatives. We can show how this method works by focusing on the Laplacian term in equation (1.34),

$$\frac{\partial\psi}{\partial t} = i\nabla^2\psi. \tag{1.41}$$

By using the Fourier transform of ψ:

$$\hat{\psi} = \int_{\mathcal{D}} \psi e^{-i\mathbf{k}\cdot\mathbf{x}} d\mathbf{x} \tag{1.42}$$

and taking the Fourier transform of (1.41) we find

$$\frac{\partial \hat{\psi}}{\partial t} = -ik^2\hat{\psi} \tag{1.43}$$

which has a solution if we integrate for t:

$$\hat{\psi}(t) = \hat{\psi}_0 e^{-ik^2 t}. \tag{1.44}$$

Thus to find the solution we can use the inverse Fourier transform:

$$\psi = \int_{\mathcal{D}_k} \hat{\psi} e^{i\mathbf{k}\cdot\mathbf{x}} d\mathbf{k}. \tag{1.45}$$

To deal with the nonlinear term plus any external potential term we can consider the equation:

$$\frac{\partial \psi}{\partial t} = IFT[k^2[FT[\psi]]] - i|\psi|^2\psi - i\psi - i\sum_{i=1}^{\mathcal{N}_0} V_{\mathcal{P}}(\mathbf{r} - \mathbf{q}_i)\psi. \tag{1.46}$$

where $FT[\cdot]$ indicates the Fourier transform and $IFT[\cdot]$ its inverse. Now we can use the Runge-Kutta method discussed in IV.ii to step in time.

When performing the Fourier transform numerically dealiasing errors can arise. We follow Ref. [59] and use the standard 2/3-dealiasing rule, with $k_{\max} = 2/3 \times N_c/2$ in the Galerkin projector $\mathcal{P}_G$

$$\mathcal{P}_G[\hat{\psi}(\mathbf{k})] = \mathcal{H}(k_{\max} - |\mathbf{k}|)\hat{\psi}(\mathbf{k}). \tag{1.47}$$

Here , $\mathcal{H}(\cdot)$ the Heaviside function. The two thirds rule arises from requiring that interactions between waves that introduce waves outside of the available modes are not re introduced as unphysical waves due to the DFT. If we have two waves with wave numbers k_1 and k_2 such that $k_1 + k_2 > N_c/2$, the DFT will then assign the amplitude of the wave resulting from

their interaction to the mode $k_1 + k_2 - N_c$. To counter this we choose a sub-domain in k in which all amplitudes are set to zero. We chose that $k_1 + k_2 - N < -k_{max} < N_c$, for all $k_1, k_2 \in [-k_{max}, k_{max}]$. The extremal values are then required to satisfy $2k_{max} - N_c < -k_{max}$. Thus, we arrive at the 2/3-dealiasing rule, with$k_{\max} = 2/3 \times N_c/2$.

We first apply $\mathcal{P}_G$ on $|\psi|^2$ and then again on $\mathcal{P}_G[|\psi|^2]\psi$. This ensures global momentum conservation in our simulations. This is essential for the study of collisions between particles [97] and their interactions with the field ψ. Thus, our Galerkin-truncated GPE becomes

$$\begin{aligned} i\frac{\partial\psi(\mathbf{r},t)}{\partial t} = \mathcal{P}_G\Bigg[&-IFT[k^2[FT[\psi(\mathbf{r},t)]]] + \mathcal{P}_G[|\psi|^2]\psi(\mathbf{r},t) \\ &- 1 + \sum\nolimits_{\mathrm{i}=1}^{\mathcal{N}_\mathrm{o}} V_\mathcal{P}(\mathbf{r}-\mathbf{q}_i)\psi(\mathbf{r},t)\Bigg]. \end{aligned} \tag{1.48}$$

Given our Galerkin-truncation scheme, we can write the force acting on the particle as

$$\begin{aligned} \mathbf{f}_{\mathrm{o},i} = -\int_\mathcal{A}\Big[&\psi^*\mathcal{P}_G[V_\mathcal{P}(\mathbf{r}-\mathbf{q}_i)\nabla\psi] \\ &+ \psi\mathcal{P}_G[V_\mathcal{P}(\mathbf{r}-\mathbf{q}_i)\nabla\psi^*]\Big]d^2x. \end{aligned} \tag{1.49}$$

V Derivation of Leith Model

In this section we follow the original paper of Leith [64] in his derivation of a simplistic model for the diffusion of energy in the Navier-Stokes (NS) equation. This is a precursor to Chapter 5, in which we analyse the stationary solutions when the viscosity is generalised. We start by defining one of the fundamental quantities of turbulence, the two point correlation function of the velocity:

$$\langle \mathbf{u}(\mathbf{x})\cdot\mathbf{u}(\mathbf{x}+\mathbf{r})\rangle = \frac{1}{2}\int_{\mathbb{R}^3}\mathbf{u}(\mathbf{x})\cdot\mathbf{u}(\mathbf{x}+\mathbf{r})d\mathbf{x}. \tag{1.50}$$

To find an evolution equation for this quantity we take the Navier-Stokes equation,

$$\frac{\partial \mathbf{u}}{\partial t} + (\mathbf{u} \cdot \nabla)\mathbf{u} - \nu \nabla^2 \mathbf{u} = 0 \tag{1.51}$$

where $\mathbf{u}$ is the velocity of a fluid. We also chose the velocity to be divergence free,

$$\nabla \cdot \mathbf{u} = 0 \tag{1.52}$$

such that the density of the fluid is conserved. The final terms corresponds to dissipation, with ν being the kinematic viscosity. By taking the dot product of (1.51) with the velocity at some point a distance $\mathbf{r}$, $\mathbf{u}(\mathbf{x}+\mathbf{r})$, performing the averaging and using the fact the velocity is divergence free we have:

$$\frac{1}{2}\frac{\partial \langle \mathbf{u}(\mathbf{x}) \cdot \mathbf{u}(\mathbf{x}+\mathbf{r}) \rangle}{\partial t} + A(\mathbf{u}) - \frac{1}{2}\nu \nabla^2 (\langle \mathbf{u}(\mathbf{x}) \cdot \mathbf{u}(\mathbf{x}+\mathbf{r}) \rangle) = 0 \tag{1.53}$$

where $A(\mathbf{u})$ encapsulates the average of the non-linear term in (1.51), we omit the details of this term as the proposed model will approximate the effect of this term as diffusion in $k-$space rather than the complicated non-local convolution. Now we define the 3D energy spectrum as follows,

$$E^{(3D)}(\mathbf{k}) = \frac{1}{2}\int_{\mathbb{R}^3} \langle \mathbf{u}(\mathbf{x}) \cdot \mathbf{u}(\mathbf{x}+\mathbf{r}) \rangle e^{-i\mathbf{k}\cdot\mathbf{r}} d\mathbf{r}. \tag{1.54}$$

The energy spectrum is a focus of the study of turbulence. It shows how the energy is distributed over different length scales. We aim to approximate the dynamics of this quantity due to the evolution of (1.51). We note that if the turbulence is isotropic then the dependence is only on $k = |\mathbf{k}|$, also all the information can be expressed in a 1D energy spectrum, given by, $E^{(1D)}(k) = 4\pi k^2 E^{(3D)}(k)$. Thus we can define the kinetic energy spectrum as

$$\frac{\langle u^2 \rangle}{2} = \int_{\mathcal{D}} E^{(1D)}(k) dk \tag{1.55}$$

By taking the Fourier transform of (1.53) we have:

$$\frac{\partial E^{(3D)}(\mathbf{k}, t)}{\partial t} + \Im(\mathbf{k}, t) - \nu k^2 E^{(3D)}(\mathbf{k}, t) = 0 \tag{1.56}$$

Where here $\Im$ accounts for the distribution of energy amongst the wave numbers due to non-linear interactions. The term $\Im$ should conserve energy thus we define

$$\Im = -\nabla \cdot \mathbf{F} \tag{1.57}$$

such that $\mathbf{F}$ is the flux vector of energy. We assume compactness in k-space, that is, for some cut-off k_c $\mathbf{F}(k > k_c) = 0$. If we restrict ourselves to isotropy and the radial component of $\mathbf{F}$ is $\mathcal{F}$ then (1.56) can be written:

$$\frac{\partial E^{(1D)}(k, t)}{\partial t} = -k^{-2} \frac{\partial (k^2 \mathcal{F}(k))}{\partial k} - \nu k^2 E^{(1D)}(k) \tag{1.58}$$

The restriction of isotropy allows us to integrate radially and azimuthally such that the total energy and flux for each shell corresponding to the wave number k will be given by:

$$E^{(1D)}(k) = 4\pi k^2 E^{(3D)}(k) \tag{1.59}$$

$$F = 4\pi k^2 \mathcal{F} \tag{1.60}$$

now,

$$\frac{\partial E^{(1D)}}{\partial t} = -k^{-2}\frac{\partial k^2 F}{\partial k} - \nu k^2 E^{(1D)} \tag{1.61}$$

To proceed Leith applied the ideas of Kolmogorov which has physical intuition and experimental evidence. The idea was that the flux in k must be local, such that the value of the energy flux $\varepsilon(k)$ is influenced mainly by the values at points close to k. To formulate this we introduce what is referred to as the diffusion approximation:

$$\mathcal{F} = -D\frac{\partial Q}{\partial k} \tag{1.62}$$

Where D is a diffusion coefficient and Q the diffusion potential, both of which can be functions that vary in k-space and as a function of energy density.

Dimensional arguments can show that the product DQ has dimension $k^{9/2}\varepsilon^{3/2}$, the dimensions we need to consider are,

$$[DQ] = \left[\frac{\partial E^{(1D)}}{\partial t}k^3\right] = L^3T^{-3}L^{-3} = T^{-3}, \tag{1.63}$$

$$[\varepsilon] = L^2T^{-2}, \tag{1.64}$$

$$[E^{(1D)}] = L^3T^{-2}. \tag{1.65}$$

Using these dimensions, and equation (1.61) we can determine the dimension of the product DQ:

$$[DQ] = [\epsilon]^\alpha[k^{-1}]^\beta \tag{1.66}$$

$$[T^{-3}] = [L^3T^{-2}]^\alpha[k^{-1}]^\beta \tag{1.67}$$

$$\alpha = 3/2 \tag{1.68}$$

$$\beta = 9/2. \tag{1.69}$$

Thus to find the dimension of D and Q separately, we can write:

$$D = \beta k^{9/2-m}\varepsilon^{n} \tag{1.70}$$

$$Q = k^{m}\varepsilon^{3/2-n}, \tag{1.71}$$

if $n = 3/2$ this case is known as the Kovasznay's approximation which is a simpler model, we choose $n \neq 3/2$ then

$$\mathcal{F} = -\beta\left(\frac{3}{2} - n\right)k^{\frac{11}{2}}\left[\frac{m}{\frac{3}{2}-n}\varepsilon^{\frac{3}{2}} + \frac{3}{2}k\varepsilon^{\frac{1}{2}}\frac{\partial\varepsilon}{\partial k}\right] \tag{1.72}$$

where $E = E^{(1D)}$ here, the notation is contracted for simplicity. As the factor of n coincides with multiplication of the constants β and m we lose no generality in choosing $n = 0$, as this choice just rescales the constants. The choice of m can be made on physical grounds. If we consider an isolated region of k- space where the energy distribution is constant every where and there is no flux, then the correct solution corresponds to $m = 0$ to cancel the first term in the bracket in (1.72). Thus substituting (1.72) into (1.61) we arrive at

$$\frac{\partial E}{\partial t} = \beta\frac{\partial}{\partial k}\left[k^{\frac{11}{2}}E^{\frac{1}{2}}\frac{\partial k^{-2}E}{\partial k}\right] - \nu k^{2}E, \tag{1.73}$$

which is Leith's model of turbulence. The term β can be chosen to fit numerical observations. Equation (1.73) approximates the evolution of the energy spectrum due to the Navier-Stokes equation. The equation differs from NS due to the treatment of the nonlinear term. In the Leith model we have replaced a non-local convolution in $k-$space with a local diffusion type nonlinearity. The equation is especially useful for studying the effects of this type of locality in turbulence.

Chapter 2

Vortex Scattering via impurities

I Introduction

In a recent paper [102], Smirnov & Smirnov have studied the scattering of two-dimensional (2D) vortex-antivortex pairs and solitons by a single quantum vortex in a homogeneous atomic Bose-Einstein condensate. They found that the pair is scattered over large angles radiating sound waves, in agreement with earlier calculations [12]. This scattering process is important because it lies at the heart of the dynamics of 2D quantum turbulence, a problem which is currently attracting experimental and theoretical attention [79, 82, 62, 105, 26, 46]. Our understanding of the turbulent motion of many interacting vortices is based on recognizing the most elementary interactions, such as the interaction of a vortex with another vortex of the same or opposite sign (resulting respectively in rotational or translation motion of the pair). Similarly, we would like to recognize the possible elementary interactions between a vortex and a large density perturbation induced by the dynamics of vortices by external means. It is well-known that a quantum vortex in a Bose-Einstein condensate is a hole of zero density around which the phase changes by 2π. The natural question is whether the incoming vortex-antivortex pair would be scattered (and if so, by which amount) by a density perturbation alone (without the circulation around it), as density gradients induce a Magnus force [72, 36] which deflects the pair. To answer this question, we have performed numerical simulations of vortex-antivortex pairs travelling towards a fixed target in the form of a density perturbation (hereafter referred to as an 'impurity') and whose depth and size is similar

to the depth and size of a quantum vortex (but without the circulation). Here we report about the significant scattering induced by the impurity, and compare it with the scattering induced by a target in the form of a vortex.

For simplicity we consider a homogeneous condensate at zero temperature, and aim at identifying the various qualitative scenarios which are possible (quantitative predictions of vortex trajectories in a harmonically trapped condensate require more specific calculations which depend on the actual physical parameters and geometry, and are outside the scope of this work). A better physical understanding of the scattering which imperfections induce on vortices is generally useful (although in general imperfections may not be as symmetric as we describe them here). Our results are also relevant to the manipulation of vortices using optical potentials generated by laser beams [29, 107].

II Model

We simulate the dimensionless version of the GP equation (1.1) in a 2D domain $-L \leq x, y \leq L$. The initial condition at $t = 0$, schematically described in Fig. 2.1, is a vortex-antivortex pair, consisting of a left (clockwise) vortex and a right (anticlockwise) vortex initially placed respectively at positions $x_L(0)$, $y_L(0)$ and $x_R(0)$, $y_R(0)$. We call $d = |x_L(0) - x_R(0)|$ the initial distance between the vortices of the pair. The vortex-antivortex pair travels along the negative y direction with impact parameter $h = (x_R(0)+x_L(0))/2$ towards a fixed density perturbation (or impurity) held at $x_I = y_I = 0$. The impurity is represented by the (dimensionless) external potential $V(x, y) = \sum_{j=1}^{4} A_j e^{-R^2/\sigma_j^2}$ where $R^2 = ((x - x_I)^2 + (y - y_I)^2)$.

With a suitable choice of parameters A_j[1] solving the time-independent GPE without the vortex-antivortex pair, the density profile of the impurity approximately matches the profile of a singly-charged vortex at x_I, y_I in the homogeneous condensate.

To quantify the scattering, we measure the deflection angle θ of the antivortex away from its initial trajectory, but in some cases (for example if the

[1]Parameters: $A_1 = 14$; $A_2 = 0.22$; $A_3 = 0.15$; $A_4 = 0.05$; $\sigma_1 = 0.4$; $\sigma_2 = 1.25$; $\sigma_3 = 2.5$; $\sigma_4 = 4.75$.

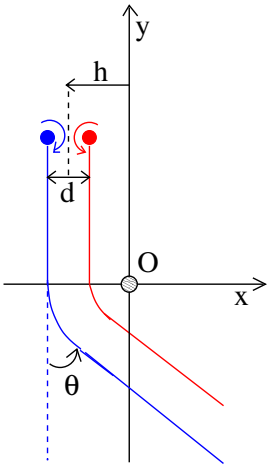

FIGURE 2.1: Schematic representation of the scattering configuration. Initially, the vortex (red, right) and the antivortex (blue, left) are separated by the distance d; the impact parameter is h (here $h < 0$). The vortex-antivortex pair travels in the negative y-direction towards the impurity (or a third vortex) at the origin. The scattering angle is θ (here $\theta > 0$).

vortex-antivortex pair breaks up) a different description of the interaction is necessary.

We choose $L = 156.6\xi$ and impose $\psi = 0$ on the boundaries. We use a 1024^2 grid, corresponding to the (dimensionless) spatial discretization $\Delta x = \Delta y = 0.3\xi$. Time-stepping is performed using the 4th-order Runge-Kutta scheme; the typical (dimensionless) time step is $\Delta t = 0.01$. During typical evolutions the total energy is conserved within 0.003 %. The calculations were repeated in a 512^2 box with size $L = 76.65\xi$ resulting in the same qualitative scattering scenarios which we describe in the next section. Variations in the deflection angles resulting from discretization errors and from sound waves reflected from the boundaries are small (of the order of one percent); the trapping scenario appears more sensitive to perturbations. On the other hand, in the experiments, 2D vortex configurations typically contain significant sound waves besides thermal noise.

III Scattering scenarios

In all calculations we choose initial y-coordinates $y_L(0) = y_R(0) = 65\xi$, sufficiently away from the impurity; the initial x-coordinates, $x_L(0)$ and $x_R(0)$, vary from case to case, as we change the impact parameter h and the vortex separation d. We have identified three typical scenarios:

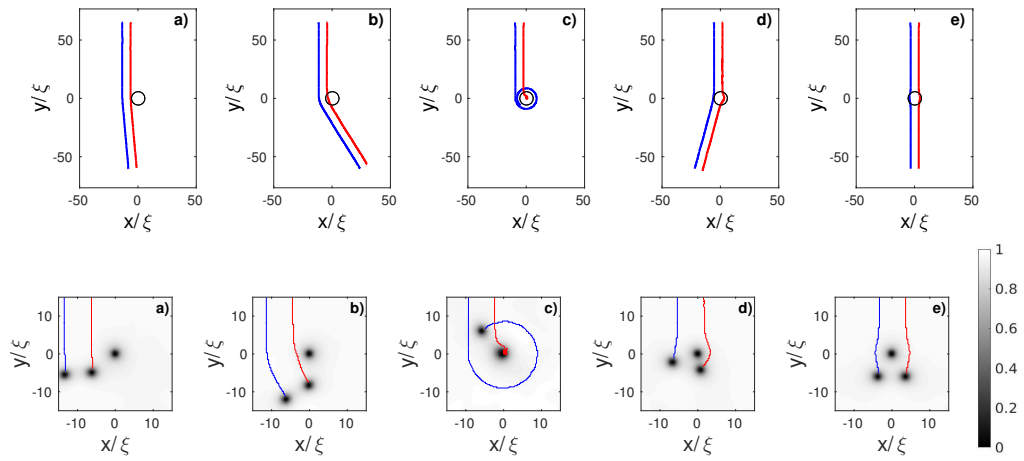

FIGURE 2.2: Scenarios of interactions between the vortex-antivortex pair and the impurity. In all panels the pair travels from top to bottom toward the impurity; the red (right) line and the blue (left) line are the trajectories of the vortex and the antivortex respectively; the black circle at the origin marks the impurity. The top panels show the computed trajectories; the bottom panels show density profiles at arbitrarily selected times together with the trajectories. Panels (a,b): Fly-by scenario for $(h, d) = (-10.0\xi, 6.91\xi)$ and $(-7.9\xi, 6.91\xi)$ respectively. The vortex-antivortex pair is scattered by the impurity, deflecting to the left by an angle θ. Panel (c): Trapping scenario for $(h, d) = (-6.0\xi, 6.98\xi)$. The vortex (red trajectory) is trapped by the impurity, and the antivortex (blue trajectory) orbits around it. Panels (d,e): Go-around scenario for $(h, d) = (-2.0\xi, 6.91\xi)$ and $(0.0\xi, 6.98\xi)$ respectively. The vortex and the antivortex overtake the impurity, going around it in opposite directions.

1. **Fly-by scenario** If the impact parameter h is large and negative, the vortex-antivortex pair is too far at the left of the impurity, see Fig. 2.2(a), to be affected, and the deflection angle is $\theta \approx 0$. If h

increases (still keeping $h < 0$), the vortex-antivortex pair is scattered to the left (as seen from the initial direction of travel) with increasing positive deflection angle θ, as shown in Fig. 2.2(a,b).

2. **Trapping scenario** If h is further increased (still keeping $h < 0$), the vortex falls into the region of low density of the impurity, see the red trajectory of Fig. 2.2(c), becomes trapped and stops, with a strong emission of sound waves, see Fig. 2.3; at this point, the isolated antivortex processes around the impurity, see the blue trajectory of Fig. 2.2(c). In this scenario the deflection angle cannot be defined.

3. **Go-around scenario**

   A further increase of h means that the vortex-antivortex pair is almost aimed at the impurity; the left (anticlockwise) vortex and the right (clockwise) vortex overtake the impurity on opposite sides, going around it along opposite directions, before joining again, re-forming the pair, and moving on to infinity. Fig. 2.2(d) shows that for slightly negative values of h the vortex pair is scattered to the right ($\theta < 0$); for $h \approx 0$, see Fig. 2.2(e), the vortex-antivortex pair proceeds almost straight ($\theta \approx 0$), vortex and antivortex going around the impurity in opposite directions.

Finally, for larger, positive values of h, the trajectories of the vortex and the antivortex are the same (as the impurity does not introduce any preferred orientation), θ being replaced by $-\theta$ (in other words the function $\theta(h)$ is antisymmetric in h). We summarize the scenarios which we have revealed by plotting the deflection angle θ as a function of the impact parameter h, see the blue line and dots in Fig. 2.4(top). The shaded areas represent the regions where the deflection angle θ cannot be defined (one vortex becomes trapped) and the blue line is interrupted.

It is instructive to replace the impurity with a third vortex, choosing positive anticlockwise circulation, initially placed at $x_I = y_I = 0$. In this way we can directly compare the deflections of the vortex pair's trajectory caused by a third vortex to the deflection caused by an impurity with the same density perturbation, isolating the effect of the vortex circulation.

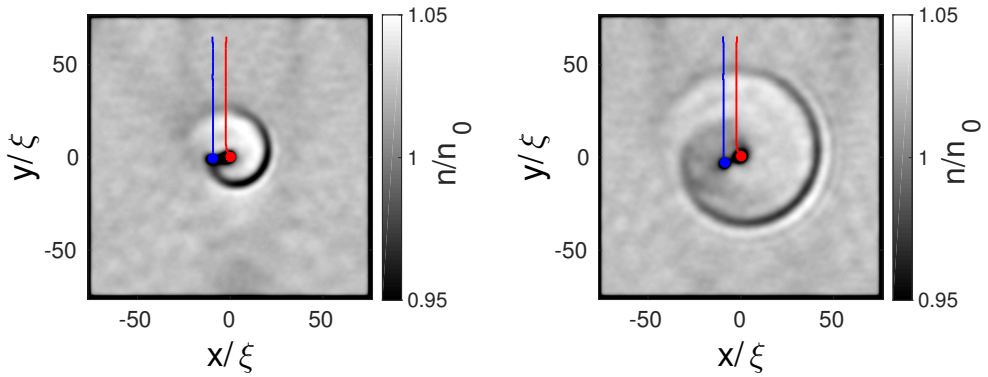

FIGURE 2.3: Trapping scenario. Plots of relative density n/n_0 showing the emission of a sound wave during trapping, corresponding to the evolution shown in Fig. 2.2(c), at two different times $t_1 = 485\tau$ (left) and $t_2 = 505\tau$ (right). The red (right) line and dot mark the vortex and its trajectory, the blue (left) line and dot mark the antivortex. At t_1 the vortex and the antivortex are respectively at $(0, 0)$ and $(-9.3\xi, -0.6\xi)$; at t_2 they are at $(0, 0.6\xi)$ and $(-8.7\xi, -3.0\xi)$.

Unlike the impurity, which is fixed, the third vortex is free to move under the velocity field of the vortex-antivortex pair. The deflection angle θ caused by the third vortex is shown by the red line and dots of Fig. 2.4(top). It is apparent that, for large negative impact parameters, the deflection angle θ is approximately the same for vortex and impurity, but becomes significantly larger for the vortex at small negative h; moreover, there is no trapping regime for the vortex. Note also that, for the vortex, the curve $\theta(h)$ is not antisymmetric about $h = 0$ as in the case of the impurity: for $h < 0$, the closest interaction is between vortices of the same sign, which makes the two close vortices to rotate around each other causing a deflection to the left ($\theta > 0$) with respect to the initial direction of motion; for $h > 0$, the closest interaction is between vortices of the opposite sign, which makes the two close vortices to travel away together, causing a deflection to the right ($\theta < 0$); with respect to the initial direction of motion. This is why the two peaks of the red curve of Fig. 2.4(top), which represent these strong interactions, are not symmetric about $h = 0$. Between these two peaks there is a regime in which the antivortex of the pair swaps place with the (initially stationary) third vortex, which couples with the original vortex of

the pair and travels away with it, forming a new pair.

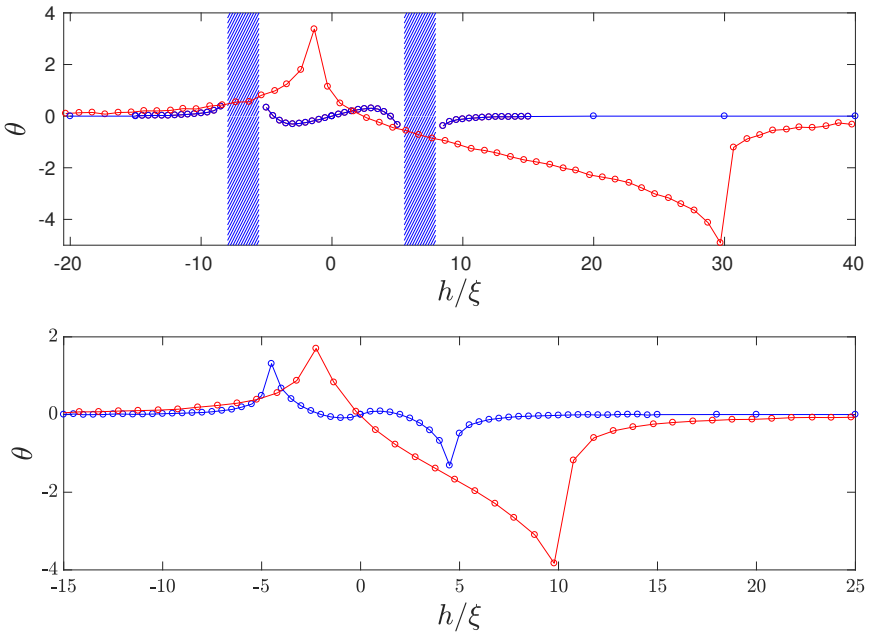

FIGURE 2.4: Deflection angle θ as a function of impact parameter h for initial vortex-antivortex separation $d \approx 6.9\xi$ (top) and $d \approx 2.9\xi$ (bottom) when the target is an impurity (blue line and dots) and a vortex (red line and dots). The shaded blue areas represent the parameter regions where θ cannot be defined because one vortex becomes trapped in the impurity. Comparing top and bottom, notice the absence of the trapping regime and the extension of the figure to larger positive values of h (negligible deflection if the target is an impurity, non-negligible if it is a vortex).

An example of this swapping regime is presented in Fig. 2.5(a). Finally, notice that the effect of the third vortex extends to large positive values of h, unlike the effect of the impurity.

Fig. 2.4(bottom) shows what happens if we halve the initial separation of the vortex from the antivortex to $d \approx 2.9\xi$. At this short separation, the trapping regimes disappears (the vortex, now rather close to the antivortex, moves at large speed, and the impurity is not strong enough to stop it). The other features of the interaction remain qualitatively the same as for the larger pair separation $d \approx 6.9\xi$.

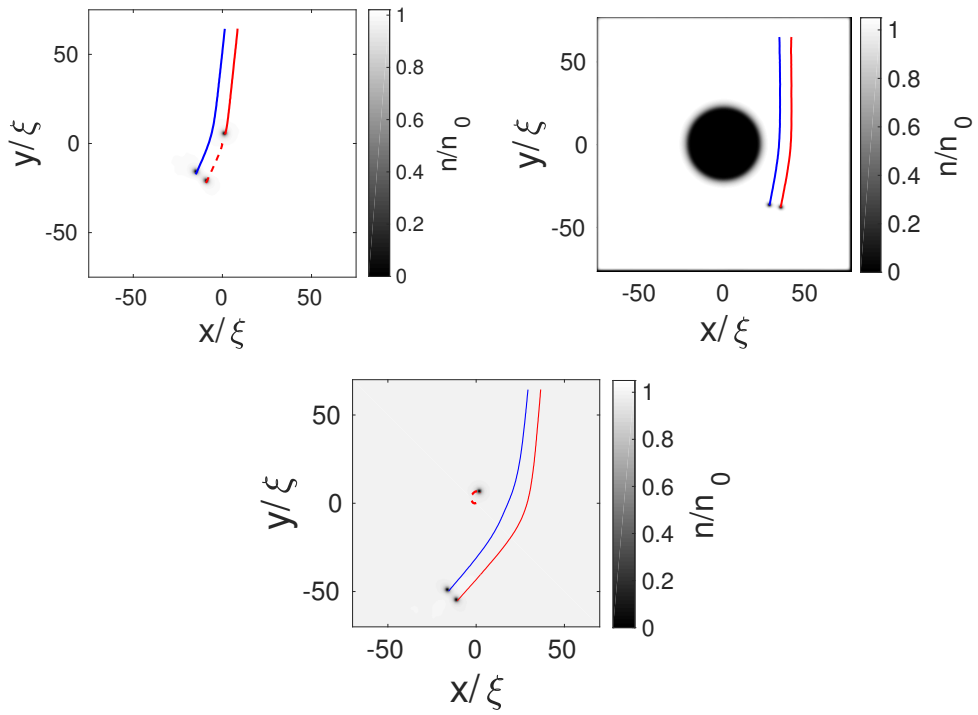

FIGURE 2.5: Top left: Example of vortex swapping scenario (initial separation $d = 7.26\xi$, impact parameter $h = 4.66\xi$). Top Right: Example of vortex deflection around large impurity. Bottom: scattering from a third vortex (initial $d = 7.2\xi$, $h = 32.7\xi$); notice the movement of the third vortex.

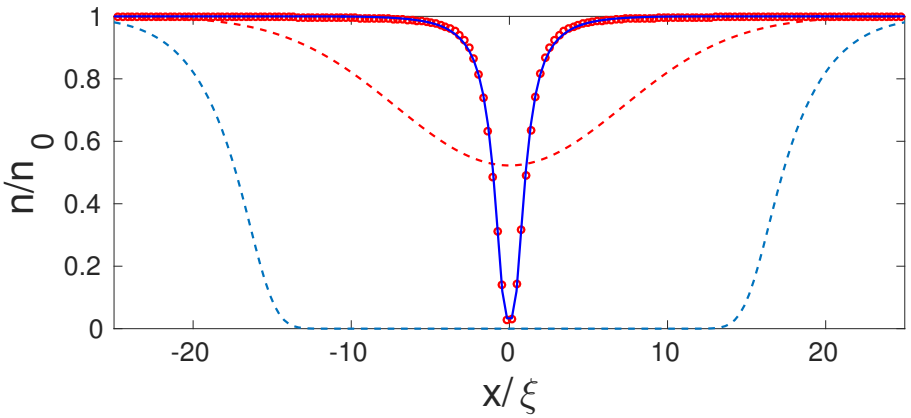

FIGURE 2.6: Relative density profiles, n/n_0 vs x, of vortex (solid red line and circles), standard impurity (solid blue line), large impurity (dashed blue line) and shallow impurity (dashed red line).

Increasing the size of the impurity or making it shallower - as for the density profiles shown by the dashed red and blue lines of Fig. 2.6 - does not change the scenarios of interaction with the vortex-antivortex pair in a qualitative way. Fig. 2.7(top left) and Fig. 2.7(bottom left) show the go-around scenario respectively for a large deep impurity and for a smaller, shallower impurity (the density at the centre is only $n \approx 0.5$). It is interesting to notice that phase defects (ghost vortices) appear inside the large impurity - compare the top right and bottom right panels of Figs. 2.7. An example of the scattering regime with an impurity similar to the size of the large impurity of Fig. 2.6 (dashed blue line) is shown in 2.5(b).

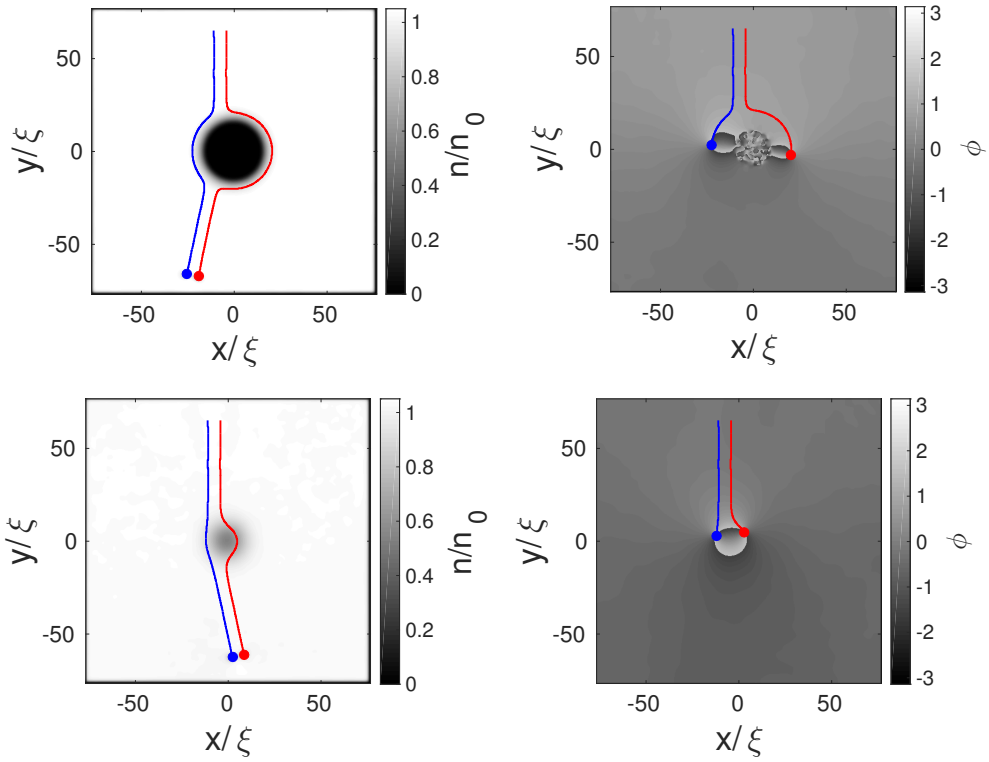

FIGURE 2.7: Go-around scenario for large (top) and shallow (bottom) impurity. The trajectories of the vortex (red line and dot) and the antivortex (blue line and dot) are superimposed to the density $n(x, y)$ (left) and phase(right).

Changing the depth of the impurity whilst keeping the width close to that of a vortex only modifies the deflection angle slightly. For deeper impurities we generally see larger scattering angles in the region close to

the impurity. The general trend is that the shallower the impurity is, the smaller the region in which trapping takes place (see Fig. 2.8), until the impurity is too shallow to trap a vortex, as shown by the black line of 2.8.

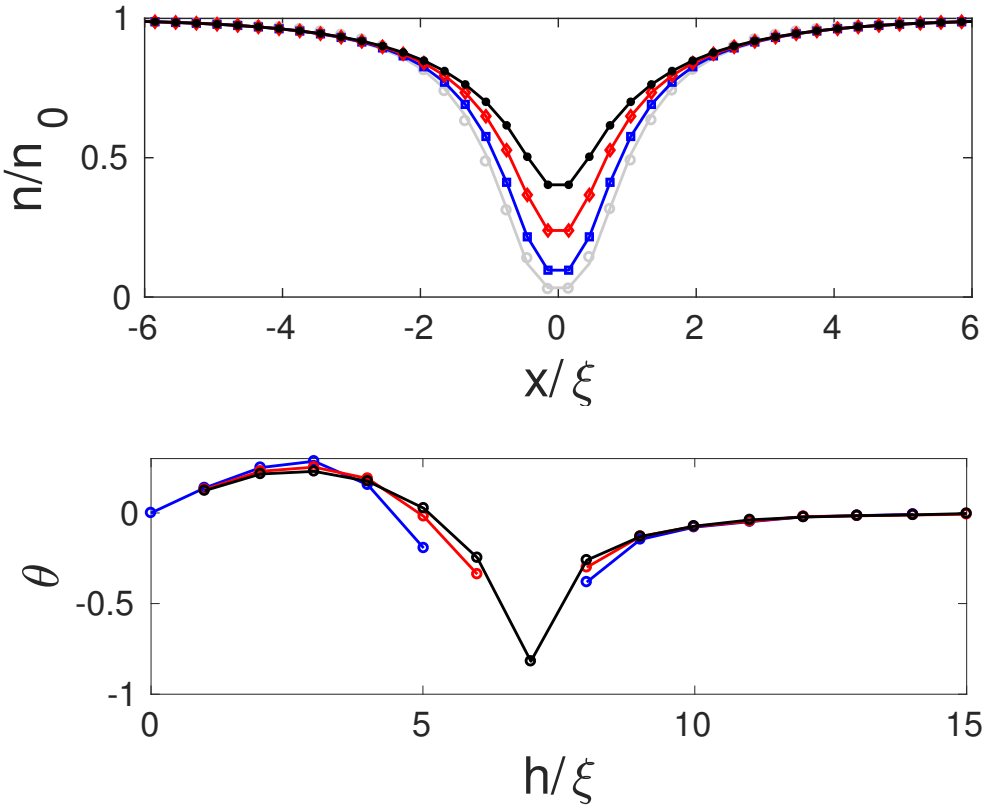

FIGURE 2.8: Top: Density profiles, n/n_0 vs x for vortex-like potential (gray), $n/n_0 = 0.096$ $A_1 = 8$ (blue),$n/n_0 = 0.239$ $A_1 = 4$ (red) and $n/n_0 = 0.403$ $A_1 = 2$ (black). Bottom: Deflection angle θ against impact parameter h. Colours correspond to top figure (lines are interrupted in the region of trapping).

We have already pointed out (Fig. 2.3) that sound waves created by accelerating vortices [12]. In general, these waves represent small acoustic losses of kinetic energy which we quantify by recalling the classical expression for the energy of a vortex ring of radius R and core radius a in a fluid of density ρ, which is [11] $E = \rho\kappa^2 R\mathcal{L}/2$ where $\mathcal{L} = [\ln(8R/a) - 2]$. Neglecting variations of the slow logarithmic term, by measuring the change of distance between the vortex and the antivortex of the pair, we can estimate

the relative energy loss $\Delta E/E \approx \Delta R/R$, which is as high as $\Delta E/E \approx 6\%$ for the scattering shown in Fig. 2.5(b).

IV Discussion and conclusions

We have compared trajectories of vortex-antivortex pairs launched either towards a third vortex or toward an impurity in the form of a similar density hole but without the circulation. By varying the impact parameter, we have identified three general scenarios (fly-by, trapping, go-around) which can occur. In the first scenario, the effect of the impurity if qualitative similar to that of the vortex, in the second and third scenarios it is significantly different. These scenarios represent the elementary processes which can be recognized within a turbulent system. They are therefore relevant to experiments in which vortices are manipulated by laser beams and to studies of 2D quantum turbulence, as large density perturbations are often generated by vortex annihilations or by the moving laser beam used to nucleate vortices in the first place.

Our results are consistent with work on the scattering of 2D quasi-solitons from potential barriers [74], for example we observe that a vortex pair is deflected towards a density dip rather than away from it as predicted (see their Fig. 1, bottom). Our work is motivated by the aim of getting insight into what is typically seen in experiments and numerical simulations of 2D vortex turbulence, and differs from Ref. [74] in three respects. Firstly it is concerned with well-separated vortex and antivortex rather than solitons (when the speed of the pair exceeds the critical value $v/c = 0.61$ where c is the sound speed, the circulation is lost and the pair becomes a solitonic object). Secondly it refers to much smaller impurities (of the order of the core size, not ten times larger). In particular, unlike Ref. [74], in our work the vortex and the antivortex which make up a pair can separate. Thirdly, by solving directly the GPE, we allow acoustic losses unlike the model equations of Ref. [74].

Future work should look at the effects induced by an inhomogeneous density background in harmonically trapped condensates. Other aspects

which are worth investigating are thermal and quantum fluctuations, which are not included in our mean field GPE model. Qualitatively, one would expect thermal fluctuations to move the vortex and the antivortex of a pair closer to each other, eventually leading to their annihilation. This effect would lead to the introduction of a new length/time scale associated with the vortex-antivortex pair's intrinsic decaying dynamics. Qualitatively, however, we would still expect the same regimes to emerge. Quantum fluctuations would lead to an intrinsic jitter motion of each vortex about its mean position, with the target impurity also suffering some fluctuations from the fluctuating density in that region. On the average we would still expect the fly-by and go-around scenarios to persist, but our discussion here may represent a rather idealised case. In fact it would be interesting to investigate this scenario experimentally.

Chapter 3

Breaking of Josephson junction oscillations and onset of quantum turbulence in Bose–Einstein condensates

I Introduction

The Josephson junction (JJ) is an experimental set-up designed to showcase the Josephson effect [54]. This quantum mechanical effect, which describes particle tunnelling through a barrier and periodic oscillations, is well studied in the context of Bose–Einstein condensates (BECs) in both theory [2, 20, 90] and experiments [22, 4, 65, 114, 104]. In this article, we discuss the dynamics when a BEC JJ is pushed to its limit and "goes bad". Namely, we study the regime where the periodic oscillations in the superfluid density break down and quantum turbulence arises in the system.

Current methods to create vortex turbulence include optical spoons [69] and shaking confining traps [77]. Both of these mechanisms have drawbacks, the methods require much energy to create a single vortex in fluids with high density. Moreover, if the density is low the resulting vortices annihilate very quickly; therefore, the creation rate will be similar to the annihilation rate. We propose a method to create vortex dipoles with initial imbalance and sustain them by using a Kibble-Zurek [56, 128] like mechanism to prolong the vortex turbulence, that is, create vortices in a region of low density and

then increase the density in a controlled manner to maintain the topological defects and decrease the relative strength of the acoustic waves.

The Josephson junction consitsts of a barrier or weak link separating two wells of superfluid or superconductor. We consider two wells separated by a potential barrier with an initial density imbalance between the wells. As the system evolves the fluid moves through or over the barrier, which leads to oscillatory dynamics. We show that when the initial density imbalance is pushed to high values, the regime of regular oscillations break down. The system then enters into chaotic behaviour with interesting nonlinear dynamics consisting of chaotic motion of vortices coupled with turbulent acoustic waves following the break down of a soliton train caused by a dispersive shock [75]. Studies on critical parameters for vortex generation have been undertaken [124]. However, these do not consider high numbers of vortices an turbulence.

In place of the predictions by Josephson, we see interesting turbulence characterised by a separation of acoustic and vortex turbulence. Such chaotic dynamics appear when an initial train of solitons are formed then break down, causing the generation of vortices. This is due to the instability of quasi-1D solitons.

We demonstrate that the Josephson junction is a nonlinear system and that by tuning experimental parameters, we can produce rich and controllable non-linear behaviour, which gives an ideal set up for turbulence. Readily available experimental apparata in BECs [22, 77], atomic vapors [51] and photorefractive crystals [73] can implement such a system. We show that a crucial element in the turbulent dynamics in such a system is due to the interaction of vortex dipoles with the barrier. These are responsible for the separation of turbulence within the two wells, with one retaining most the vortices and the other containing weak acoustic wave turbulence [80]. Certain parameters (for instance the incidence angle) control the ability for vortices to cross the barrier [74, 106].

II The mathematical model

To model theoretically the JJ we perform direct numerical simulations (DNS) of the Gross–Pitaevskii (GP) equation. The GP equation describes the dynamics of a BEC made of dilute ultra-cold gas of bosons [45, 89]. For simplicity we consider the case of a quasi-two dimensional BEC, that is we simulate the GP equation in two spatial dimensions as well as time. Lengths are expressed in units of the healing length $\xi = \hbar/\sqrt{2m\rho_0 g_{2D}}$ where ρ_0 is the mean density, g_{2D} is the effective two-dimensional interaction constant between bosons of mass m, and μ is the chemical potential of the system. Time is rescaled by ξ/c, where $c = \sqrt{\rho_0 g_{2D}/2m}$ is the speed of large scale density/phase fluctuations (sound) in the bulk. The external potential V is given in units of $\rho_0 g_{2D}$. The non-dimensional form of the GP equation reads as follows:

$$i\frac{\partial\psi}{\partial t} = \left(-\nabla^2 + V(\mathbf{x},t) + |\psi(\boldsymbol{x},t)|^2\right)\psi(\boldsymbol{x},t)\,. \tag{3.1}$$

The complex wave function $\psi(x,y,t)$ is the BEC order parameter. The BEC order parameter can be expressed in fluid like variables via the Madelung transformation $\psi = \sqrt{\rho(\mathbf{x},t)}e^{i\phi(\mathbf{x},t)}$, where $\rho(\mathbf{x},t) = |\psi(\mathbf{x},t)|^2$ and $\mathbf{v}(\mathbf{x},t) = 2\nabla\phi(\mathbf{x},t)$ are the density and velocity of the superfluid respectively. In our dimensionless variables we rescale density by the initial density ρ_0.

Our aim is to model an elongated JJ domain, large with respect to the healing length, in order to observe the formation of several quantised vortices and, eventually, fully developed quantum turbulence. We thus choose a two-dimensional spatial domain $\mathbf{x} = (x,y)$, with $x = [-256\xi, 256\xi]$ and $y = [-128\xi, 128\xi]$, setting a computational uniform grid of spacing 0.25ξ. We have Dirichlet boundary conditions with $\psi = 0$ at the boundary, this is effectively confining the fluid in an abrupt rectangular tap with an external potential at the boundary with infinite strength. The JJ barrier is modelled using an external potential $V_{JJ}(\mathbf{x},t)$ that separates the domain into two equally sized boxes, labelled B_L and B_R corresponding to the position left or right of the potential. The potential is given by a Gaussian function centred at $x = 0$ and stretched along the entire y-axis. To create the initial

superfluid density imbalance needed to trigger the JJ oscillations at $t^\star$, an extra non-zero external potential (almost) uniform V_d is present in the right box. Mathematically, the JJ barrier thus results in

$$V_{JJ}(x, y, t) = V_0 e^{-\frac{x^2}{\sigma^2}} + V_d \tanh(x) H(t^\star - t)\,, \tag{3.2}$$

where V_0 and σ control the intensity and the width of the JJ barrier, respectively, V_d sets the initial density imbalance and $H(\cdot)$ is the Heaviside step function. In all the simulations reported in this work we keep $\sigma = 1.2$ so that the width of the barrier is always similar to the healing length in the system.

To create the initial condition, we use imaginary time propagation for $t < t^\star$. This method involves evolving the GP model with the substitution $t = -i\tau$ while imposing conservation of the superfluid density to effectively minimise the energy of the system. Once the desired energy stagnation has been reached, we call the obtained state the *ground state*, set $t = t^\star$ and evolve the system in real-time. Because of the sudden jump in the V_{JJ} at $t = t^\star$, the initial condition is no longer the ground state; therefore, dynamics follow. The GP equation (3.1) is integrated using the 4th order central finite difference method in space and a Runge-Kutta 4th order method time-stepping scheme. Due to the nature of the method, only waves with wavelength of the order of half the healing length or higher are well resolved; smaller waves will be numerically dissipated. This natural dissipation of high energy high-frequency waves is ideal for such a study as dissipation occurs in experiments similarly due to the interaction with the thermal cloud and/or bosons losses due to finite-amplitude confining potential [24, 66].

III Results

III.i Measurable quantaties

We define the relative superfluid density imbalance

$$Z(t) = \frac{N_L(t) - N_R(t)}{N_L(t) + N_R(t)} \tag{3.3}$$

using the total superfluid mass

$$N_i = \int_{B_i} |\psi(x,y,t)|^2 dxdy \tag{3.4}$$

per box B_i where i is an index for the box left or right of the separating potential, Note that the total density $N = N_L + N_R$ is an integral of motion and it is numerically conserved in all simulations up to numerical dissipation. Analogously, the energy per box reads

$$E_i(t) = \int_{B_i} |\nabla\psi(x,y,t)|^2 + V(x,y)|\psi(x,y,t)|^2 + \frac{1}{2}|\psi(x,y,t)|^4 dxdy\,. \tag{3.5}$$

The total energy $E = E_L + E_R$ is also an integral of motion, but due to the intrinsic high-frequency numerical dissipation, its value decreases in time as much as 28% when $Z_0 = 0.49$ around 10% when $Z_0 = 0.88$. For the results in section III.iii, where there is no acoustic turbulence, the energy is conserved to 0.0015%. The energy is naturally decomposed in (3.5), with the second term corresponding to energy from the external potential and the third term the internal energy of the fluid. We can further decompose the first term into kinetic and quantum energy by applying the Madelung transformation $\psi = \sqrt{\rho}e^{i\phi}$ to the first term

$$|\nabla\psi|^2 = |\nabla\phi|^2\rho + |\nabla\sqrt{\rho}|^2, \tag{3.6}$$

where the first term corresponds to the kinetic energy density and the second term is the so called quantum energy density. By performing a Helmholtz decomposition on the kinetic energy density we can further decompose into the compressible and incompressible energies. That, is $\varepsilon_{kin} = \varepsilon^c_{kin} + \varepsilon^i_{kin}$,where the incompressible component of the energy corresponds to the vector field satisfying $\nabla\cdot(\sqrt{\rho}\mathbf{v})^i = 0$. Further details on the calculation can be found in [86]. Thus the energy can now be written

$$E_i(t) = \int_{B_i} \varepsilon^c_{kin} + \varepsilon^i_{kin} + |\nabla\sqrt{\rho}|^2 + V(x,y)|\psi(x,y,t)|^2 + \frac{1}{2}|\psi(x,y,t)|^4 dxdy\,. \tag{3.7}$$

The total incompressible energy $E^{in}_{kin} = \int_{B_L+B_R} \varepsilon^{in}_{kin} dxdy$ is a measure of the energy in large scale incompressible potential flow and vortices, whereas the total compressible energy $E^c_{kin} = \int_{B_L+B_R} \varepsilon^c_{kin} dxdy$ is the energy in the acoustic component.

It is also convenient to define the *local* healing length for each box as

$$\xi_i(t) = \sqrt{\frac{L^2}{N_i(t)}} \tag{3.8}$$

and we will call the natural healing length of the system ξ, that is, the healing length if the initial density imbalance is set to zero. The length of each box in units of ξ is given by L.

Finally, it is instructive to measure the total number of vortices

$$N_V(t) = N_{V_L}(t) + N_{V_R}(t) \tag{3.9}$$

in the system versus time, with N_{V_L} and N_{V_R} the number for the left and right boxes respectively. Each quantised vortex is numerically identified using the pseudo-vorticity defined as follows,

$$\omega_{\rho s} = \frac{1}{2}\nabla \times \mathbf{j}, \tag{3.10}$$

with

$$\mathbf{j} = \rho\mathbf{v} = -\frac{i}{2}(\psi^*\nabla\psi - \psi\nabla\psi^*) \tag{3.11}$$

$$\tag{3.12}$$

where $\mathbf{j}$ is the density flux. Then we find the maxima in simply connected regions ignoring the field below a chosen cut-off value, see [116] for further details. Ghost vortices are phase fluctuations in large regions where ψ is

close to zero, these do not show the same dynamics as hydrodynamical vortices. We add an extra filter to our vortex tracker, namely we only consider vortices with substantial density surrounding them, this is to remove the ghost vortices and to track only the hydrodynamic vortices. The numerical scheme calculates the average density around any point identified by the vortex tracking routine and discards the vortex if the average is below a threshold value.

III.ii Creation of vortices

In the GP model, 1D dark or grey solitons are unstable to transverse perturbations in two spatial dimensions, the instability is known as the snake instability. This instability is a result of the speed of a soliton being proportional to its amplitude. The instability can be understood as a result of smaller solitons having larger speeds. A small transverse perturbation introduces a local difference in speed of the soliton. Such a difference in speed will cause the soliton to bulge in the direction of motion if the perturbation is negative, or the opposite direction if the perturbation is positive. For instance, if we introduce a bulge in the direction of motion, since the soliton will move perpendicular to its tangent there will be a focussing effect on either side of the perturbation. Since the speed of the soliton is reduced when its amplitude increases, the focused parts of the solitons slow down producing an inverted bulge. The process then continues along the length of the soliton with bulges and inverted bulges forming along the soliton, for more details and mathematical analysis see [61]. When a grey-soliton's amplitude becomes as large as the density around it, i.e. points at which $\psi = 0$ will appear: phase defects in the form of vortices are nucleated. In this section we will discuss how we take advantage of this instability to produce vortices.

The potential is such that a train of solitons is produced within a dispersive shock wave in the right well which has low density $N_L(0) < N_R(0)$, this can be seen in Fig. 3.1 which shows an example simulation for the entire domain. Fig. 3.1(a) shows the production of the train of solitons, seen as the stripes in the low density region. The solitons will then decay by the

snake instability into alternating signed vortices, the process begins at the boundary and can be seen in Fig. 3.1 (b) with later stages in Fig. 3.1 (c). Due to the large number of vortices and to the fact that the local density is small, the initial vortices have large cores and do not interact like hydrodynamic vortices. These vortices are often referred to as ghost vortices and are not counted by the tracking algorithm. The continuous flow of solitons carrying density into the right well reduces the local healing length, which in turn transitions the ghost vortices towards hydrodynamic vortices. After the ghost vortices are produced in Fig. 3.1 (b), we see chaotic motion with a proliferation of hydrodynamic vortices in Fig. 3.1 (c) when the density becomes larger due to the fluid flux from the left box. As the process continues, the healing length tends to ξ in both boxes, the healing length when $N_L = N_R$. Some opposite signed vortices annihilate which results in continuous decay of the total number of vortices. As a result, the remaining vortices become even better formed as hydrodynamic because the mean distance between them becomes much greater than ξ. Later stages of the dynamics are shown in Figs. 3.1(c-d) where many of the vortices have decayed.

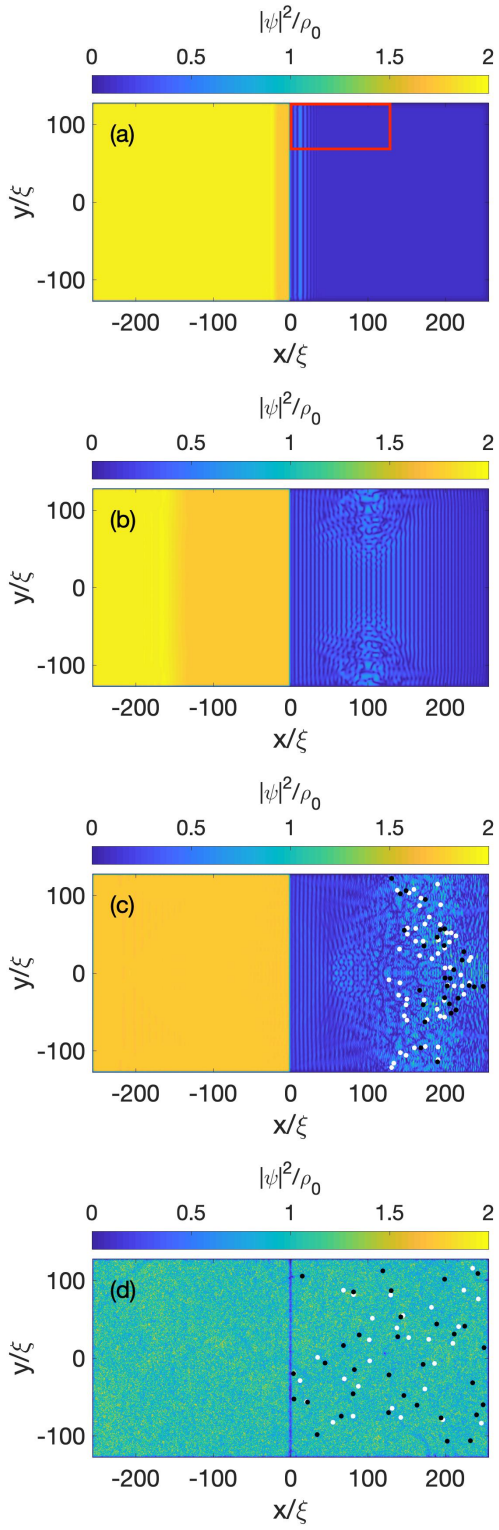

FIGURE 3.1: Density fields for simulation with $V_0 = 1.5/\mu$, $\sigma = 1.2/\xi$ and $Z_0 = 0.88$. Panel (a): $t = 20\xi/c$; (b): $t = 90\xi/c$, Panel (c): $t = 150\xi/c$, Panel (d): at $t = 3000\xi/c$. The red box in (a) indicates the region which we zoom in on in Fig. 3.2. Positive vortices are shown with the white circle and negative with a black circle.

In order to show the snake instability better, we present an example of the early stage 2D density and phase fields with potential strength $V_0 = 1.5/\mu$ and initial imbalance $Z_0 = 0.88$. We zoom in on the subregion of B_R in Fig. 3.2 (a), the region depicted by the red rectangle in Fig. 3.1 (a).

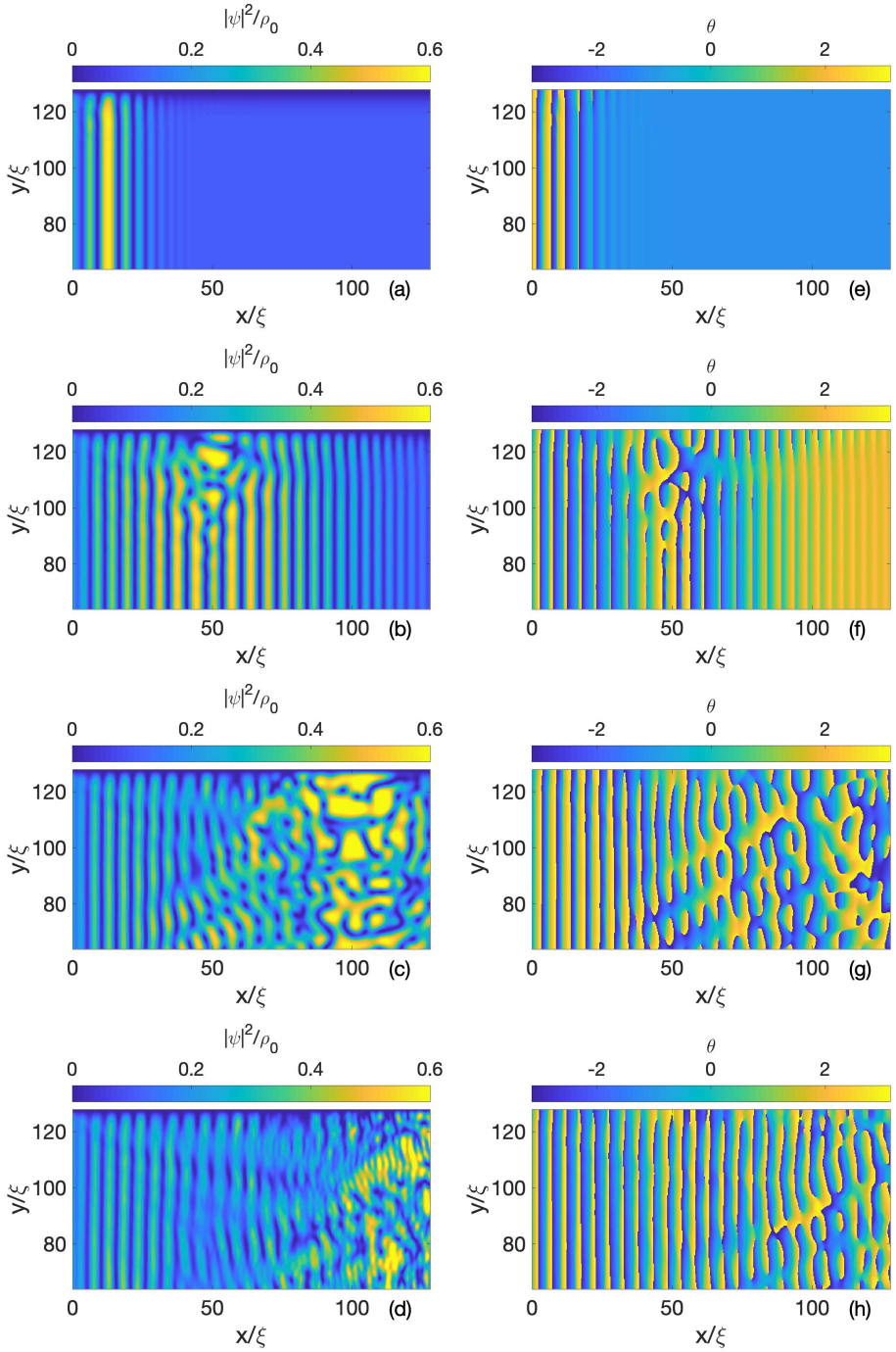

FIGURE 3.2: Zoom on density and phase fields in simulation with $V_0 = 1.5/\mu$, $\sigma = 1.2/\xi$ and $Z_0 = 0.88$. Panels (a-d): density field, (e-h): phase field. The zoomed window is the red rectangle in Fig. 3.1(a). Panels (a,e): $t = 30\xi/c$, (b,f): $t = 60\xi/c$, (c,g): $t = 100\xi/c$, (d,h): $t = 150\xi/c$.

The train of quasi 1D solitons within a dispersive shock region is seen in Fig. 3.2 (a). Fig. 3.2 (b) shows the snake instability forming on the solitons. As they travel, the solitons begin to snake until they break up into a chain of ghost vortices with circulations of alternating signs, which then interact to form vortex turbulence. The ghost vortices can be seen in the corresponding phase plots. For instance, in Fig. 3.2 (f) we see discontinuities in the phase where the phase winds from $-\pi$ to π around them. The ghost vortices correspond to the dark (blue) circles in Fig. 3.2 (b). They are not counted as in the number of vortices or marked by the black and white circles corresponding to the well-formed hydrodynamic vortices.

In the case of many atoms, where the Laplacian term in the Gross-Pitaevskii equation can be neglected, we can analytically find the stationary profile for the wave function. The latter is known as the Thomas-Fermi (TF) profile. We choose to take a slice along $y = 0$ as there is no y- dependence on the potentials. When the fluid has enough energy to flow over the barrier, that is when the TF profile $|\psi(x)_{TF}|^2 > 0$ for all x, the dynamics are different to that of the classical Josephson junction as the flow is not only a consequence of tunnelling but also due to the fluid which has enough energy to pass the barrier. The stationary TF profile is given by:

$$\begin{cases} \psi_{TF} = \sqrt{\rho_0 - V_0 e^{\frac{x^2}{\sigma^2}} - V_d \tanh(x)} & \text{if} \quad \rho_0 - V_0 e^{\frac{x^2}{\sigma^2}} - V_d \tanh(x) > 0, \\ |\psi_{TF}|^2 = 0 & \text{otherwise.} \end{cases}$$

Thus the barrier TF width, W_{TF}, is given by:

$$W_{TF} = \sigma \sqrt{\ln\left(\frac{V_0}{\rho_0 + V_d}\right)}. \tag{3.13}$$

From this we can see that flow has no tunnelling when $V_0 < \rho_0 + V_d$. Once the vortices are introduced, confining them to the right box only should make them interact more due to the smaller inter-vortex distance. The main process in which vortices spread out is by forming dipoles which move away from the vortex bulk at a nearly constant speed. These vortices can

penetrate the barrier in certain cases, namely when V_0 is small and/or the vortex dipole is fast. The barrier width W_{TF} will also affect the ability for vortices to penetrate the barrier. Such dependences of the penetrability on the barrier and vortex properties are not obvious, so we will now present a study to classify and quantify different outcomes of the dipole-barrier interactions.

III.iii Vortex dipole scattering off the barrier

The interaction between quantised vortices and the JJ barrier plays a vital role in the dynamics discussed in section III.ii and is an interesting problem in itself. The barrier can trap vortices as well as assist in their annihilation. In certain regimes of 2D vortex turbulence, vortices tend to couple into vortex dipoles [80]. This process is the result of random vortex motion; it includes inter-vortex collisions which can re-couple or scatter vortex pairs. As a result of this motion some vortex pairs will move away from the turbulent bulk. As we have boundaries, the vortices will be incident either on the outer boundaries or the barrier. If the dipole is incident on the outer boundary it, will get split into the two vortices moving along the boundary in opposite directions. If the dipole is incident on the barrier, it can be transmitted, annihilated or trapped, depending on the barrier height and the dipole size.

In this subsection we present a study of a vortex dipole interacting with a JJ barrier where no initial density imbalance between the the left and right boxes is present, that is, $Z_0 = 0$ and $V_d = 0$. Initially, we position a vortex dipole centred at $(-25\xi, 0)$, and define θ as the angle between the x-axis and the direction of propagation of the vortex dipole. Clearly by symmetry, we expect the dynamics to be mirror-symmetric with respect to the $x-$axis i.e. with respect to the change $\theta \to -\theta$. The vortices are initially separated by a distance of d_0, and the vortex with positive circulation is in the upper-half plane so that the dipole moves towards the positive x-direction. Examples of the resulting vortex trajectories are shown in the different panels of Fig. 3.3. In Fig. 3.3 we see that in all examples the vortices lose energy to sound during the interaction with the barrier. We quantify the amount of sound

emitted by calculating the change in the incompressible energy

$$\Delta E^i(t) = E^i(0) - E^i(t) = \int_{B_L+B_R} \left(\varepsilon^i_{kin}(x,y,0) - \varepsilon^i_{kin}(x,y,t)\right) dxdy.$$

We measure this change in energy at a final time t_f after the interaction has happened. As a criteria for determining t_f we choose the following three criteria: (i) the vortex dipole passed the line $x = 25\xi$ corresponds to Fig. 3.3 (a,d); (ii) either vortex becomes within 5ξ of the system boundary corresponds to Fig. 3.3 (b); (iii) if case (i) and (ii) are not fulfilled we allow a maximum time of $t_f = 750\xi/c$. We assume that the vortices have annihilated if they do not fulfil case (i) or (ii) after such a long time, so case (iii) corresponds to vortex annihilations an example is shown in Fig. 3.3 (c).

Fig. 3.3 shows four different examples of the dipole-barrier scattering for different values of the scattering parameters V_0, d_0 and θ. The images show the superfluid density plots after the scattering with the dipole with the trajectories overlaid. For the dipole-barrier scattering experiments presented in this subsection we have chosen to shorten the L_x side and increase the L_y side of the JJ system, compared with the one presented for instance in Fig. 3.1, in order to give the vortices more space to interact with the barrier. Fig. 3.3 (a) shows a the path two vortices take when passing a barrier. Notice that the vortices after the interaction are closer together. As the vortices' motion was perpendicular to the barrier there was no deflection. Fig. 3.3 (b) shows the case of a dipole not being able to pass the barrier. This corresponds to case (ii). The vortices separate from one another and move along the barrier. The vortices effectively see images of themselves in the barrier. This motion is similar to that when a vortex-pair is incident on an external boundary, where the boundary conditions are similar to that of an infinite barrier. Fig. 3.3 (c) shows an annihilation, this is case (iii). Fig. 3.3 (d) shows the vortices being deflected during the interaction with the barrier. In this example the vortices were not moving perpendicular to the barrier but had an incidence angle $\theta = 0.4\pi$.

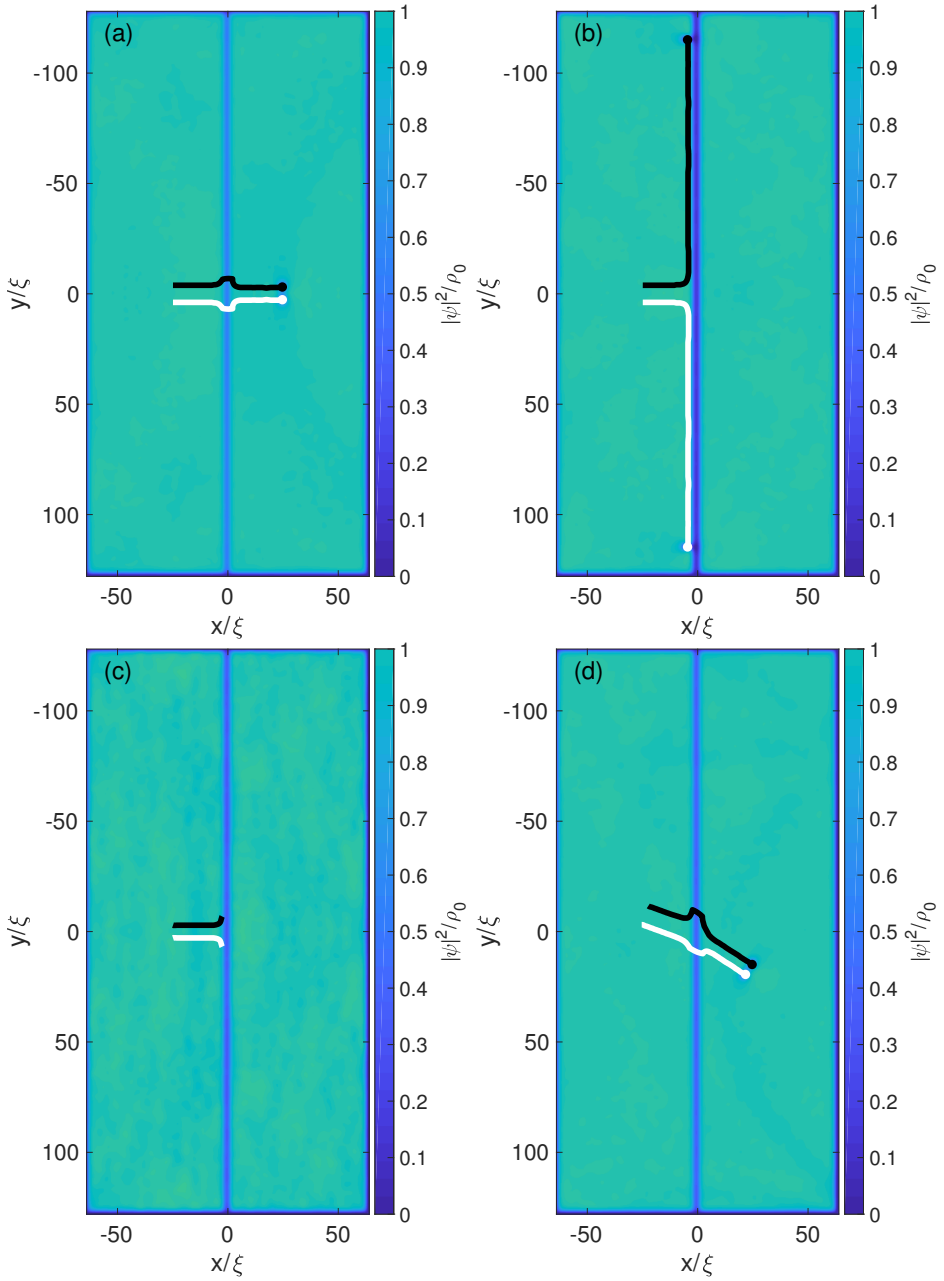

FIGURE 3.3: Examples of vortex-barrier interactions. Panel (a): Vortices crossing the barrier at $V_0 = 0.8/\mu$ and $d_0 = 8/\xi$. Panel (b): Vortices trapped by the barrier at $V_0 = 1.9/\mu$ and $d_0 = 8/\xi$. Panel (c): Vortices annihalting $V_0 = 1.2/\mu$ $d_0 = 6/\xi$; (d): Vortices passing with aninitial angle of incedence of 0.4π, $V_0 = 1.15/\mu$ and $d_0 = 10/\xi$. The white line corresponds to the vortex trajectory and the black line corresponds to the antivortex.

We perform two sets of simulations for two different incidence angles $\theta = 0, 0.4\pi$, sweeping over different vortex separations d_0, and vortex barrier heights V_0. We observe and classify for each set of parameters, what kind of dipole barrier interaction takes place, (i), (ii) or (iii), and also measure sound released in the interaction. The results are presented in Fig. 3.4. Firstly we calculate whether or not a vortex dipole of separation d_0 will pass the JJ barrier of given strength V_0; the cases when the dipoles pass are marked with asterisks.

If the dipole cannot pass, this can be due to two reasons: the dipole is annihilated by the barrier producing sound (case (iii) marked by squares) or the interaction of the dipole and the barrier is not over when the boundary effects become relevant(case (ii) marked by circles). In the latter case, it is not possible to say whether the dipole would have annihilated in an infinite domain or not, hence it is a consequence of the finiteness of the system. We see that when annihilations happen, there is more sound energy (measured by the change in the incompressible energy) released from dipoles with larger separations. Fig. 3.4 shows that there are clear connected regions in which each of the possible cases happens.

As we mentioned in the introduction our aim is to explore the best parameters for vortex turbulence. Annihilations are key events which determine the vortex decay rate, which will be further discussed in section III.ii. We see that the barrier can cause annihilations. In Fig. 3.4 (a) we see that the annihilations are numerous and they also correspond to a high emission of sound. As well as removing vortices from the system, the extra sound is known to increase the vortex decay rate [79]. On the other hand, the highly energetic sound produced can penetrate the barrier and be spread over the adjacent box which is void of vortices. As a result, the sound is distributed over twice the area (both the wells). Thus, the second well acts as a sound absorber i.e. as an effective heat sink. By introducing a finite angle of incidence θ, the amount of vortex annihilations is greatly reduced. At the same time vortex splitting becomes much more frequent. However, the amount of vortices that pass the barrier does not change much. We see that small dipoles ($d_0 < 7$) are annihilated by the barrier in the region of the barrier strength $V_0 \sim 1$. For the region $V_0 = 1.3 - 1.6$ with large dipoles

($d_0 > 7$) we see that the dipoles separate. Compared to the splitting region in Fig. 3.4(a) in this case they emit much more sound.

The vortex-barrier interaction discussed here is more simple than the interaction when the densities are unequal, the background condensate is saturated with sound, and there are more than two vortices involved in the interaction. The results are informative as a rough measure of the vortices ability to cross the barrier.

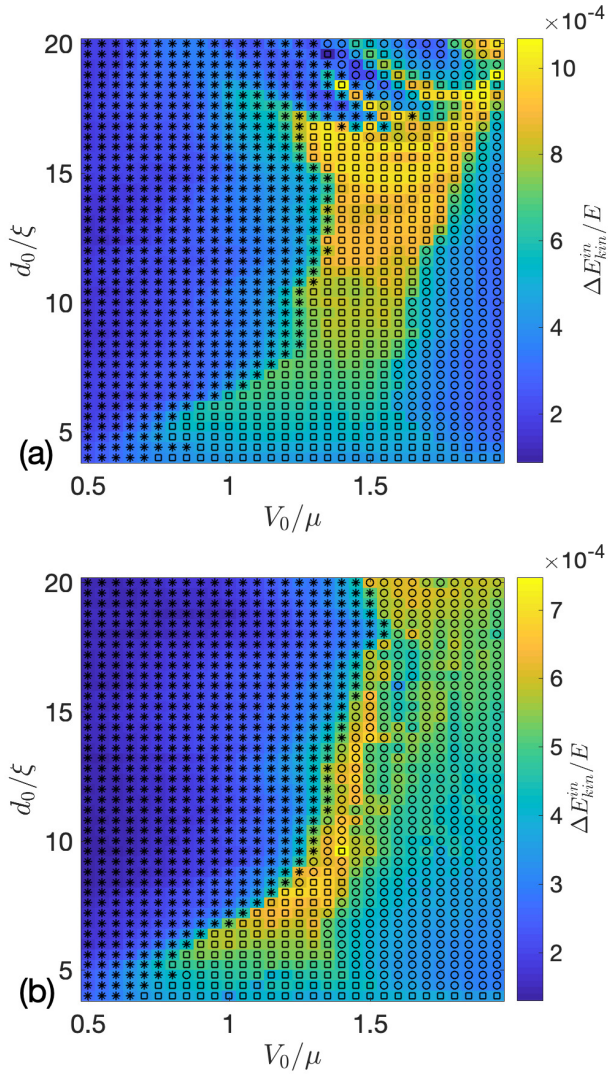

FIGURE 3.4: Panel (a): parameter sweep of initial dipole separation and barrier height for angle of incidence $\theta = 0$. Scaled colour indicates the approximated compressible energy at $t = t_f$. Overlaid points show if the dipole passed (asterisks), annihilated (squares) or interacted with boundary (circles). Barrier width $\sigma = 1.2$. Panel (b): similar parameter sweep for $\theta = 0.4\pi$.

III.iv Vortex turbulence

Optimal parameters

We now discuss the optimal choice of parameters to produce vortex turbulence. Our aim is not only to produce the highest number of vortices, but to also minimise the secondary by-products of the method, namely, sound and large density waves. We also introduce the mean number of vortices over time

$$\bar{N}_v = \frac{1}{T}\int_0^T N_v(t)dt, \tag{3.14}$$

and for the left and right box, $\bar{N}_{V_L}$ and $\bar{N}_{V_R}$ respectively. We use the mean (opposed to the maximum) as a measure as it also takes into account the sustainability of the vortex turbulence. We not only want to create many vortices we want them to persist for as long as possible. Another measure we use to classify the quality of the turbulence is the amount of interfering compressible waves, these account for the large scale density sloshing and the small scale acoustic component. Obviously, it is desirable to minimise such compressible motions.

The mean number of vortices produced by the proposed method depends both on the barrier strength and the initial imbalance. In Fig. 3.5 we show the effects of varying the two control parameters, the barrier strength V_0 and the initial imbalance Z_0. In Fig. 3.5 (a) we see that for a large imbalance ($Z_0 = 0.88$) increasing V_0 monotonically reduces the mean number of vortices, and for a large enough V_0 no vortices will be produced; this is due to the barrier disrupting the creation of solitons by reducing the rate at which fluid can cross the barrier. On the other hand, for a lower initial imbalance ($Z_0 = 0.49$), Fig. 3.5 (a) shows that there is a clear maximum for the mean number of vortices in B_R at around $V_0/\mu = 0.6$. This is due to the mechanism discussed in section I: a steady influx of density 'freezes' the vortices in the right well and the potential reduces oscillations of the density imbalance which would otherwise strongly interact with the vortices. For a high initial imbalance ($Z_0 = 0.88$), the mean number of vortices

is higher without a barrier as shown in Figs. 3.5 (a). However, as we will discuss below, the vortices are accompanied by more small-scale (acoustic) and large scale (sloshing) compressible waves, which is an undesirable effect if we want 'clean' vortex turbulence. Even when the initial imbalance is high in Fig. 3.5 (a) and there is no barrier ($V_0 = 0$), the vortices are evenly distributed over both boxes. As a consequence the amount of vortices in the right box B_R, is not so much larger than the cases with higher values of V_0.

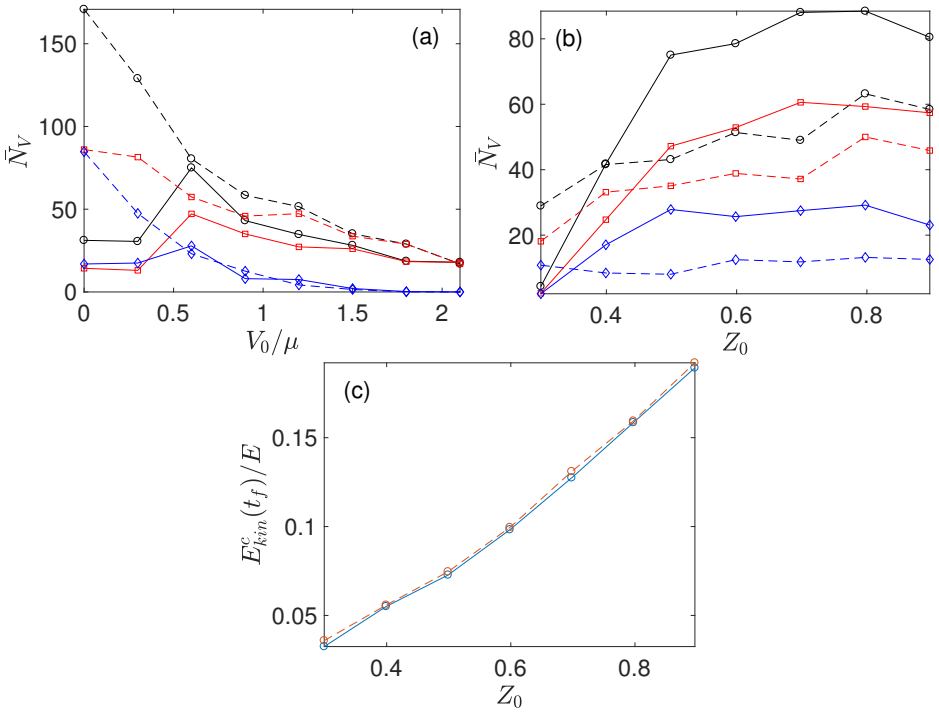

FIGURE 3.5: Panel (a): the mean number of vortices against barrier height for two values of initial imbalance $Z_0 = 0.49$ (full line) and 0.88 (dashed line). The circle (black), square (red) and diamond (blue) correspond to vortices in $B_L + B_R$, B_R and B_L respectively. Panel (b): two values of barrier height $V_0 = 0.6/\mu$ (full line) and $0.9/\mu$ (dashed line) against the mean number of vortices for the entire domain $B_L + B_R$ (black circles), the right box only B_R (red squares) and the left box B_L (blue diamonds). Panel (c): the compressible energy as a percentage of the total energy against the initial imbalance for two barrier strengths $V_0 = 0.6/\mu$ (full line) and $0.9/\mu$ (dashed line).

When V_0 is fixed, by increasing the initial imbalance we reach a plateau in the mean number of vortices in Fig. 3.5 (b). This plateau, along with the increase in compressible energy in Fig. 3.5 (c), indicates that after a certain imbalance the energy is more swiftly converted into compressible sound waves. Using this insight, we propose that it is preferable to choose a lower imbalance such that the vortex dynamics are cleaner, that is, there is less acoustic turbulence and large-scale density sloshing interacting with the vortices.

A secondary effect also complements the longevity of the vortex turbulence. The highly-energetic small scale sound, produced during the vortex creation and subsequent interactions, can easily pass the barrier. The sound energy from the vortex turbulence of the right well is then distributed over twice the area, reducing the interaction with the vortices and, therefore, slowing down their annihilation rate.

In the absence of a barrier, many vortices are produced; however, we identify two critical issues with the turbulence that follows. The first is that the local healing length oscillates for a long time, see Fig. 3.6 (a). The fluctuation of the local healing length causes vortices to annihilate. Secondly, the large density waves are seen to interact with vortices, this adds additional complexity to the interactions, and it is not clear what the effect on the vortex interactions this will have. Introducing a barrier addresses both of these problems as seen in Fig. 3.6. When a barrier is present, as in Fig. 3.6 (b), the oscillations are dampened, with only small oscillations remaining once the boxes have equilibrated. This is due to the amplitude of the large wave simultaneously being reflected and transmitted on each barrier interaction. This multiplies the number of waves decreases the size of the local wave amplitude. Also, it causes the density to fill the right box more smoothly. The smoother descent is due to barrier reflecting more of the wave when the barrier is stronger. That is, the amplitude of the transmitted wave is reduced on each wave-barrier interaction, therefore, the density flux across the barrier is also reduced; this essentially dampens the overshooting of the oscillations. This can be seen in Fig. 3.6 (c) where we plot the standard deviation of the oscillations, σ, against barrier strength: this reduces quickly when the barrier strength increases and a transition

seems to occur at a value close to $V_0/\mu = 1$. We choose the time period to measure the standard deviation over to be the same for each simulation. The period is chosen to be after the all the simulations have reached $Z(t) = 0$ for the first time.

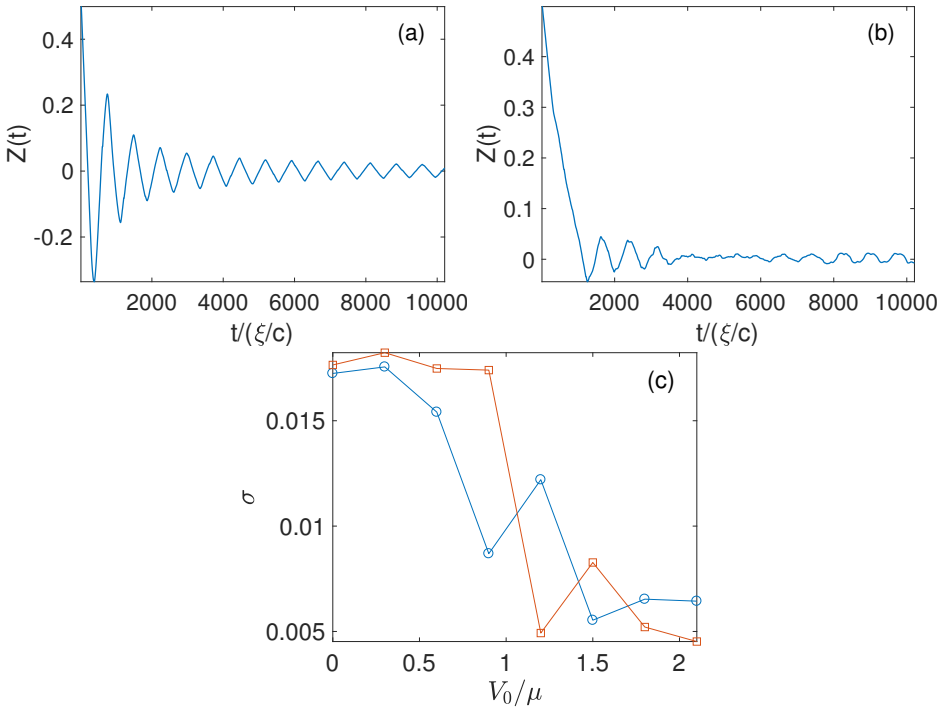

FIGURE 3.6: Panels (a): Evolution of relative density $Z(t)$ for parameters $V_0 = 0.0$, $\sigma = 1.2$ and $Z_0 = 0.49$. Panel (b): the same for $V_0 = 1.5$, $\sigma = 1.2$ and $Z_0 = 0.49$. Panel (c): the standard deviation of $Z(t)$ after $t_s = 4200\xi/c$ for a range of different barrier heights. The blue line with circles is for $Z_0 = 0.49$ and the red with squares $Z_0 = 0.88$.

Vortex decay rates

Recent discussions [8, 27, 62], indicate that the number of vortices in a homogeneus condensate decay as $t^{-1/3}$, this corresponds to four-vortex interactions. The arguments in [8, 27, 62] use a simple logistic equation for the number of vortices N_v,

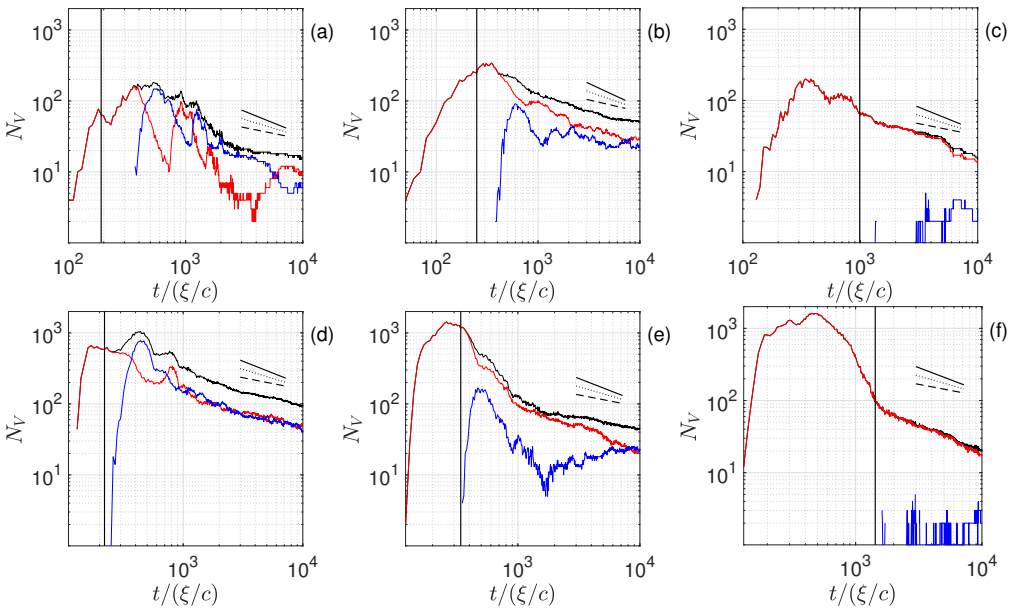

FIGURE 3.7: Log-log plots of number of vortices against time. For low initial imbalance, (a-c), $Z_0 = 0.49$ and barrier height: (a) $V_0 = 0.0$; (b) $V_0 = 0.6$ and (c) $V_0 = 1.5$. For high initial imbalance, (d-f), $Z_0 = 0.88$ and barrier height: (c) $V_0 = 0.0$; (e) $V_0 = 0.6$ and (f) $V_0 = 1.5$. The black full line is shows $t^{-2/3}$ law, the dotted to $t^{-1/2}$ and the dashed line – $t^{-1/3}$. The vertical black line shows the time when $Z(t) < 0.05$ for the first time. The red lines corresponds to the number of vortices in the right box, the blue the left box and the black the total number of vortices.

$$\frac{dN_v}{dt} = -CN_v^{\alpha}, \tag{3.15}$$

where α here corresponds to the number of colliding vortices causing an annihilation and C is a constant. Equation (3.15) is a crude approximation which does not take into account any correlation between the vortices, nor does it take into account spatial inhomogeneity in the system. Following this approach, for two-vortex annihilations we have N_v is proportional to t^{-1}, for three-vortex interactions – to $t^{-1/2}$ and four-vortex interactions – to $t^{-1/3}$. More specifically, one could present a more general model for vortex decay:

$$\frac{dN_v}{dt} = -\sum_{i=1}^{N_p} C_i N_v^i. \tag{3.16}$$

Such a model allows for N_p competing processes of vortex decay. One would expect that the constants, with respect to time, C_i each have a dependence on the compressible energy in the fluid as well as other properties which may influence decay such as barriers. We note that finding the precise set of C_is for our experiments would require much more data, instead we present a fit of equation (3.15) as an indicator of the vortex decay processes present.

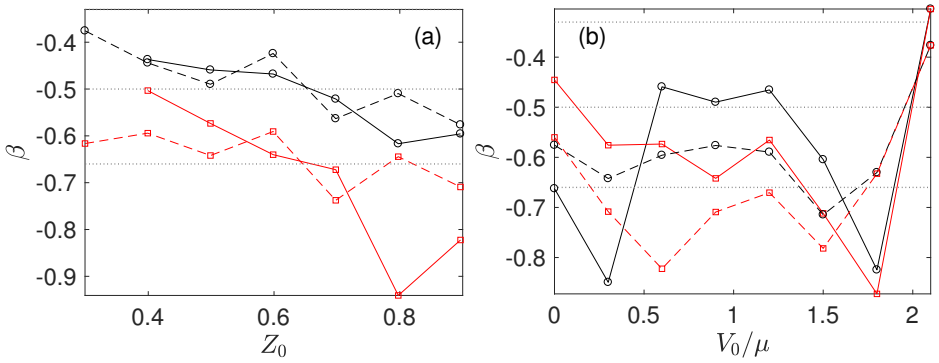

FIGURE 3.8: Vortex number decay fitted with $t^{-\beta}$. Panel (a): The decay rate β in the entire domain (black circles) and right box (red squares) as we increase initial imbalance with $V_0 = 0.6/\mu$ (full line) $0.9/\mu$ (dashed line). Panel (b): The decay rate α in the entire domain (black circles) and right box (red squares) as we increase barrier height with initial imbalance $Z_0 = 0.49$ (full line) 0.88 (dashed line). The grey dotted horizontal lines are markers for $-1/3$, $-1/2$ and $-2/3$.

In our system, the decay of vortices from B_R can happen in four ways: (1) vortices annihilate via vortex-vortex interaction; (2) vortices annihilate at the barrier or boundary, see Fig. 3.3 (c); (3) vortices pass the barrier and enter to B_L, see Fig. 3.3 (a,b,d) (however, the barrier can be chosen such that the vortices cannot penetrate or so that only vortex dipoles of a certain

size can exist in the left well, this is discussed further in section III.iii); (4) vortices annihilate from interacting with the background sound.

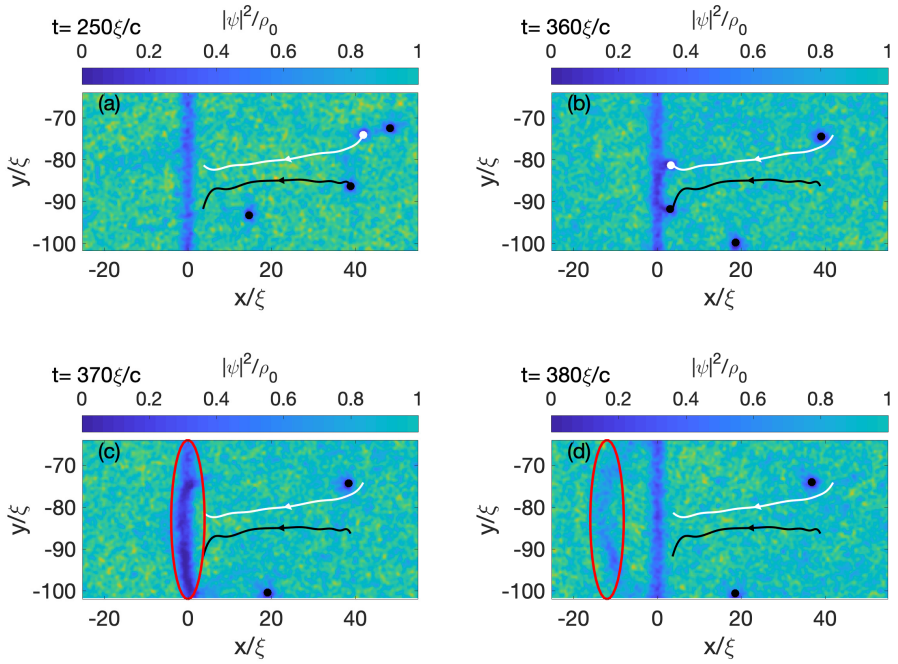

FIGURE 3.9: Vortices annihilating at the barrier. Density plots with parameters $V_0 = 1.2/\mu$, $\sigma = 1.2/\xi$ and $Z_0 = 0.49/\mu$. The time is indicated in the figures. The white line is the trajectory of the vortex and the black lines are the antivortex trajectories. The filled circles are the positions of the vortices in each frame. The arrows indicate the direction of motion of the vortice and the ellipses the sound waves post collision.

Fig. 3.7 shows examples of the evolution of the number of vortices in a log-log plot. In the figure the red line represents the number of vortices in the right box N_{V_R}, the blue the number in the left box N_{V_L} and the black the total in the entire domain $N_{V_R} + N_{V_L}$. We overlay a vertical line for which the imbalance has become almost zero ($Z < 0.05$) for the first time in each simulation, this is an indicator of when the initial vortex creation period has ended.

We first focus on the decay rate in the later stages of the dynamics where we expect to see the exponents predicted above. We present in Fig. 3.7 cases

with two values of initial imbalance, $Z_0 = 0.49$ (a-c) and $Z_0 = 0.88$ (d-f). In the cases with no barrier (a, e) we see that the vortices move freely between the two boxes. In Fig. 3.7 (a) in particular, we do not produce enough vortices to see vortex turbulence, thus we do not see a clear decay rate. In Fig. 3.7 (e) homogeneous vortex turbulence develops quickly with an almost equal amount of vortices in each box. In this case we see a decay closer to $t^{-1/3}$ which is predicted for a four-vortex process. In Fig. 3.7 (f), for small value of V_0, see also a decay closer to $t^{-1/3}$, whereas a t^{-1} decay is seen for higher barrier height in Fig. 3.7 (g), which corresponds to a two-vortex collision in the logistic equation.

Clearly the amount of vortices in the left box decreases with the barrier height. It also appears that the number of vortices in the right box remains almost the same whilst the number in the left tends to zero. We also note that for cases with a high initial amount of vortices there is a steeper decay rate. We propose that some transition in the dominant type of the vortex collision occurs at a vortex density which is dependent on the mean density of the vortices. Indeed, it is natural to think that the higher-order vortex collision (e.g. four-wave) dominates over the lower-order collision (e.g. three-wave) for higher vortex densities and vice versa. The mean vortex density is dependent on the barrier height in a non-trivial way as shown in section III.iii.

It is difficult to distinguish the best fit from the decay in Fig. 3.7 by visual inspection. We instead calculate the the best fit numerically and present the results in Fig. 3.8. We choose a value t_s such that all the simulations are safely in the late stage vortex decay regime and calculate the best fit of the exponent over the same range in all the simulations.

In Fig. 3.8 (a) we present the exponent plotted against increasing initial imbalance Z_0. We notice that the decay rate is faster for a higher imbalance. We conjecture that this is due to the higher mean vortex density as well as an increased acoustic component (see Fig. 3.5 (c)) which interacts with the vortices helping them to annihilate. In Fig. 3.7 (b) as the barrier height increases the total number of vortices (black line) and the vortices in the right box (red line) converge due to all of the vortices being in the right box. We also see in Fig. 3.8 (a) and (b) that the decay rate fluctuates.

However, for most of the parameters, it seems to be steeper than $t^{-1/2}$ and shallower than t^{-1} which may be due to the combination of all of the annihilation mechanisms. For instance, the decay rate may be explained by the interaction with the boundary and barrier, which can aid annihilation. For instance in Fig. 3.9 we see a vortex dipole scatter of a third vortex (a three-vortex precess) until the dipole is small enough such that the boundary or the barrier will annihilate them (a two-vortex process). Also in Fig. 3.9 (c,d) the red ellipses show the dynamics during (c) and after (d) the interaction with the barrier. We highlight that the rarefaction pulse caused by the annihilation is directed into the left box, thus the pulse is not likely to interact with other vortices causing more annihilations. We note that by increasing dipole size, we do not necessarily increase the chance of annihilation; see Fig. 3.4 (a). If we take $V_0 = 1.6/\mu$ we see that smaller dipoles are trapped whereas larger dipoles annihilate.

IV Conclusions

In this paper, we have explore the use of a Josephson junction set-up for generating BEC vortex turbulence. We have shown that the generation and decay of vortices in a Josephson junction BEC configuration, can be altered by controlling the barrier height and the initial density imbalance parameters, which can be readily applied to existing experimental apparatus. We discussed the critical advantage of this method for generating vortex turbulence is the creation of vortices in low-density regions, with the density then being increased to solidify (shrink) the vortex cores. We have provided ranges of parameters to tune the barrier to produce a certain optimal number of vortices and also shown parameters which allow for vortex penetration. We showed that for a higher imbalance we produce more vortices. However, most of these vortices decay quickly leaving much of acoustic noise and large-scale density sloshing, and for this reason it may be preferential to have a smaller initial imbalance. For instance, if one would like to create vortices confined to a single box with the acoustic component less than 10% of the total energy one would choose an initial imbalance of $Z_0 = 0.6$, with

a barrier with strength (measured in chemical potential μ) in the range of μ to 1.5μ with the width of the order of the healing length. Although our simulations are larger than current experiments, there are experiments that are not so much smaller [41, 52].

Another disadvantage of the vortex turbulence without the barrier is the large wave-vortex interaction. A key consideration is the control of the amount of sound energy released as part of the snake instability. Such sound can be shared over the two boxes while confining the vortices to one box, and thereby separate the vortices and sound in physical space better so that the sound does not adversely affect the vortex dynamics. We show that the interaction of vortices with a quasi-1D barrier is non-trivial and that the barrier also can work as another effective mechanism for vortex dissipation. This is particularly interesting in terms of using such a barrier to filter vortex turbulence and produce vortices of a certain size, a more detailed study will be the subject of future work. In this work we focused on the vortex turbulence; however, the acoustic turbulence present is also worth further study.

Chapter 4

Modelling particle motion in GPE

I Introduction

Superfluidity occurs in a wide variety of systems both terrestrial, e.g., ^{4}He-II, ^{3}He-B (B-phase), Bose-Einstein condensates (BECs) of alkali atoms, exciton-polariton condensates [21] in laboratory experiments, and exotic astrophysical objects, such as neutron stars [14, 118]. Moreover, a monochromatic light while passing through a non-linear media, e.g., photo-refractive crystals [73], has been shown to exhibit a flow that is essentially superfluid. The unusual flow properties of these superfluid flows have held the attention of experimentalists and theorists alike. For example, helium II can sustain rotational motion only through formation of quantised vortices, wherein the circulation along paths enclosing vortices is restricted to multiples of h/m_4, where h is the Planck's constant and m_4 is the mass of a ^{4}He atom [32]. These quantised vortices in helium II are angstrom size in diameter, and they occur either as closed loops or filaments that must end at the boundary of the fluid.

Quantised vortices display rich dynamical behaviour [120]: For example, in three dimensional (3D) rotating superfluid systems, above the vortex nucleation threshold, the number of vortices increases with rotation speed, and can form a vortex lattice. At still higher rotation speed the system transitions to a turbulent state [113]. It is a non-equilibrium state involving

processes that span a broad range of length- and time-scales, and is characterised by the presence of a dynamic random tangle of interacting vortices [38, 84, 85]. These quantised vortices upon close approach can undergo reconnections [18, 93], a topology changing process that further drives the system to a turbulent state. Reconnection events excite Kelvin waves on the vortices, and the non-linear interaction of these waves gives rise to a cascade process that transfers energy to smaller length scales, which is ultimately radiated as sound [60, 9, 39, 98]. Turbulence in these superfluid systems can also be excited by stirring, shaking, moving objects, etc. [71, 101, 49]. Moreover, a turbulent state can also be realised in two-dimensional (2D) superfluids[78, 30], where point-like vortices move chaotically[82, 52], and can organise to produce large scale flows. The subject has seen a spurt of activity, both numerical and experimental, to find its universal features and provide a comparison with its classical counterpart [19, 96, 99].

However, it must be emphasised the experimental study of the fundamental processes involved in superfluid turbulence is a difficult task and requires state of the art facilities [32, 10]. In particular, visualisation of the quantised vortices has been a challenge because of extremely low temperatures and small system sizes. The flow visualisation methods available for classical fluids are difficult to adapt to superfluid helium [47].

Use of particles to probe superfluid flows involving vortices was suggested in Ref. [31]. A great deal of information about quantised vortices, including their existence, in helium II has been obtained, in the past, by the use of moving ions [121]. More recently, solid-hydrogen particles were used to visualise quantised vortices in helium II at temperatures $\sim 2\,\mathrm{K}$ [17, 33]. These particles were also used to study vortex reconnection events [18] and Kelvin waves [39] on vortices in superfluid helium. Note that in these experiments, even though particles used were roughly 10^4 times the vortex diameter, they managed to capture the essential physics.

Now much smaller particles in the form of metastable $^4\mathrm{He}_2^*$ excimer molecules, $\sim 100\,\mathrm{nm}$ in size, are available that can be used as vorticity tracers. More specifically, in the $T = 0$ limit, in the absence of normal fluid and at temperatures above $1\,\mathrm{K}$ they act as tracers of the normal component of the fluid [127].

Notwithstanding the significant experimental progress in the use of particles to characterize superfluid turbulence, the exact level of intrusion of the particle on the vortex motion remains unclear. Therefore, it is important to explore and understand these issues by building simplified models to study particle-vortex dynamics both theoretically and numerically[16, 115].

In this work, we focus on the Magnus force that acts on a particle trapped on a translating vortex. To do so, we make use of both the Gross-Pitaevskii equation (GPE) description of superfluids [45, 89] and the suitably adapted classical treatment of point vortices in 2D. In our GPE description, we make use of a recently developed minimal model [97, 88, 100], wherein we couple the equations of motion of particles with the GP classical wave function ψ. We demonstrate that the Magnus force description borrowed from the theory of ideal hydrodynamic flow works and also provides a good description of the dynamics of particle loaded vortices in superfluids. We first study a particle loaded vortex-antivortex pair configuration and carry out systematic direct numerical simulations (DNS) of the GPE based minimal model. We compare these GPE DNS results with a Magnus force model that we have derived (see below), both in the simplified analytically tractable case of constant background flow and a more realistic situation wherein the background flow is allowed to vary in response to the particle loaded vortices (or other external vortices). We then extend our study of the particle loaded vortex-antivortex pair to more complex vortex configurations, where: (i) each vortex is multiply charged; (ii) free external vortices are present in the neighbourhood. We will argue that under certain circumstances, the effects can be observed in superfluid helium experiments. Moreover, our study indicates that particles can be a useful tool for future studies of vortex motion in Bose-Einstein condensates (BECs).

The advantage of our analytical and semi-analytical models is that they can be applied, and work better, for setups with the particles much larger than the healing length, whereas it would be virtually impossible to simulate such systems with huge scale separations in DNS. Such models will be useful, for example, in investigations of the effect of hydrogen ice tracers whose typical diameter is the order of a few micro-meters [17], while the vortex core diameter is of the order of an angstrom ($= 10^{-10}m$). In this situation,

we can think of a classical flow with a thin boundary layer so that classical textbook solutions relating the force on a moving object with the circulation around the object can be used [3]. This indicates that the Magnus model will work better in describing the motion of large particles relative to vortex core size. However, the validity of such a model in quantum fluids can not be taken for granted due to the presence of the compressibility, acceleration as well as a flow non-uniformity over the distances comparable to the particle sizes. We emphasise that the GP equation is only a phenomenological model for superfluid helium; however, the results from this chapter indicate that the dynamics should be present in superfluid helium.

In this chapter, we demonstrate that the Magnus force model works very well even for situations well beyond the formal limits of applicability of the ideal flow descriptions, e.g. when the size of the particle is no so much bigger than the healing length, and the velocity is not so much smaller than the speed of sound.

II Model and Numerical Methods

II.i Gross-Pitaevskii equation coupled with particles

We use the GP theory to model the superfluid flow and study its interaction with particles. The GP framework provides a good hydrodynamical description of a weakly interacting superfluid at low-temperatures and is able to reproduce the qualitative features of the strongly interacting superfluid helium. Within this framework, the state of the system is specified by the complex scalar field $\psi(\mathbf{r}, t)$.

The particles that we consider are *active*; they are affected by flow and act back on it too. In earlier works[97, 88, 100] we introduced a Lagrangian for this combined system, wherein particles were represented by specifying the potential $V_{\mathcal{P}}$. This procedure yields the following GP equation for the spatiotemporal evolution of $\psi(\mathbf{r})$:

$$i\hbar\frac{\partial\psi}{\partial t} = -\frac{\hbar^2}{2m_b}\nabla^2\psi - \mu\psi + g|\psi|^2\psi + \sum_{j=1}^{\mathcal{N}_0} V_{\mathcal{P}}(\mathbf{r}-\mathbf{q}_j)\psi, \tag{4.1}$$

where $\hbar = h/2\pi$ is the reduced Planck's constant, m_b the mass of bosons constituting the superfluid, g the effective interaction strength among these bosons, μ the chemical potential and $\mathbf{q}_j$ the position of the jth particle (i.e. center of the potential).

Our modelling of the particles by specifying $V_{\mathcal{P}}$ allows us to control their characteristics, e.g. shape and size. For the purpose of present study, we use the Gaussian potential

$$V_{\mathcal{P}} = V_0 \exp\Big(-\frac{r^2}{2d_p^2}\Big); \tag{4.2}$$

here V_0 is the strength of the potential and d_{p} is the measure of its width.

Furthermore, we include a two-particle, short-range repulsion potential. Thus, the Newtonian dynamics of the particles is governed by the following equation,

$$m_j \ddot{\mathbf{q}}_j = \mathbf{f}_{0,j} + \mathbf{G}_j, \tag{4.3}$$

where m_j is the mass of the jth particle, which we assume to be same for all, $m_j = m_0$, vector $\mathbf{f}_{0,j}$ is the force exerted by the superfluid onto the particle,

$$\mathbf{f}_j = \int_{\mathcal{A}} |\psi|^2 \nabla V_{\mathcal{P}}(\mathbf{r} - \mathbf{q}_j)\, d\mathbf{r}, \tag{4.4}$$

$\mathcal{A}$ is the area occupied by the particle (determined by a cutoff of the potential (4.2)), and $\mathbf{G}_j = (G_x, G_y) = \hat{\mathbf{e}}_x \sum_{i=1, i\neq j}^{\mathcal{N}_0} \frac{\Delta_E r_{SR}^{12}}{|(\mathbf{q}_i - \mathbf{q}_j)\cdot\hat{\mathbf{e}}_x|^{12}} + \hat{\mathbf{e}}_y \sum_{i=1, i\neq j}^{\mathcal{N}_0} \frac{\Delta_E r_{SR}^{12}}{|(\mathbf{q}_i - \mathbf{q}_j)\cdot\hat{\mathbf{e}}_y|^{12}}$ is the inter-particle short-range repulsion force, where r_{SR} and Δ_E are parameters corresponding to a length and repulsion energy scale respectively.

II.ii Numerical methods, units and parameters

To study the dynamics of particles in complex superfluid flows, we solve Eqs. (4.1) and (4.3) numerically. In order to do so, we perform direct numerical simulations (DNSs) of the GP by using the Fourier pseudospectral method on a square, periodic simulation domain $\mathcal{A}$ of side L with N_c^2 grid points [96]. In this method, we evaluate the linear terms in Fourier space and the nonlinear term in real (physical) space, which we then transform to Fourier space. For the Fourier-transform operations, we use the FFTW

library [1]. A fourth-order, Runge-Kutta scheme is used to evolve these equations in time. Further details can be found in [100].

We define the length scale $\xi = \hbar/\sqrt{m_b g \rho_0}$, known as the healing length and the speed of sound $c = \sqrt{g\rho_0/m_b}$. The mean density can be also calculated $\rho_0 = \int_{\mathcal{A}} |\psi|^2 \, d\mathbf{r}/\mathcal{A}$. We then choose to rescale the parameters in (4.1) with the following scalings: $\tilde{\mu} = \mu/(g\rho_0)$, $\tilde{V}_{\mathcal{P}} = V_{\mathcal{P}}/(g\rho_0)$, $\tilde{\psi} = \psi/\sqrt{\rho_0}$, $\tilde{\mathbf{r}} = \mathbf{r}/\xi$ and $\tilde{t} = tc/\xi$, we arrive at the dimensionless equation which we simulate:

$$i\frac{\partial\tilde{\psi}}{\partial\tilde{t}} = -\frac{1}{2}\tilde{\nabla}^2\tilde{\psi} - \tilde{\mu}\tilde{\psi} + |\tilde{\psi}|^2\tilde{\psi} + \sum_{j=1}^{\mathcal{N}_0}\tilde{V}_{\mathcal{P}}(\mathbf{r} - \mathbf{q}_j)\psi. \tag{4.5}$$

From here on we drop the tildes for simplicity of notation. Taking into account that we are in dimensionless units, in our calculations we can set $\rho_0 = c = \xi = \mu = 1$ by choosing our initial conditions. In dimensionless units we also choose the parameters $L = 177.78$, with the grid spacing $dx = L/N_c$, and the number of collocation points $N_c = 256$. For the external potential we choose the parameters $V_0 = 10$, and $d_{\mathrm{p}} = 1.5$. To calculate the initial conditions we solve the real Ginzburg-Landau equation (RGLE), this minimises the energy of the fluid in the presence of the potentials modelling the particles.

II.iii Magnus force model

Lift force or the Magnus effect is a well-studied phenomenon in classical fluid dynamics [112]. In a fluid flow with a uniform upstream velocity $\mathbf{u}_{\mathrm{flow}}$, a cylindrical disk with circulation Γ around it experiences a lift force $\rho\Gamma\mathbf{u}_{\mathrm{flow}} \times \hat{\mathbf{e}}_z$, where ρ is the fluid density and $\hat{\mathbf{e}}_z$ is the unit vector along the cylinder corresponding to the vorticity direction. This phenomenon in a superfluid was first observed by Vinen [117] by measuring modifications to frequency of a vibrating wire submerged in He II, which also allowed to demonstrate the quantisation of the circulation around the wire. In the present work, the fluid flow relative to a solid object is induced not by mechanical properties of the solid object itself (e.g., its elasticity), but rather

by an external vortex (or multiple vortices) not trapped by this particular object.

Here, we want to explore the dynamics of an assembly of particles trapped on 2D vortices in superfluids. In particular, we want to elucidate the role of the Magnus force acting on these particles. To this end, we develop a Magnus force model (MFM) to describe this system. The Magnus force induced acceleration of the jth particle trapped on a vortex (circulation strength Γ) at the location (x_j, y_j) is given by

$$\ddot{x}_j = A(\dot{y}_j - v_j) + G_x/(m_0 + m'), \tag{4.6}$$

$$\ddot{y}_j = A(u_j - \dot{x}_j) + G_y/(m_0 + m'), \tag{4.7}$$

where the overhead dots indicate time derivative; (u_j, v_j) is the flow velocity at the position of the particle collectively induced by the other (excluding the jth) vortices. The model describes the motion of the particle induced from two competing Magnus forces. The first induced by external flows and the second induced by the particle's motion relative to the surrounding fluid. In our description of the particle dynamics, we ignore the variation of the flow velocity over a distance comparable to the particle radius. Such an approximation is valid when the distance between the particles is large compared to both the particle radius and the healing length. The parameter $A = \Gamma\rho/(m_0 + m')$ is the natural oscillation frequency of the vortex trapped particle in our system. m_0 is the physical mass of the particle and m' the hydrodynamical added masses (see below).

Note that in (4.6) and (4.7) we have introduced a short-range repulsion G between the particles, which acts only when the particles come to distances comparable to their size. Strictly speaking the approximation that the velocity around a particle is uniform fails at such short distances; however, our goal in this paper is to test the model beyond its formal limits of applicability in order to test its robustness. The added mass can be computed using the unsteady Bernoulli equation (derived from the GPE),

$$\frac{\partial\phi}{\partial t} + \frac{1}{2}(\nabla\phi)^2 - \sum_{j=1}^{\mathcal{N}_0} V_{\mathcal{P}}(\mathbf{r} - \mathbf{q}_j) = \frac{1}{2}\frac{\nabla^2\sqrt{\rho}}{\sqrt{\rho}} - \frac{p}{\rho}, \tag{4.8}$$

where $\phi = \arg\psi$, which relates to the superfluid velocity $\mathbf{v}$ via $\mathbf{v} = \nabla\phi$, density $\rho = |\psi|^2$ and the first term on the right hand side in Eq. (4.8) is the quantum pressure term. Note that in this model the dynamics are compressible and that $\rho = \rho(\mathbf{x}, t)$.

Let us assume for the moment that the potential representing the particle is hard, i.e., it has a well defined boundary (an extension to the case of "soft" particle potential is made later). In such a case, the superfluid density ρ is zero within the particle boundary and it "heals" to its bulk value over a boundary layer that is approximately healing length wide. Now, if the particle radius $R \gg \xi$, then we can regard the particle and its boundary layer as a single moving control volume. This allows us to neglect the quantum pressure at the boundary of the considered control volume, and we can write

$$p = -\rho\left(\frac{\partial\phi}{\partial t} + \frac{1}{2}|\nabla\phi|^2\right), \tag{4.9}$$

i.e. the classical expression for irrotational ideal fluids. Thus, we can apply the classical textbook calculations for both the Magnus force and the added mass by integrating the pressure distribution over the control volume boundary[63]. If the particle under consideration is a 2D disk of radius R, then the $\frac{\partial\phi}{\partial t}$ term gives rise to the added mass $m' = \rho\pi R^2$.

Our method of treating the dynamics of particle loaded vortices self-consistently takes into account the variations in the background flow velocity around the particles because of the dynamically varying separation between the vortices. It is important to appreciate the fact that the Magnus force description given by Eqs. (4.6) and (4.7) depends on the motion of the particle relative to the fluid and the resulting force is perpendicular to the motion. In the other words, there would be no Magnus force if the particle motion was tracing the fluid paths (this regime would be realised by the limit of very small and light particles).

In our GP simulations, we use a Gaussian potential, which has a soft boundary, to represent particles; therefore, we need an estimate of an effective radius to compute the added mass m'. A consequence of the soft boundary is that the fluid can penetrate a region of the potential, but is

slowed down by the increasing strength of the potential until the reflection point. An explicit calculation of the effective radius is a non-trivial exercise. Therefore, we compute it in an ad-hoc manner by making use of the Thomas-Fermi (TF) profile of the superfluid density around the particle potential. The TF profile is the density of a time-independent solution of Eq. (4.5) in which we remove the Laplacian term, this approximates the density depletion due to the particle on the surrounding fluid with no kinetic energy. This approximation is valid when the number of bosons is very large. The TF profile $|\psi_{TF}|^2$ in the presence of a single particle is then given by

$$|\psi_{TF}|^2 = \left(1 - V_0 e^{\frac{-r^2}{2d_p^2}}\right) \mathcal{H}(r - R_{TF}), \tag{4.10}$$

where $\mathcal{H}$ denotes the Heavyside step function and R_{TF} the radius of the region within which the profile is zero. In Fig. 4.1 we show a slice of the TF profile, along with the initial condition. The initial condition is a slice across the particle as calculated by solving the RGLE with the potentials modelling the particles. The radius R_{TF}, computed from the Eq. (4.10), is given by

$$R_{TF} = d_p \sqrt{2 \log(V_0)}. \tag{4.11}$$

The TF profile allows us to obtain an estimate of the displaced mass of the superfluid due to the particle (while fluid density is held fixed at ρ_0). We use this displaced mass as the added mass, as this captures the features of the soft potential. Thus,

$$m' = 2\pi \int_0^\infty (1 - |\psi_{TF}|^2) r dr. \tag{4.12}$$

To be more clear here, the added mass can be decomposed into two parts: m'_1, the contribution governed by the geometry of the particle, while assuming incompressibility; m'_2, the contribution coming from the boundary

layer. We express this as follows:

$$m' = m'_1 + m'_2 = \pi R_{TF}^2 + 2\pi \int_{R_{TF}}^{\infty} V_0 e^{-\frac{r^2}{2d_p^2}} r dr \tag{4.13}$$

$$= \pi R_{TF}^2 + V_0 d_p^2 e^{-\frac{R_{TF}^2}{2d_p^2}}$$

$$= d_p^2 (2\pi \log(V_0) + 1). \tag{4.14}$$

It is worth emphasising that the added mass depends on the geometry

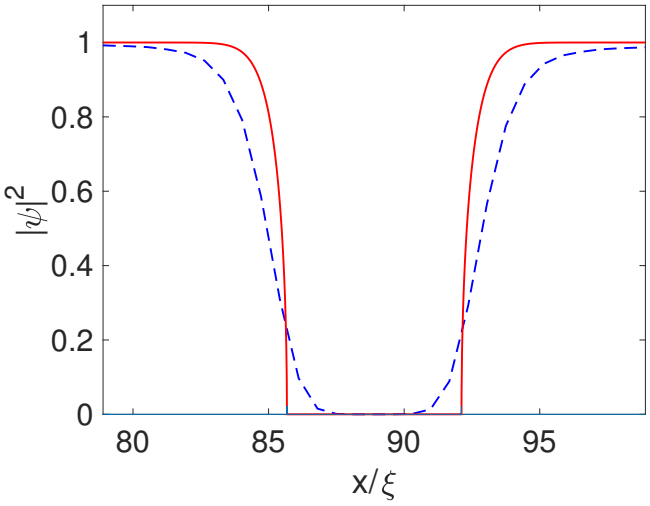

FIGURE 4.1: Density profile of particle and TF profile: The density profile of the simulated particle is blue (dashed), The TF profile is red, both with the same parameters, $V_0 = 10g\rho_0$ and $d_p = 1.5\xi$.

of the particle, and in the case of an arbitrarily shaped particles further considerations are required compared to what we wish to address in the present study. For the parameters used in this study, we find m' to be 46.69.

We use the added mass m' of the displaced superfluid from the TF profile to define the ratio

$$\mathcal{M} \equiv \frac{m_0}{m'}, \tag{4.15}$$

which allows us to distinguish between heavy ($\mathcal{M} > 1$), neutral ($\mathcal{M} = 1$) and light ($\mathcal{M} < 1$) particles. We emphasise here that the added mass in

general differers from the displaced mass; however, for disk shaped particles they are identical. This is important as the added mass can depend on the geometry of the particle. Consider a triangle shaped particle. The added mass will be smaller on the vector pointing to the vertices of the triangle and much larger for the edges. This is the same as saying a triangle is more aerodynamic in some directions.

We express the MFM equations in a more compact form as

$$\ddot{z}_j = iA(w_j - \dot{z}_j) + G/(m_0 + m'), \tag{4.16}$$

where $z_j = x_j + iy_j$, $w_j = u_j + iv_j$ and $G = G_x + iG_y$.

We can easily extend our 2D MFM to 3D by using the Local Induction Approximation (LIA) of the Biot-Savart law, wherein a vortex element $\mathbf{s}$ of a vortex line at the arc length ζ and time t has velocity[94]

$$\dot{\mathbf{s}}(\zeta, t) = \beta \mathbf{s}' \times \mathbf{s}'', \tag{4.17}$$

where the overhead dot and prime correspond to derivatives with respect to the time and arclength, respectively; $\beta = \log(l/\xi)$ and l is a suitable cut-off length scale that is approximately equal to the mean curvature radius.

Therefore, in 3D the dynamics of the vortex-line, with uniform mass distribution, is given by

$$\ddot{\mathbf{q}} = A\mathbf{s}' \times (\dot{\mathbf{q}} - \dot{\mathbf{s}}(\zeta, t)), \tag{4.18}$$

where $\mathbf{q}(\zeta, t)$ is the position of the particle. This equation corresponds to a vortex line with test particles densely filling its core. Another interpretation could be normal fluid trapped into the superfluid vortex core. Similar to the 2D case, in 3D we can include a short range repulsion between the particles.

The LIA is derived from the more general Biot-Savart law. Using the Biot-Savart description with our model requires more complexity. This is due to the vortex arclength not being conserved in the Biot-Savart description. Thus, a separate equation for the mass density along the vortex line would be required.

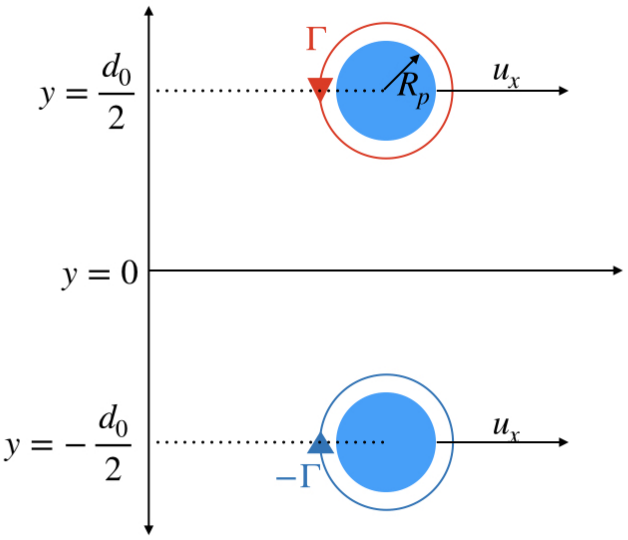

FIGURE 4.2: *(Color online)* Schematic diagram illustrates the initial configuration, wherein a vortex-antivortex pair loaded with particles is translating along the x-axis. Particles are shown by blue disks. The circle with anticlockwise (clockwise) arrow represents a vortex (an antivortex) with circulation vector pointing out of (in) the plane. The centers of the particles (the coincident vortices) are separated by a distance d_0.

II.iv Simplified Magnus force model for particle loaded vortex-antivortex pair

A vortex-antivortex pair of size d_0 is the simplest multi-vortex configuration that occurs in a periodic, 2D domain. This vortex-antivortex pair translates at a speed $u = \Gamma/(2\pi d_0)$ in a direction perpendicular to the line joining the two vortices (See Fig. 4.2). Therefore, the dynamics of the two particles $\mathcal{P}_1$ and $\mathcal{P}_2$ trapped on the vortex and antivortex, respectively, serves to provide a simple demonstration of the Magnus effect.

To simplify our discussion, we assume that the y-component of the velocity of the underlying flow experienced by the particles is zero, i.e. $v = 0$ in Eqs. (4.6) and (4.7). Also, we consider a large vortex-antivortex pair, $d_0 \gg R_p$, that allows us to neglect the short-range repulsion. As our vortex-antivortex pair is symmetric about the x-axis (See Fig. 4.2), in what follows we discuss the dynamics (trajectory) of only one particle. The equation of motion for the particle is then given by

$$\ddot{x} = -A\dot{y}, \tag{4.19}$$

$$\ddot{y} = -A(u(y) - \dot{x}). \tag{4.20}$$

To further simplify the discussion, we impose a condition that the horizontal component $u(y) =$ constant during the dynamical evolution of this system, thereby furnishing a readily solvable set of coupled ODEs. Hereafter, we refer to this model as the simple Magnus force model (SMFM). In SMFM, with the initial conditions

$$\begin{aligned} x(0) &= x_0 & y(0) &= y_0 \\ \dot{x}(0) &= 0 & \dot{y}(0) &= 0, \end{aligned} \tag{4.21}$$

the particle trajectory is of the following form:

$$x(t) = x_0 + ut - \frac{u}{A}\sin(At), \tag{4.22}$$

$$y(t) = y_0 - \frac{u}{A}(1 - \cos(At)). \tag{4.23}$$

Note that this rather restrictive description is valid only when the oscillations of the particles are small.

In the present study, we compare the predictions of the MFM and SMFM against the GP description to illustrate the Magnus effect. Therefore, it is important to recognise the fact that due to the periodicity of the phase of the wave function representing the vortex-antivortex pair within the GP description in a 2D periodic domain, the motion of the pair is altered as compared to that in the ideal fluid. We discuss this in detail in section III, where we provide a detailed comparison of the vortex-antivortex pair

dynamics in the GPE and the ideal fluid case (Weiss-McWilliams formula).

III Weiss-McWilliams formulae for ideal fluids and GP system

The adaptation of the Weiss-McWilliams formula for the translational velocity of a vortex-antivortex pair in an ideal fluid to the GPE system with a periodic domain requires a modification because of the periodicity of the phase of the wave function in the latter. Below we demonstrate this for a vortex-antivortex pair, which we then generalize to the case of N-pairs.

Consider a vortex-antivortex pair, translating along the x-axis with vortex at $(x, \pi + d/2)$ and antivortex at $(x, \pi - d/2)$. Now let us consider the circulation along three lines $\mathcal{C}_i$ for $i = 1, 2, 3$, as shown in Fig. 4.3:

$$\mathcal{C}_i(d) = \int_0^{2\pi} u(x, y_i)dx, \tag{4.24}$$

where $0 < d < 2\pi$; $0 \leq y_1 < \pi - d/2$; $\pi - d/2 < y_2 < \pi + d/2$ and $\pi + d/2 < y_3 \leq 2\pi$. These contours can be closed by joining $x = 0$ and $x = 2\pi$, without generating any contribution to the circulation, as guaranteed by the periodic boundary condition. Thence,

$$\mathcal{C}_1 - \mathcal{C}_2 = -\Gamma, \tag{4.25}$$

$$\mathcal{C}_2 - \mathcal{C}_3 = \Gamma, \tag{4.26}$$

$$\mathcal{C}_1 = \mathcal{C}_2 - \Gamma = \mathcal{C}_3, \tag{4.27}$$

for the contours enclosing vortices. The circulation can now be solely expressed as a function of the y-position of the contour and the separation between the vortices:

$$\int_0^{2\pi} u(x, y)dx = \mathcal{C}(y, d) = \int_0^{2\pi} -\frac{\partial h}{\partial y}dx \tag{4.28}$$

where h is the stream function and $u = -\partial h/\partial y$. Let us define the mean velocity

$$\bar{u} = \frac{1}{(2\pi)^2}\int_0^{2\pi} \mathcal{C}(y,d)dy \tag{4.29}$$

$$= \frac{1}{(2\pi)^2}\int_0^{2\pi}\int_0^{2\pi} u(x,y)dxdy. \tag{4.30}$$

From the periodicity of stream function it follows that the mean velocity is zero. The integral in (4.30) can be then computed as a sum of the areas multiplied by the circulation, that is,

$$\left(\pi - \frac{d}{2}\right)\mathcal{C}_1 + \mathcal{C}_2 d + \left(\pi - \frac{d}{2}\right)\mathcal{C}_3 = 2\pi\mathcal{C}_1 + \Gamma d$$

$$= 0, \tag{4.31}$$

by using equation (4.27). Thus $\mathcal{C}_1 = -\Gamma d/(2\pi)$ for a system with a periodic stream function. Note that the Euler equations are Galilean invariant and any constant velocity can be added to the system which corresponds to moving to a different inertial frame. However, the requirement that the streamfunction is periodic fixes the frame of reference such that the mean velocity is zero. This is the choice of frame in Ref. [119]. Such a choice is inconsistent with the periodicity of the wave function, as it would result in a phase change which is not an integer multiple of 2π (for $\Gamma = 2\pi, \mathcal{C}_1 = d \neq 2\pi n$). Therefore, if we want to use the Weiss-McWilliams prescribed velocity (ideal fluid case), we must work in a frame in which the phase of the wave function is periodic. Thus, we must add a constant background velocity equal to $\mathcal{C}_1/2\pi$.

Note that in order to be consistent with the contents of the main text, in our discussion here, we have used a vortex-antivortex pair that is only separated along the y-direction. However, our arguments are still valid if the vortices are separated in the x-direction as well. In which case, we simply have to repeat the argument with vertical contours which separate the vortices to find the contribution to the y-component of the velocity.

Moreover, our discussion here is generalisable to the case of $2N$ vortices,

with an equal number of vortices and antivortices. This is so because the system is linear, i.e., the contribution to the velocity field is additive. Also, the argument is valid, as the sum of the periodic phases will also be periodic. Therefore, for a system of $2N$ vortices, the additional background velocity $\mathbf{u_b}$ is

$$\mathbf{u_b} = \sum_{i}^{2N} \frac{\Gamma_i}{(2\pi)^2} \hat{\mathbf{e}}_z \times \mathbf{x}_i, \tag{4.32}$$

where $\mathbf{x}_i$ is the position of the ith vortex, which is, up to a constant, the total momentum of the point vortex system.

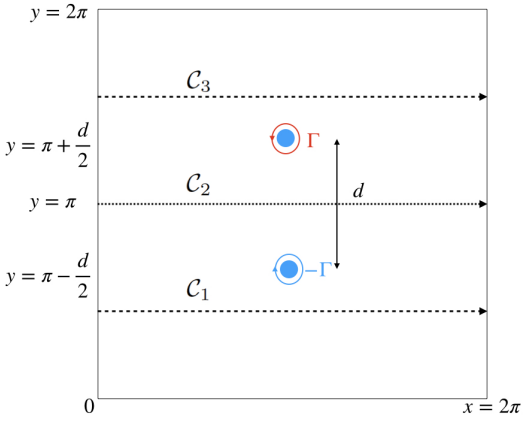

FIGURE 4.3: Schematic of two vortices separated by distance d. Overlaid with the contours on which we calculate the x-contributions of the circulation.

For an odd number of vortices, the system will have a net circulation. Therefore, to make arguments as, we now have to work in a rotating frame of reference. This is same as adding a constant background vorticity, such that the frame has net circulation zero. The ratio between the angular velocity of the rotating frame and the vorticity is a half. Other valid configurations could include constant vorticity such as shear. In this case, such formulation is consistent when periodicity is imposed in sheared coordinates.

In Fig. 4.4 we show the comparison of the vortex-antivortex pair velocity as obtained from the GPE DNS (dashed red curve) and the adapted Weiss-McWilliams formula (blue curve). For very small pair size, we observe a

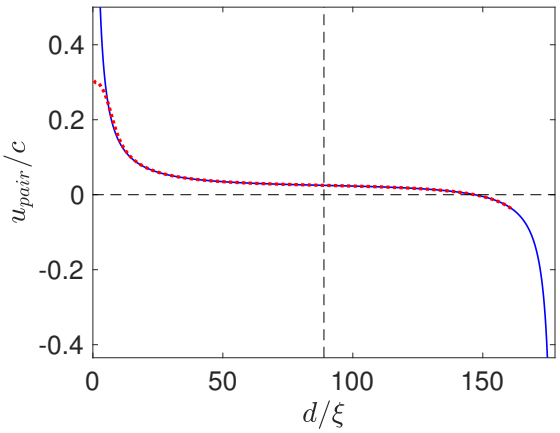

FIGURE 4.4: Velocity of the vortex-antivortex pair as a function of its size. The red dashed curve represent the data obtained from the GPE simulations, whereas the blue solid line indicates the velocity given by the adapted Weiss-McWilliams formula, see text for more details. The black dashed horizontal line indicates $u_{\text{pair}} = 0$ and the black dashed vertical line marks the mid point of the periodic domain.

disagreement, as now the vortex core size is important. At still very small sizes, vortices annihilate and become a localised density perturbations. The original Weiss-Mcwilliams (ideal fluid) x-directional velocity of a vortex pair (as in 4.3) is given by

$$u_{WMc}(d) = -\frac{\Gamma}{4\pi}\sum_{n=-\infty}^{\infty}\frac{\sin(d)}{\cosh(2\pi n) - cos(d)}. \tag{4.33}$$

Therefore, the expression obtained by adapting this to the case of the GPE in a periodic domain is given by

$$u_{pair}(d) = -\frac{\Gamma}{4\pi}\left(\sum_{n=-\infty}^{\infty}\frac{\sin(d)}{\cosh(2\pi n) - cos(d)} + \frac{d}{\pi}\right). \tag{4.34}$$

For our purposes, we calculate the velocity until it has converged within 10^{-9}, this corresponds to retaining 9 terms, i.e. $n = -4$ to $n = 4$. Therefore,

to the leading order

$$u_{pair}(d) = \frac{\Gamma}{4\pi}\left(\frac{1+\cos(d)}{\sin(d)} + \frac{d}{\pi}\right), \tag{4.35}$$

and its derivative with respect to separation is

$$\frac{\partial u_{pair}(d)}{\partial d} = -\frac{\Gamma}{4\pi}\left(\frac{1+\cos(d)}{\sin^2(d)} + \frac{1}{\pi}\right). \tag{4.36}$$

This has a minimum at $d = \pi$, thus the approximation of constant velocity across the particle is most suitable close to half the domain size, $L/2$.

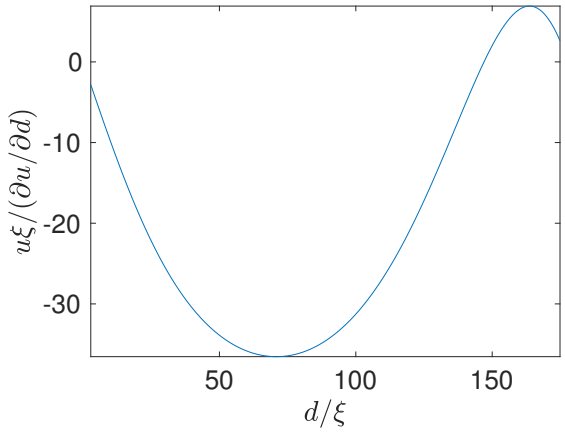

FIGURE 4.5: Derivative of velocity with respect to separation against separation.

IV Results

IV.i Dipole configuration

We first discuss the discuss the dynamics of the particle loaded vortex-antivortex pair, starting with an initial configuration as shown in Fig. 4.2. In Fig. 4.6, we show the pseudo-color plots of the density field $\rho(\mathbf{r})$ overlaid with trajectories of the two particles, along with SMFM predictions (blue dashed curves) given by Eq.(4.22) and Eq.(4.23). We find that the particles follow

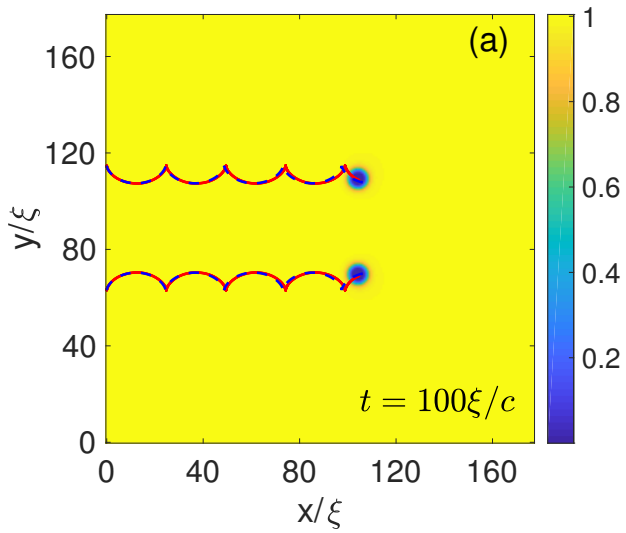

FIGURE 4.6: Trajectories of loaded vortex dipole. Parameters: mass ratio $\mathcal{M} = 17.15$ and initial separation $d_0 = 52.50\xi$. Pseudo-color density ($|\psi(\mathbf{r}, t_f)|^2$) plots with simulated (red) and predicted with MFM (blue dashed) trajectories overlaid.

a nearly cycloid trajectory, in good agreement with the SMFM predictions. The cycloid trajectory of the particles is characterised by the displacement amplitude in the y-direction δ_a and the periodic length X_p in the x-direction. These two quantities are easily deduced from the SMFM (Eqs. (4.22) and (4.23)) yielding $\delta_a = 2u/A$ and $X_p \simeq u2\pi/A$; note the dependence on the flow velocity u.

To better appreciate this dependence, we approximate the flow velocity u by the following three values, with u_{pair} given by Eq. (4.33).

1. $u = u_{pair}(d_0)$;

2. $u = u_{pair}(d_0 - 2\delta_0)$, where $\delta_0 = 2u_{pair}(d_0)/A$ is the amplitude of case (1);

3. u is the mean of the estimates obtained from (1) and (2) above.

In Fig. 4.7 (a) and (b) we show the plots of δ_a/d_0 and X_p/ξ, respectively, vs. $\mathcal{M}$ obtained from the GPE simulations (curves with circles as markers) and the use of the above three test cases for u in SMFM; we do this for

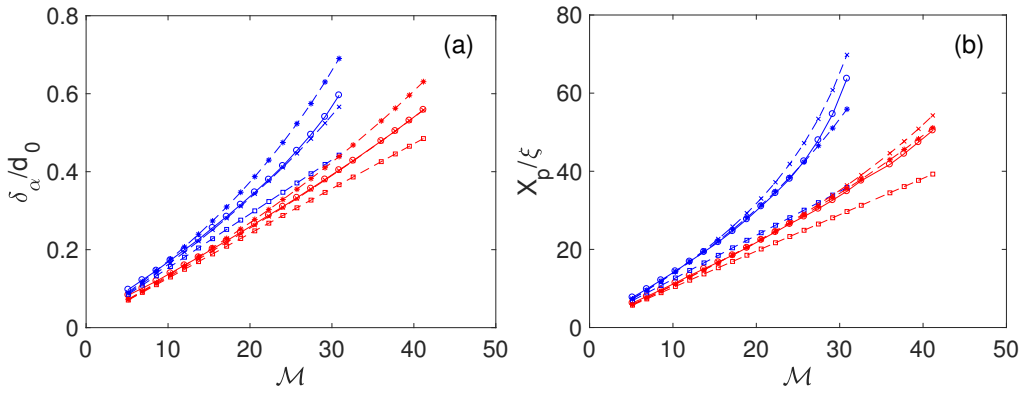

FIGURE 4.7: Amplitude and period analysis of SMFM. All blue (top four) lines correspond to a separation $d_0 = 52.50\xi$ and red lines (bottom four) to $d_0 = 72.41\xi$ with the circles representing simulated data in both (a,b). The other types of line correspond to the fit for a velocity $u_{pair}(d_0)$ (square, case 1 in text), for velocity $u_{pair}(d_0 - 2\delta_\alpha)$ (asterisk, case 2 in text) and average of the other two (cross, case 3 in text). Panel (a): the amplitude δ_α of the cycloid in units of initial separation against mass ratio $\mathcal{M}$. Panel (b): the period X_p against mass ratio $\mathcal{M}$.

two initial values of $d_0 = 52.30\xi$ (blue curves) and $d_0 = 72.41\xi$ (red lines). This exercise reveals a clear dependence of the results on the choice of u; thereby suggesting that in any modelling scheme based on the MFM model, the flow velocity u must be updated in a self-consistent manner. Note that the case (1) is the velocity at the initial time, this also corresponds to the minimum velocity, as the particles are at maximum separation. Case (2), which tends to overshoot, is based on the approximate minimum distance, thus resulting in maximum velocity. Case (3) is a simple average, we see that this predicts well the parameters of the cycloid trajectories for all the simulations.

Also note that in Fig. 4.7 the data for $d_0 = 52.50\,\xi$ and $\mathcal{M} > 30.87$ is absent, as for these values of the parameters the amplitude of the cycloid motion becomes larger than half the initial vortex-antivortex pair size and results in a collision of the two particles, thereby annihilating the vortices. Later (in Fig. 4.10) we show that the model fits well up until the collision.

Now let us recall an assumption of our model, that the flow is uniform

across the particle. This assumption is good as long as the vortex-antivortex pair size is large. However, as the size decreases, the finite size of the particles becomes increasingly important due to the external flow varying over the particle. Despite these restrictions, the analytic model provides a good phenomenological description of the dynamics of the particle loaded vortices.

To improve the simplified model we remove the assumption that the velocity is constant throughout the dynamics, namely, we let the velocity vary depending on the current separation of the particles. We solve the MFM Eqs. (4.6) and (4.7) numerically, while accounting for the variation in $u \equiv u_{\text{pair}}(d(t))$ as the vortex-antivortex pair size varies; this allows us to improve the accuracy. We compare the trajectories of the particles obtained directly from the GP simulations with those predicted by the MFM. We solve the coupled ODEs of the MFM by using the specialised ODE solver ODE45 in MATLAB. We also include the short range repulsion forces as now they are relevant for the cases where our model is tested beyond the formal limit of applicability, namely, when the inequality $\xi \ll R \ll d$ does not hold.

For comparing the above two solutions, we define an average error

$$\epsilon = \sum_{i=1}^{N_t} ((x_s(t_i) - x_p(t_i))^2 + (y_s(t_i) - y_p(t_i))^2)^{1/2}/N_t, \tag{4.37}$$

where (x_s, y_s) are the GP simulated coordinates of the particle and (x_p, y_p) are the coordinates from the simulated ODE. We choose N_t points on each trajectory which are evenly spaced in time. The measure of error, ϵ, is the average distance the predicted value is away from the true value over the entire run, we present this in units of ξ.

In Fig. 4.8, we present two examples ($d_0/\xi = 52.50$ and 72.41) of direct comparison between the particle trajectories obtained from the GP simulations and those predicted by the MFM. Note that we only show the trajectory of the particle trapped on a vortex with positive circulation because of the symmetry. The mismatch between the trajectories gives a visual indication of the error.

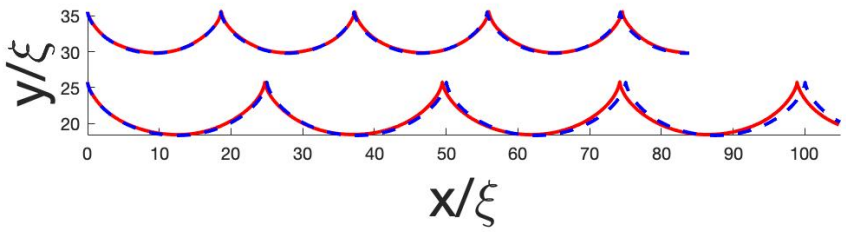

FIGURE 4.8: Trajectory of the loaded upper vortex in the dipole. Example of DNS trajectories (red) compared to predicted trajectories (blue dashed). Two cases show $d_0 = 52.50\xi$ (bottom curve), 72.41ξ (top curve) with $\mathcal{M} = 17.15$. The final time of the simulation is $t_f = 100$.

We perform numerical simulations for a large range of particle masses $\mathcal{M} \in [5, 50]$ for the same two initial separations, keeping the total time of the dynamics fixed at $t_f = 100\xi/c$. We then compute the error ϵ and present the results in Fig. 4.9 (a). We observe that the error for all simulations stays of the order of a healing length. Surprisingly, we see that as the mass grows the error decreases for the pair with larger initial separation. As we increase the mass, we expect that the particle is less sensitive to compressibility effects. We also note that for a greater mass, the amplitude of the cycloid for a given initial position is larger. We see the effect of this on the pair with smaller initial separation. The error grows rapidly as the mass approaches $\mathcal{M} = 30$ at this point, the particles collide, causing the vortices to annihilate. In general, the model predicts the behaviour of more massive particles more accurately as long as the inequality $\xi \ll R \ll d$ holds. However, increasing the mass causes larger amplitudes, subsequently causing the inequality to break.

In another protocol, we keep the mass fixed at $\mathcal{M} = 17.15$ and vary the initial size of the vortex-antivortex pair. The nonlinear shape to this error is again due to competing assumptions of our model. For low separations the finite size of the particle becomes important, thus we see high error. We conjecture that the minimum that follows is due to the change in velocity due to the separation, $(\partial u/\partial d)2R$, becoming small compared to the velocity,

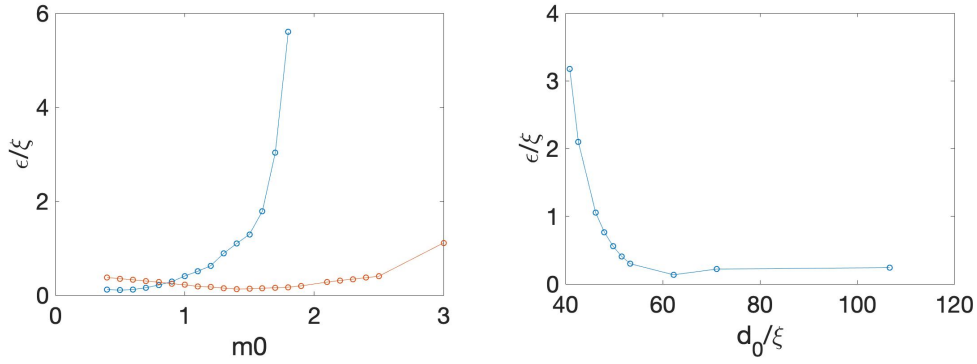

FIGURE 4.9: Error with simple dipole configuration. Panel (a): two cases show $d_0 = 52.50\xi$ (blue) and 72.41ξ (red) for a range of different masses. For values of $\mathcal{M}$, greater than 30.87 the particles have collided for $d_0 = 52.50\xi$ (blue), so they have been omitted. Panel (b): For $\mathcal{M} = 17.15$ with a range of different initial distances.

see Fig. 4.5 in Section III. The error always stays of the order of a healing length. This clearly demonstrates the usefulness of a simple ODE based MFM model, which is easily solved numerically and able to capture the phenomenological motion of the vortices loaded with particles. Moreover, it predicts their motion to high accuracy.

Above examples show that the MFM model provides good description for a simple configuration. Now we extend its use to predict more complex configurations.

As mentioned earlier, one of the limitations of our model is that it does not capture the possible annihilation of vortices during a collision event. This process plays an essential role in the dynamical evolution of an assembly of vortices in 2D in the presence of particles, which can potentially increase the annihilation rate [100]. This has implications for the quench (relaxation) dynamics of the 2D superfluid system, which undergoes the Berezinskii-Kosterlitz-Thouless (BKT)[15, 58] phase transition (transition in long range order of the fluid) via a vortex annihilations. Consequently, the increased annihilations in 2D and vortex reconnections in 3D will have a strong influence the velocity statistics in a turbulent state.

In Fig. 4.10 we show that the model describes the dynamics well up until

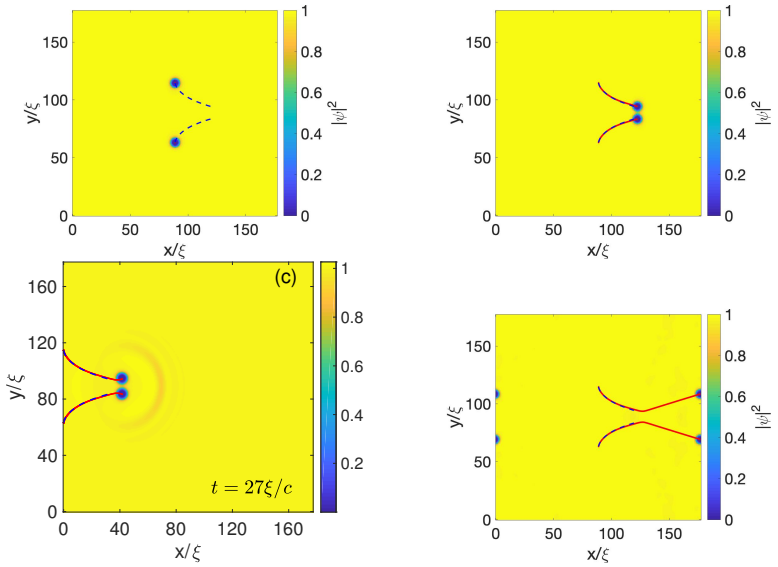

FIGURE 4.10: Collision of loaded vortices. Parameters: mass ratio $\mathcal{M} = 36.02$ and separation $d_0 = 52.5\xi$. Psuedo-color density ($|\psi(\mathbf{r}, t_f)|^2$) plots with DNS (red) and MFM (blue dashed) trajectories overlaid with time presented in the each panel. Sound produced during annihilation can be seen as variations in the psuedo-color density. The MFM trajectories are only presented up until the collision.

a collision in which the vortices annihilate. The annihilation is followed by linear motion of the particles, with the particles conserving their momentum from the collision. Although the current models do not account for the annihilations, this feature can be added in a ad hoc manner, for example as in Ref. [7]. To add this we require further study of the collisions to define some particle separation cut off value for which the vortices annihilate. In order to define such a cut off we need to study the different possible dynamics during such a collision and to further understand the exchange of momentum of the particles and the role of the acoustic component. However, this is beyond the scope of the current work.

IV.ii More complex configurations

We studied the case of particles on vortices in a dipole configuration in detail. We now want to briefly consider further configurations to see how

the model performs in more complex set-ups.

It is well known that vortices with more than one quanta of circulation are unstable [95, 76] and move apart due to the emission of sound due to the rotational acceleration. There have been studies on the role of static potentials in stabilising the vortices [109, 48]; however, this can be extended to cases with external flows and dynamic potentials like the particles presented here. We show that the particles can be used to add stability and to create a localised region in a flow with circulation larger than one quanta.

We consider a vortex-antivortex pair configuration similar to that in Fig. 4.2, but where each vortex has two quanta of circulation and a particle trapped on it. Such a system exhibits an exciting dynamics, it remains stable, i.e. both vortices remain on the particle, up until the collision. We show the collision of the particles in Fig. 4.10, where on colliding only one of the pairs is annihilated via the emission of an unstable Robert-Jones[53] soliton. The other pair remains on the particles, continuing to propagate, with the dynamics being captured by the MFM. Figure 4.11 shows that the MFM can successfully model the post-collision dynamics. We initialise the MFM with a position and velocity taken from the simulated GP data after the collision. Even in the presence of considerable background sound waves, we obtain an excellent agreement with the GP dynamics, with the error being $\epsilon = 2.74\,\xi$. The fact that the collisional interaction exhibits annihilation of only a single vortex-antivortex pair merits further investigation, as it is not trivial to understand why the entire vortical charge on the particle was not annihilated. This example also emphasises how particles can change the dynamics of a simple configuration, and that reconnection events may be more common when vortices are loaded with particles.

To further increase the complexity, we consider a final example in which free vortices (i.e. vortices not loaded with particles) are positioned in front of a vortex-antivortex pair loaded with particles, in the latter each vortex has two quanta of circulation. We compute the motion of the free vortices using (4.33) such that the velocity contributions from the vortices loaded with particles are the same as if they were free vortices. The motion of the particles is once again calculated by numerically solving the Eqs. (4.6) and (4.7); however, the velocity field is more complicated now. This model is

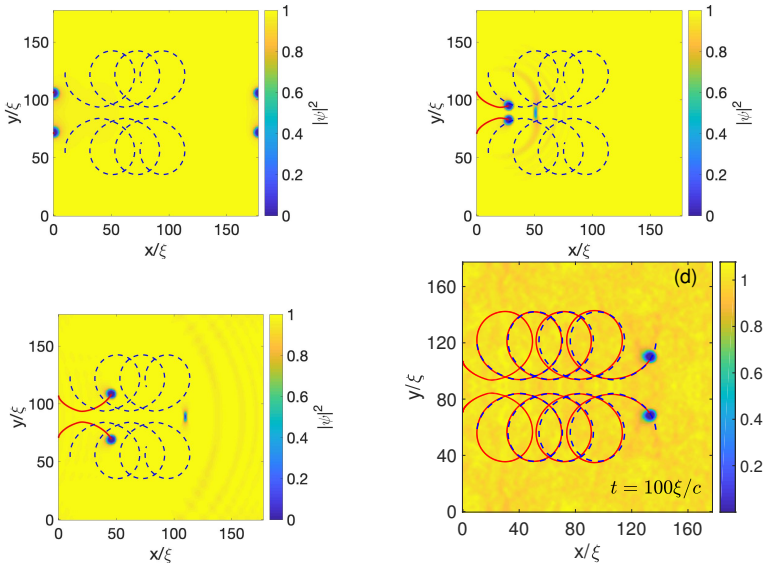

FIGURE 4.11: Multiple vortices on particles: Pseudo-color density ($|\psi(\mathbf{r}, t_f)|^2$) plots with DNS (red) and MFM (blue dashed) trajectories overlaid at different times as presented in the panel. The MFM trajectories are only calculated post-collision. Initially each particle has two vortices or two quanta of circulation on its core. The Robert-Jones soliton is shown by large density change in (b) and (c).

more general as it can handle a combination of free vortices and vortices trapped on particles; we will refer to this as PV+MFM (Point vortex and Magnus force model). We employ a simple Euler method to advance in time, with the velocity field coupling the two motions. The model predicts well the general motion not only of the particle, and also the free vortices as seen in Fig. 4.12. The average error of the model is 3.57ξ, and one can see in FIG. 4.12 that with the additional complexity the dynamics are captured phenomenologically.

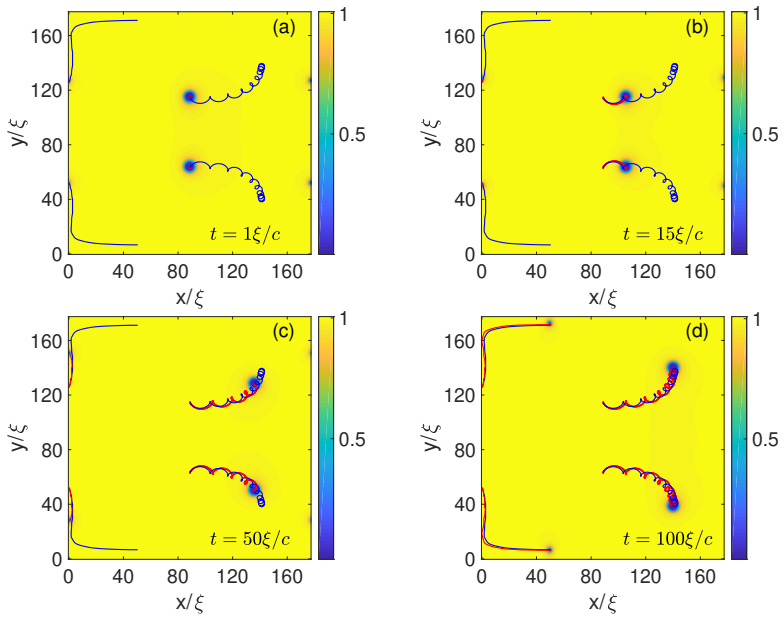

FIGURE 4.12: Free vortices and loaded vortices. Parameters: mass ratio is $\mathcal{M} = 17.15$ and initial separation $d_0 = 52.5\xi$. Pseudo-color density ($|\psi(\mathbf{r}, t_f)|^2$) plots with DNS (red) and PV+MFM (blue) trajectories of particles and free vortices overlaid. The smaller disks in the pseudo-color density plots are free vortices. The DNS (red) and PV+MFM (blue) are overlaid and are difficult to distinguish (see color online).

V Conclusions

We have shown that the particles trapped on vortex cores experience a Magnus force in the presence of neighbouring vortices or a relative background flow. For simple configurations, where the flow velocity is known, this method can be employed to efficiently predict particle trajectories. It is also possible to generalise our model in the presence of many free vortices by accounting for their motion using the usual point vortex expressions. The MFM predictions are good enough, as long as we can ignore the finite size of the particles, e.g., for large size vortex-antivortex pairs, where it fits well even for massive particles. The model performs well outside of its formal limits of applicability.

The MFM description naturally extends to 3D by combining the model with the LIA, we hope to further develop the method beyond LIA and incorporate the full BS description in future work. Our model can be generalised to include cases in which annihilation takes place and of course, describes well the post-collision dynamics. Further work could focus on how the attractive forces added to vortices can increase vortex annihilations and further aid phase transitions like the BKT phase transition. The development of a simple theoretical framework which accounts for the motion of particles in the presence of vortices would significantly improve the ability to study the effect of particles in superfluid turbulence. We could algorithmically add annihilations of vortices and vortices on particles much using similar methods which are commonly used[6]; this will be the subject of future work. To do this, we would need to choose some physical cut-off value of the particle separation for which vortices annihilate. This could be found by further studies into the annihilation of vortices in the presence of external potentials. However, with the current model we have a fast and accurate way to simulate 2D turbulence interacting with tracer particles.

Chapter 5

Steady states in Leith's model of turbulence

I Introduction

Leith's model of turbulence is a nonlinear degenerate inhomogeneous parabolic equation with absorption of the form [64, 81, 28]:

$$\frac{\partial E}{\partial t} = \frac{1}{8}\frac{\partial}{\partial k}\left(k^{\frac{11}{2}}E^{\frac{1}{2}}\frac{\partial}{\partial k}\left(k^{-2}E\right)\right) - \nu k^z E, \tag{5.1}$$

where $E \equiv E(k,t)$ is the one-dimensional energy spectrum, k is the absolute value of the wave number, $\nu = \text{const} > 0$ is a viscosity coefficient and $z = \text{const} > 0$ is the degree of the viscous dissipation. The usual kinematic viscosity corresponds to $z = 2$, friction dissipation—to $z = 0$, hyper-viscous dissipation (often used in numerics)—to $z > 2$. We will be interested in the stationary version of this equation:

$$\frac{1}{8}\frac{\partial}{\partial k}\left(k^{11/2}E^{1/2}\frac{\partial}{\partial k}\left(E/k^2\right)\right) = \nu k^z E. \tag{5.2}$$

Quantity

$$\epsilon(k) = -\frac{1}{8}k^{11/2}E^{1/2}\frac{\partial}{\partial k}\left(E/k^2\right) \tag{5.3}$$

has the meaning of the energy flux through k. Clearly $\epsilon(k)$ is always a monotonically decreasing function for $\nu > 0$ and constant for $\nu = 0$.

Transient solutions of the inviscid Leith model, i.e. equation (5.1) with $\nu = 0$, arising from an initial spectrum compactly supported at low k were

investigated in [81, 28]. These solutions precede the formation of a steady cascade in the full Leith model. It was shown that this regime becomes self-similar just before the breaking of the energy conservation (which occurs once the cascade has proceeded far enough to generate a finite flux of energy to $k = \infty$). This regime is interesting because it does not exhibit the scaling inherited from the Kolmogorov spectrum. Namely, the transient spectrum was found to have a power-law asymptotics with an exponent which is smaller than the Kolmogorov index. The self-similar solutions which were analyzed numerically in [81] have a "sharp" nonlinear front which accelerates explosively reaching $k = \infty$ at a finite time $t = t_*$. In [43] they recovered this result analytically and established the existence of a self-similar solution with a power-law asymptotic on the low-wavenumber end and a sharp boundary on the high-wavenumber end which propagates to infinite wavenumbers in a finite-time t_*. It was shown that such a self-similar solution is realised by a heteroclinic orbit of the corresponding dynamical system. It was proven that this solution has a power-law asymptotic with an anomalous exponent x^* which is greater than the Kolmogorov value, $x^* > 5/3$, and less than value $x_2 \approx 1.95$ corresponding to a Hopf bifurcation. The existence of weak solutions (the spectrum evolving from an arbitrary finitely supported initial data) of the initial-boundary value problem was proven and convergence to the self-similar solution as $t \to t_*$ was established. In paper [23], the symmetry analysis was applied to describe all essentially different invariant solutions of the Leith model with or without viscosity.

The present paper is devoted to the study and full classification of the stationary solutions of the Leith model (5.1). In absence of viscosity, the general stationary solution was found in [81, 28]:

$$E_{P,Q}(k) = ck^2(Pk^{-11/2} + Q)^{2/3}, \tag{5.4}$$

where $c = (24/11)^{2/3}$ and P and Q are arbitrary constants. For $Q = 0$, this gives the pure Kolmogorov cascade solution, whereas for $P = 0$ this is a pure thermodynamic spectrum. For the general solution, both the constant flux energy $\epsilon(k) = P = \text{const} \neq 0$ and a thermodynamic part $Q \neq 0$ are present as a nonlinear combination which is a nonlinear mixture

of the Kolmogorov cascade (dominating at small k) and a thermal Rayleigh-Jeans spectrum (dominating at large k). Respectively, solution $E_{P,Q}$ with $P, Q \neq 0$ was called a "warm cascade" spectrum in [81, 28]. Such a warm-cascade solution describes a bottleneck phenomenon of spectrum stagnation near the dissipative scale. It is a prototype of the bottleneck phenomenon in the numerical simulations of the Euler (inviscid) turbulence using spectral methods, where the energy spectrum accumulates at high wavenumbers near the truncation wavenumber [25]. It also similar to a real physical bottleneck phenomenon in superfluid turbulence—an energy accumulation at the classical-quantum crossover scale, an effect predicted in [68].

The bottleneck effect was shown to exist, although in a much milder form, in viscous (Navier-Stokes) fluids too, even without a cut-off wave number [34]. It was explained in Ref. [34] by using the fact that the Navier-Stokes are nonlocal in the k-space.

In the present paper we will study the stationary solutions of the viscous Leith model, i.e. solutions of equation (5.1). We will see that the inviscid warm-cascade spectra (5.4) still play an important role in some relevant asymptotic regimes. However, we will see that in absence of a maximum (cut-off) wave number such spectra (or any milder bottleneck) require presence of an extra energy source at $k = \infty$. This results agrees with the view of Ref. [34], nonlocality of interaction in the k-space is important—the property absent in the Leith model. However, we will see that the warm-cascade described by the Leith model is still relevant to the situations where a maximum (cut-off) wave number is naturally present.

The present paper is structured as follows. In Section II, we perform the change of independent and dependent variables which transforms the stationary viscous Leith's type model into an autonomous nonlinear ordinary differential equation. The corresponding dynamical system is presented and its fixed points are found and classified. This is followed by an analysis of the inviscid asymptotics and the power-law scalings, and the behavior of solutions near a sharp front, where both the stationary spectrum $E(k)$ and the flux of energy are vanishing. Section III is devoted to a qualitative analysis of the dynamical system based on phase portraits for different values of z found numerically. The solutions are interpreted in terms of their physical

meanings as low and high Reynolds number direct and inverse energy cascades. Appendix B is devoted to rigorous proofs of the assertions made in Section III, including the formulation of relevant types of Cauchy problems, studying their solvability and identifying several classes of qualitatively different solutions, their dependence on z and on the initial conditions. The full classification is given in terms of the three sets of the qualitatively different orbits existing for any z. A summary and discussion of results is given in Section IV.

II Autonomous dynamical system and its basic solutions

II.i The stationary model as an autonomous dynamical system

To introduce into consideration the autonomous dynamical system, we change variables as

$$s = \ln\left(k/k_0\right), \quad E = k^{2z-3} f^2, \tag{5.5}$$

where k_0 is the left or right (depending on the particular problem) boundary of the considered k-range. Then equation (5.2) is transformed into the following autonomous ODE,

$$2f\frac{d^2 f}{ds^2} + 4\left(\frac{df}{ds}\right)^2 + (12z-19)\, f\frac{df}{ds} + Df^2 = 8\nu f, \tag{5.6}$$

where

$$D = (3z-2)\,(2z-5)\,.$$

For the flux (5.3), we have in terms of f and s:

$$\epsilon(s) = -\frac{1}{8} e^{(3z-2)s}\left[(2z-5)f^3 + f^2\frac{df}{ds}\right]. \tag{5.7}$$

Since $\epsilon(k)$ is always a monotonically decreasing function for $\nu > 0$, $\epsilon(s)$ is also always a monotonically decreasing function for $\nu > 0$.

We can write equation (5.6) in the form of a dynamical system in $2D$ phase space by introducing a new variable g via

$$\frac{df}{ds} = (f+g)\,. \tag{5.8}$$

Then from (5.8) and (5.6) we have

$$2f\frac{dg}{ds} + 2f\,(f+g) + 4\,(f+g)^2 + (12z-19)\,f\,(f+g) + Df^2 = 8\nu f. \tag{5.9}$$

Notice that (5.9) is singular at $f=0$. To remove the singularity, we introduce a new "time" variable τ by

$$\frac{d}{d\tau} = f\frac{d}{ds},$$

and as a result the dynamical system reads

$$\frac{df}{d\tau} = (f+g)\,f, \tag{5.10}$$

$$\frac{dg}{d\tau} + 2\,(f+g)^2 + \left(6z - \frac{17}{2}\right) f\,(f+g) + \frac{D}{2}f^2 = 4\nu f. \tag{5.11}$$

For equilibria we have either $f=0$, $g=0$ or

$$f+g=0, \quad Df^2 = 8\nu f.$$

Therefore, we always have fixed point $P1 = (0,0)$, and sometimes also fixed point $P2 = \frac{8\nu}{D}\,(1,-1)$. The latter exists only for $D>0$ since from the physics f must be a non-negative function. A linearised version of the dynamical system near the fixed point $P1=(0,0)$ reads

$$\frac{d}{d\tau}\begin{pmatrix} f \\ g \end{pmatrix} = 4\nu \begin{pmatrix} 0 & 0 \\ 1 & 0 \end{pmatrix}\begin{pmatrix} f \\ g \end{pmatrix} \tag{5.12}$$

with degenerate eigenvalues $\lambda_1 = \lambda_2 = 0$ and a single eigenvector $(0, 1)$. Correspondingly, near $P2$ we have the following linearised system,

$$\frac{d}{d\tau}\begin{pmatrix} f \\ g \end{pmatrix} = \frac{8\nu}{D}\begin{pmatrix} 1 & 1 \\ -\frac{1}{2}D - A & -A \end{pmatrix}\begin{pmatrix} f \\ g \end{pmatrix}, \tag{5.13}$$

where $A = 6z - \frac{17}{2}$. The eigenvalues are given by

$$\lambda_\pm = \frac{4\nu}{D}\left(\frac{19}{2} - 6z \pm \sqrt{24z^2 - 76z + 281/4}\right).$$

The expression under the square root is always positive. However, $P2$ exists only for $z < 2/3$ and $z > 5/2$. We have stability if $z > 19/12$ and instability otherwise. Thus, $P2$ is an unstable node for $z < 2/3$ and a stable node for $z > 5/2$.

II.ii Asymptotes to inviscid solutions

Let us assume that z is of order one and not too close to $2/3$ or $5/2$. Then it is clear from (5.11) that the viscous term can be neglected if $f \gg \nu$ or/and $|g| \gg \nu$. Thus, the general stationary solution for regions $f \gg \nu$ or/and $|g| \gg \nu$ is given by the warm-cascade spectrum (5.4). If both P and Q are positive then such a spectrum grows unbounded at both small and large k. However, we will see later that solutions with either P or Q (but not both simultaneously) negative are also of interest. Cases $P < 0, Q > 0$ and $P > 0, Q < 0$ correspond to solutions that have a sharp front on the left and the right sides of the k-range respectively. Both types are bounding solutions for orbits in the case with $\nu > 0$ and same values of P and Q at large f.

II.iii Power law scalings

For reference, let us first find power-law solutions in the inviscid case ($\nu = 0$), i.e. $E(k) \sim k^{-x}$. We have

$$f = k^{\frac{3-2z}{2}} E^{1/2} = k^{\frac{3-2z-x}{2}} \tag{5.14}$$

and respectively

$$g = \partial_s f - f = \frac{1 - 2z - x}{2} k^{\frac{3-2z-x}{2}}. \tag{5.15}$$

This corresponds to $f(s)$ in the form $f \sim e^{ps}$ with $p = (3 - x - 2z)/2$. Then from (5.6) with $\nu = 0$ we have: $6p^2 + (12z - 19)\, p + D = 0$, i.e. $p = (19 \pm 11)/12 - z$. Here, the plus sign corresponds to the thermodynamic and the minus to the Kolmogorov spectra. For Kolmogorov solution (corresponding to $Q = 0$ in the mixed solution (5.4)):

$$f_{P,0} = e^{(2/3-z)s} = k^{2/3-z}. \tag{5.16}$$

In this case $f_{P,0}$ is an increasing function of k if $z < 2/3$, constant for $z = 2/3$, and decreasing otherwise. For thermodynamic solution ($P = 0$):

$$f_{0,Q} = e^{(5/2-z)s} = k^{5/2-z}. \tag{5.17}$$

In this case $f_{0,Q}$ is an increasing function of k if $z < 5/2$, constant for $z = 5/2$, and decreasing otherwise.

Pure power-law Kolmogorov and thermodynamic spectra are not solutions when $\nu \neq 0$. However, in this case there also exists a power law solution—it corresponds the fixed point $P2$. For such a "viscous scaling" we have f constant so that $x = 3 - 2z$. If the viscous scaling is steeper than Kolmogorov, it will be observed on the low-k side of the spectrum. This occurs for $3 - 2z > 5/3$ i.e. for $z < 2/3$.

For the ratio we have $g/f = (1 - 2z - x)/2$. For Kolmogorov solution:

$$g_{P,0}/f_{P,0} = -1/3 - z. \tag{5.18}$$

For thermodynamic solution:

$$g_{0,Q}/f_{0,Q} = 3/2 - z. \tag{5.19}$$

II.iv A sharp-front solution

Let us analyse the behaviour of solutions of equation (5.2) under the assumption that there exists a finite point k_* where the stationary spectrum $E(k)$ and the energy flux ϵ, are vanishing, which implies

$$E(k_*) = dE(k)/dk|_{k=k_*} = 0. \tag{5.20}$$

Let us seek a solution of equation (5.2) for $k < k_*$ in the form

$$E(k) = A(k - k_*)^y. \tag{5.21}$$

Assuming that $k_* - k \ll k_*$, in the leading order in $(k_* - k)/k_*$ by direct calculation we have

$$y(3y/2 - 1)k_*^{11/2-2}A^{1/2}(k - k_*)^{3y/2-2} = 8\nu k_*^z(k - k_*)^y. \tag{5.22}$$

From here it follows that $y = 4$ and $A = 4\nu^2 k_*^{2z-7}/25$. Therefore the function

$$E(k) = \frac{4\nu^2 k_*^{2z-7}}{25}(k - k_*)^4 \tag{5.23}$$

satisfies equation (5.2) and the condition (5.20). For the phase variables f and g we have respectively

$$f = k_*^{\frac{3-2z}{2}} A^{1/2}(k - k_*)^2, \tag{5.24}$$

$$g \approx \partial_s f = 2A^{1/2}k_*^{\frac{5-2z}{2}}(k - k_*) = -(\nu f/5)^{1/2}. \tag{5.25}$$

This solution corresponds to the motion in a small vicinity of fixed point $P1$ on its slow manifold (both its stable and the unstable parts). It is not captured by the linear analysis near $P1$ because such motion is nonlinear due to the zero eigenvalue. Note that there is no k_* dependence in this expression. Solutions with different k_* (and therefore with different energy flux) correspond to the same orbit, namely the slow manifold of $P1$. The different energy flux corresponds to different choices of the initial wave number. For example, we fix the flux if we specify condition $f(k_0) = f_0$: then the value f_0 will correspond to a unique starting point on the slow manifold. Thus,

the "time" to the collapse is uniquely determined by the starting point on the slow manifold i.e. $s_* = \ln(k_*/k_0)$ will be a unique function of f_0.

Note that there is also another orbit connecting to the fixed point from the positive side. Asymptotic consideration similar to the one above give for this orbit

$$g \approx \partial_s f = 2A^{1/2} k_*^{\frac{5-2z}{2}} (k - k_*) = (\nu f/5)^{1/2}, \tag{5.26}$$

where now the cut off is on the left side, $k_* < k$.

III Phase analysis of orbits: qualitative considerations and overview of results

The easiest way to understand the main features of the steady state solutions for different parameter values is to consider the phase space plots of the respective dynamical systems. There are three qualitatively different cases: $z < 2/3$, $2/3 < z < 5/2$ and $z > 5/2$; see Figures 5.1, 5.2 and 5.3 respectively. As we said before, there are two fixed points for $z < 2/3$ and $z > 5/2$, ($P1 = (0.0)$ and $P2 = (8\nu/D, -8\nu/D)$, and only one for $2/3 < z < 5/2$, ($P1 = (0.0)$). The Kolmogorov and the thermodynamic scalings correspond to straight lines with slopes $-1/3 - z$ and $3/2 - z$ respectively. Since $z > 0$, the Kolmogorov slope is always negative and below the thermodynamic one (the latter is positive for $z < 3/2$ and negative otherwise). It is also instructive to mark the line $g = -f$ where the orbits are vertical (have an infinite slope), i.e. $f(s)$ reaches a local maximum or minimum. This line passes through $P2$ when the latter exists.

III.i Separatrices

The most physically important orbits are represented by separatrices. These solutions are generic in the sense that they correspond to a single energy source at one of the ends of the k-range and no sinks (i.e. the energy is dissipated by the viscosity only).

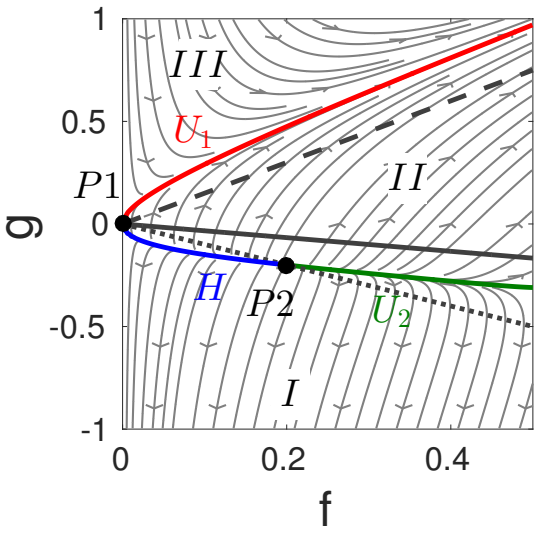

FIGURE 5.1: Case $z < 2/3$. Phase portrait for $z = 0, \nu = 1/4$. The solid straight line shows the Kolmogorov scaling, the dashed line—thermodynamic, and the dotted line is $f = -g$.

There are two separatrices in the case $2/3 < z < 5/2$: the stable manifold of $P1$ asymptoting to the Kolmogorov line at infinity, S_1, and the unstable manifold of $P1$ asymptoting to the thermodynamic line, U_1. There are three separatrices in each of the $z < 2/3$ and $z > 5/2$ cases. One of them is a heteroclinic orbit connecting $P1$ and $P2$. For $z < 2/3$, the other two separatrices are represented by the unstable manifold of $P2$ asymptoting to the Kolmogorov line, U_2, and the unstable manifold of $P1$ asymptoting to the thermodynamic line, U_1. For $z > 5/2$, the other two separatrices are represented by the stable manifold of $P2$ asymptoting to the thermodynamic line, S_2, and the stable manifold of $P1$ asymptoting to the Kolmogorov line, S_1.

Let us analyse solutions corresponding to the separatrices.

Case $z < 2/3$.

We start with the case $z < 2/3$. Orbit U_2 corresponds to a direct energy cascade from low to high k: it starts with the dissipative scaling near $P2$,

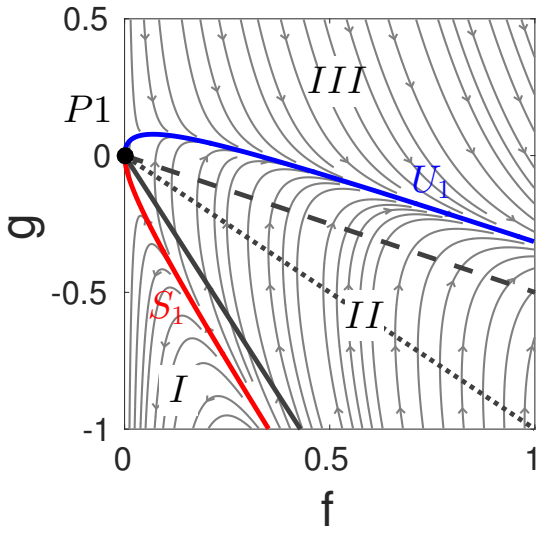

FIGURE 5.2: Case $2/3 < z < 5/2$. Phase portrait for $z = 2, \nu = 1/4$. The solid straight line shows the Kolmogorov scaling, the dashed line—thermodynamic, and the dotted line is $f = -g$.

$E \sim k^{2z-3}$, where the energy flux is gradually weakening, followed by transition to the Kolmogorov scaling, $E \sim k^{-5/3}$, at high k where the energy flux saturates to a constant k-independent value; see Figure 5.4, left. The $-5/3$ scaling will continue to infinite k corresponding to the fact that the dissipation is negligible in this range. A solution of this kind was first found in [67]. Note that orbit U_2 corresponds to an energy source at the low k boundary strong enough for f to be greater than $8\nu/D$ (i.e. to the right of $P2$). We will refer to this solution as high-Reynolds-number direct cascade.

Remark III.1. *At large k (corresponding to large f in this case) the dissipation is negligible and the solution tends to one of the inviscid solutions (5.4). Importantly, the solution in this case is pure Kolmogorov, $Q = 0$. Indeed, any finite Q would lead to deviation from the Kolmogorov line at $k \to \infty$, which is not the case here.*

Orbit H (a heteroclinic orbit connecting $P1$ and $P2$) corresponds to forcing with $f < 8\nu/D$—we will call it the low-Reynolds-number direct cascade; see Figure 5.4, left. This solution also starts with the dissipative

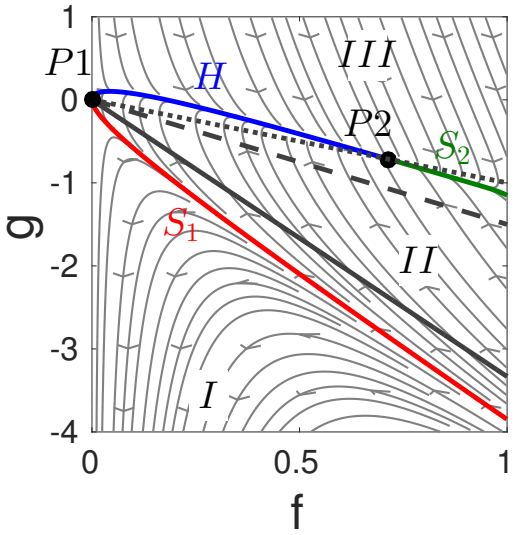

FIGURE 5.3: Case $z > 5/2$. Phase portrait for $z = 3, \nu = 5/8$ The solid straight line shows the Kolmogorov scaling, the dashed line—thermodynamic, and the dotted line is $f = -g$.

scaling near $P2$, $E \sim k^{3-2z}$, where the energy flux is gradually weakening. However, this scaling does not transition to the inviscid $-5/3$ scaling (as in of the high-Reynolds-number case) but drops to zero, together with the energy flux, at a finite wave number k_*. This corresponds to arrival of H at fixed point $P1$ and described by solution (5.24) in the vicinity of k_*.

Remark III.2. *Importantly, viscous scaling will show up on the spectra for the direct or inverse energy cascade only for very special initial data corresponding to $f_0 = f|_{s=0}$ close to $8\nu/D$, i.e. such that $E(k_0)$ is close to $k_0^{2z-3}(8\nu/D)^2$. For a generic case this condition is not satisfied, i.e. the starting point on orbits U_2 or H is far from $P2$ and there is no viscous scaling range on the spectrum.*

Finally, orbit U_1 corresponds to an inverse energy cascade; see Figure 5.4, right. Here, the energy forcing is at high (or infinite) wave number k_0 and the energy flux $\epsilon(k)$ is negative at $k < k_0$, gradually decreasing in magnitude toward lower k's and turning into zero, together with the spectrum itself, at a finite k_*. At high k, the dissipation is negligible and the spectrum tends to the warm-cascade solution (5.4), dominated by the thermodynamic part,

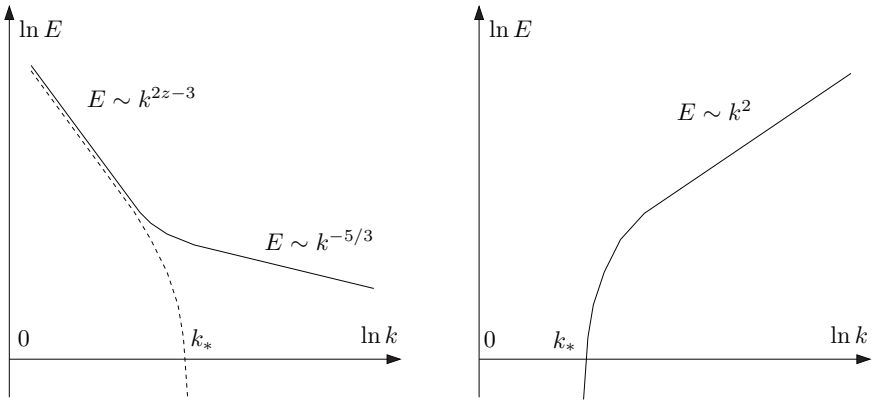

FIGURE 5.4: Sketches of spectra in case $z < 2/3$. Left panel corresponds to the direct cascade: solid line is the high-Reynolds-number spectrum described by orbit U_2; dashed line is the low-Reynolds-number spectrum described by orbit H. Right panel corresponds to the inverse cascade described by orbit U_1 (similar spectrum is associated to orbit U_1 for $2/3 < z < 5/2$).

but with a finite flux correction which is negative and almost k-independent in the high-k range, $\epsilon(k) \to P = \text{const} < 0$. On the dimensional grounds we can estimate:

$$P \sim Q^{\frac{2-3z}{5-2z}} \nu^{\frac{11}{5-2z}}. \tag{5.27}$$

Case $2/3 < z < 5/2$.

This case is the simplest because there is no $P2$ equilibrium. Orbit S_1 corresponds to a direct energy cascade. It starts with the Kolmogorov scaling at low k's (there viscosity is negligible) and terminates, with zero flux, at a finite right boundary $k = k_*$ (corresponding to the arrival at $P1$); see Figure 5.5, left. In the low-k range the Kolmogorov scaling has a finite thermal correction with $Q < 0$.

Orbit U_1 corresponds to an inverse-cascade spectrum which terminates, with zero flux, at a finite left boundary $k = k_*$; see Figure 5.4, right. At large k the spectrum asymptotes to a warm-cascade spectrum dominated

by the thermodynamic part, but with a finite flux P. The value of P can be estimated as before by equation (5.27).

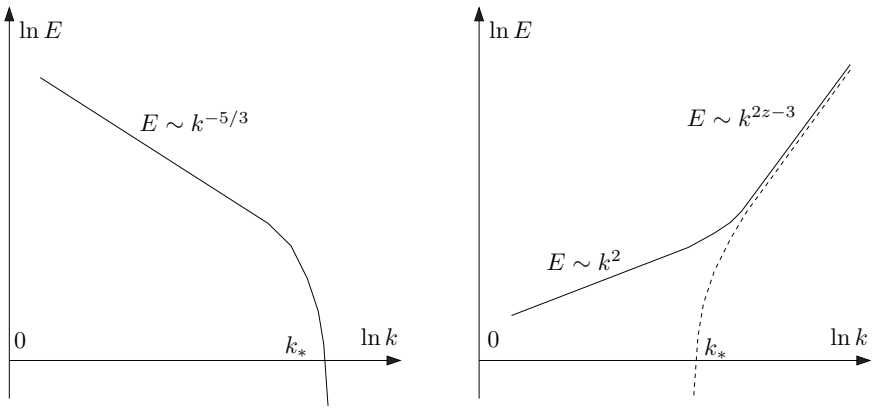

FIGURE 5.5: Sketches of spectra in case $z > 5/2$. Left panel corresponds to the direct cascade described by orbit S_1 (similar spectrum is associated to orbit S_1 for $2/3 < z < 5/2$). Left panel corresponds to the inverse cascade: solid line is the high-Reynolds-number spectrum described by orbit S_2; dashed line is the low-Reynolds-number spectrum described by orbit H.

Case $z > 5/2$.

For $z > 5/2$, the orbit S_1 behaves qualitatively similar to the behaviour of S_1 in the case $2/3 < z < 5/2$; see Figure 5.5, left. Orbits S_2 and H describe a high-Reynolds and a low-Reynolds number inverse cascades respectively; see Figure 5.5, right. The energy source is located at the right boundary of the k-range, k_0, near which it has the dissipative scaling $E \sim k^{2z-3}$ if (and only if) $E(k_0)$ is close to $k_0^{2z-3}(8\nu/D)^2$ (c.f. case $z < 2/3$). At small k the dissipation is negligible and the solution is close to pure thermodynamic. We have $P = 0$ because otherwise the flux part would win at $k \to 0$ in the warm-cascade solution (5.4), which is not the case here. The low-Reynolds number inverse cascade does not transition to the thermodynamic scaling: it terminates, with zero spectrum and flux, at a finite left boundary $k = k_*$.

III.ii Orbits other than separatrices

The other orbits are less interesting because they correspond to more artificial boundary conditions with extra sources and sinks, but we will consider them too for completeness. Orbits from part I of the phase space (below the lower separatrix/separatrices) correspond to warm direct-cascade spectra that turn into zero at finite right boundary $k = k_*$ with a finite positive value of the energy flux, which implies presence of a *point sink* at k_*; see Figure 5.6, top left. Orbits from part III (above the upper separatrix/separatrices) correspond to warm inverse-cascade spectra that turn into zero at finite left boundary $k = k_*$ with a finite negative value of the energy flux, which, again, implies presence of a *point sink* at k_*; see Figure 5.6, top right. Orbits from part II (in between of the lower and the upper separatrices) which have their two ends on the opposite sides of the thermodynamic line correspond to spectra with *two point sources* located at both ends of the k-range (energy fluxes converging toward the centre of this range are dissipated by the viscosity); see Figure 5.6, bottom. If both ends of the type II orbit are below (above) the thermodynamic line then the we get a warm direct (inverse) cascade spectrum with a *point sink* and the right (left) end of the k-range. Obviously, if one of the orbit's ends is exactly on the thermodynamic line, there are no point sinks. This special case is relevant to some numerical simulations, as will be discussed in the Conclusions section.

IV Conclusions

In this paper we have presented an exhaustive study and full classification of all possible stationary solutions of the Leith model of turbulence with dissipation represented by equation (5.1) by the phase plane analysis of the corresponding dynamical system. Different solutions are realised depending on the degree of the dissipation z, the effective Reynolds number $f_D/8\nu$, position of the forcing (at the left and right boundaries for the direct and inverse cascades respectively), absence or presence of extra dissipation or/and forcing at the boundaries (dual cascades diverging to the centre of

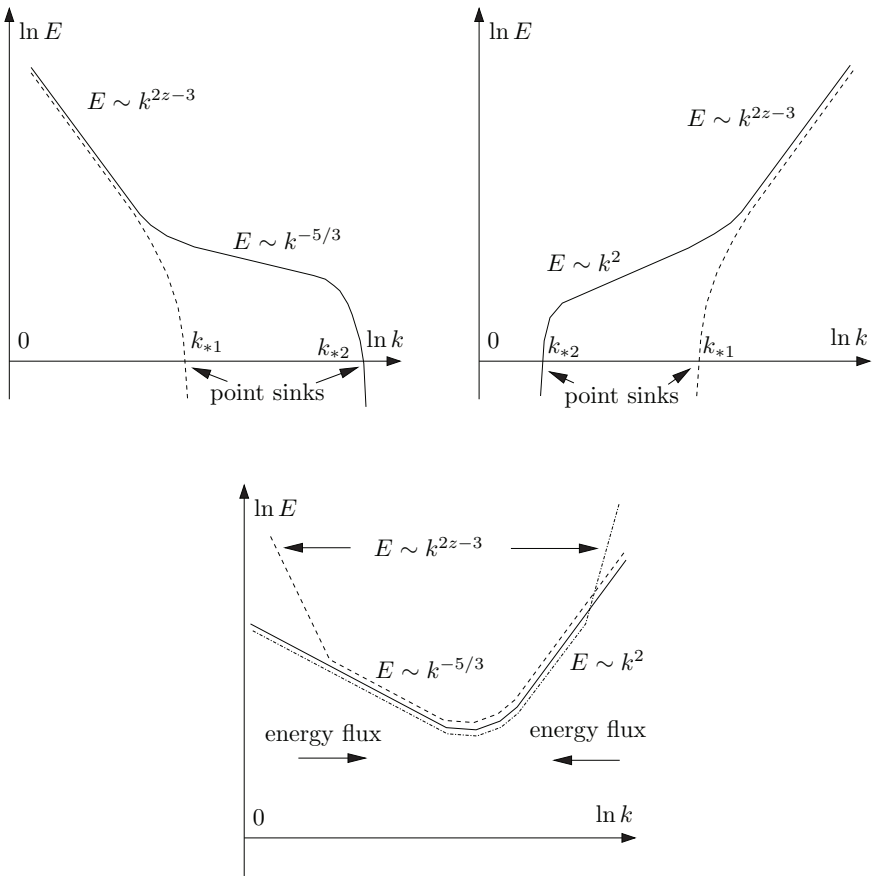

FIGURE 5.6: Sketches of spectra corresponding to orbits which are not separatrices. Top left panel corresponds to high-Reynolds (solid line) and Low-Reynolds number direct cascades (dashed line) described by the part I orbits in case $z < 2/3$. Spectra for $z > 2/3$ are similar except $E \sim k^{2z-3}$ part is absent. Top right panel corresponds to high-Reynolds (solid line) and Low-Reynolds number inverse cascades (dashed line) described by the part III orbits in case $z > 5/2$. Spectra for $z < 5/2$ are similar except $E \sim k^{2z-3}$ part is absent. Bottom panel corresponds to dual (converging) cascade spectra described by the part II orbits in cases $2/3 < z < 5/2$ (solid line), $z < 2/3$ (dashed line) and $z > 5/2$ (dash-dotted line).

the k-range, point sinks instantly absorbing the remaining flux). Such solutions may or may not have a finite front, they may asymptotically tend to inviscid "warm cascade" solutions at $k \to \infty$ with a finite constant flux P and/or temperature Q, they may exhibit viscous scaling at high or low ends of the k-range. Many possible physical situations were linked to three types of the boundary value problems—Problem 1, 2 and 3. In spite of the behavioural richness, the solutions may be divided into three distinct classes corresponding to the orbits the phase plane divided by separatrices which connect fixed points of the corresponding dynamical system with each other or with infinity.

The most physically relevant solutions are represented by the separatrices themselves. Let us mention another interesting solution corresponding to a warm direct cascade with $Q > 0$ such that the energy flux ϵ is zero at the right boundary. This is a typical solution in numerical simulations of turbulence by pseudo-spectral methods, implying there is a maximal wave number at which the energy flux is reflected. In our classification such solutions are to be found by solving Problem 3: e.g. one of such solutions could be obtained by first picking an arbitrary orbit from Part II of the phase plane, then picking its left end arbitrarily, and then placing its right end onto the thermodynamic line (see the discussion in section III).

In section III we gave a qualitative description of the solutions, including the phase portraits and sketches of typical spectra. In section B we presented rigorous proofs of the statements made in section III. The table below provides a brief summary of our solutions with emphasis on their physical meanings.

In future, it remains to be shown that the steady state solutions found in the present paper are attractors of the evolving system. It is also interesting to study scenarios of reaching the steady states. Based on a numerical evidence, the authors of papers [81, 28] suggested that the steady state in the direct cascade forms as a reflection wave propagating from high to low k's in which the Kolmogorov scaling is gradually replacing an initially steeper transient power law. This seems to be the typical behaviour for finite capacity turbulent systems [110], and it is also observed in integral/kinetic equation closures [40]. However, such a scenario has not been explained

analytically yet, and this would be an important subject for future work.

Orbits	Physics	Problems
$U_1, z < \frac{5}{2}$	Warm inverse cascade, zero flux at a sharp left end.	2
$S_1, z > \frac{2}{3}$	Negative-Q direct cascade, zero flux at a sharp right end.	1
$U_2, z < \frac{2}{3}$	High-Re cold direct cascade; (possibly) the dissipative scaling near the left end and Kolmogorov near the right end.	3
$S_2, z > \frac{5}{2}$	High-Re inverse cascade; (possibly) the dissipative scaling near the right end and thermodynamic near the left end with $\epsilon \to 0$ at $k \to 0$.	3
$H, z < \frac{2}{3}$	Low-Re direct cascade, zero flux at a sharp right end. No scaling ranges.	1
$H, z > \frac{5}{2}$	Low-Re inverse cascade, zero flux at a sharp left end. No scaling ranges.	2
O_I, any z	Direct cascade, point sink at a sharp right end.	1
O_{III}, any z	Inverse cascade, point sink at a sharp left end.	2
O_{II}, any z	Direct cascade, finite spectrum and point sink at right end, *or* inverse cascade, finite spectrum and point sink at left end, *or* converging direct and inverse cascades, point sources at both ends, *or* inverse cascade, finite spectrum and zero flux at the left end, *or* direct cascade, finite spectrum and zero flux at the right end.	3

Chapter 6

Conclusions, Discussions and Future work

We have shown that the introduction of an external potential can model experimental apparatus and can be used to study turbulence. The interactions of vortices with external potentials such as stationary vortex-like defects in Chapter 2, active defects such as particles Chapter 5 and barriers in Chapter 3 create interesting nonlinear dynamics.

One key element discussed is the emission of sound in vortex-potential interactions. This is a mechanism for energy to cascade to smaller scales. Further, we saw that impurities, barriers and particles all facilitated vortex annihilations. We saw that vortex annihilations were accompanied by a rarefaction pulse which then, via interacting further with potentials or a field of compressible sound waves, breaks into small scales. We see then that the effect is magnified as the intensity of the sound field causes a faster vortex decay rate.

In Chapter 2, we showed that vortices can be annihilated by a small vortex sized potential. The potential also trapped and scattered the vortices. We compared directly to the case of scattering from a vortex. We saw that the potential could play the role of a catalyst for vortex annihilations. As experimental apparatus is likely to have defects, this could change the decay rates and spectra considerably.

By Creating an unstable large scale structure (a step in the wave function) we were able to create turbulence in Chapter 3. This Large scale structure decayed into smaller structures, either via a train of solitons or

large scale sloshing both of which nucleated vortices. In this chapter, we saw that the inclusion of a barrier could affect the time it takes for the energy to pass through the scales. Non-trivial parameters exist for the barrier to prolong vortex turbulence. In some cases, we had a finite capacity dissipation for some range of wavenumbers in the form of a real-space heat sink, i.e. an extra well. The vortices decayed faster in the simulations in which the acoustic component was more occupied. Finally, we saw that the vortex barrier interaction is highly non-trivial and again can cause annihilations. The barrier in 3 is essentially the potential in 2 extended along a line. Here we saw the same effect of scattering; however, in this case, only when there was an angle of incidence (as changing the impact parameter would not break a symmetry).

In Chapter 4 we make the potential active and we model particle motion immersed in a superfluid. Again this can be compared to Chapter 2 as essentially we are allowing the particle to be moved by the flow of the superfluid. We test outside of its formal limits, a simplistic model for the dynamics of a particle with a vortex trapped on its core. This follows from the observation that vortices trap particles by natural dynamics in Chapter 2. The model explains excellently the dynamics of the vortices loaded with a particle. We propose future work in using an extended model, which can account for un-trapping events and annihilations for a large number of both free and trapped particles and vortices. Another key observation was that the inclusion of particles could increase annihilations due to the large amplitude oscillations of massive particles.

The analytical and semi-analytical models in Chapter 4 have a clear advantage in that they can be applied for set-ups with the particles much larger than the healing length. Such models will be useful, in investigations of superfluid with tracers where often particles are much larger than vortices. We propose that the studies in Chapter 4 show the validity of such a model in quantum fluids and that the Magnus force model works very well even for situations well beyond the formal limits of applicability of the ideal flow descriptions.

We saw via the Madelung transformation that GP dynamics are different from in classical fluids due to the quantum pressure. However, another

difference is the lack of viscosity in superfluids. The analysis of the effect of viscosity on stationary energy spectra of an approximation of NS shows that the viscosity can significantly affect the possible solutions. We also highlight how natural numerical cut-offs (dissipation in finite-difference and reflection in pseudo-spectral schemes) can affect the observed spectra.

Appendix A

Additional Calculations

I Madelung transform

In this section we show how the GP equation can be expressed in classical fluid variable, namely, ρ the fluid density and $\mathbf{u}$ the fluid velocity. We start with the defocussing NLS,

$$i\frac{\partial\psi}{\partial t} + \nabla^2\psi - |\psi|^2\psi = 0, \tag{A.1}$$

with no external potential. We then consider $-i\psi^*\times$ (A.1) + c.c.:

$$\begin{aligned} 0 &= -i\psi^*\left(i\psi_t + \nabla^2\psi - \psi|\psi|^2\right) + c.c \\ &= \partial_t\left(\psi\psi^*\right) - i\left(\psi^*\nabla^2\psi - \psi\nabla^2\psi^*\right) \\ &= \partial_t\left(\psi\psi^*\right) - i\nabla\cdot\left(\psi^*\nabla\psi - \psi\nabla\psi^*\right) \end{aligned} \tag{A.2}$$

Now we substitute in for ψ the new variables via the Madelung transformation:

$$\psi = \sqrt{\rho}\, e^{i\phi}, \tag{A.3}$$

such that $|\psi|^2 = \psi\psi^* = \rho$ and

$$(\psi^*\nabla\psi - \psi\nabla\psi^*) = \sqrt{\rho}e^{-i\phi}\left(\nabla\sqrt{\rho} + i\sqrt{\rho}\nabla\phi\right)e^{i\phi} \tag{A.4}$$
$$- \sqrt{\rho}e^{i\phi}\left(\nabla\sqrt{\rho} - i\sqrt{\rho}\nabla\phi\right)e^{-i\phi} \tag{A.5}$$
$$= i2\rho\nabla\phi = i\rho\mathbf{u} \tag{A.6}$$

where we have set $\mathbf{u} = 2\nabla\phi$. Substituting (A.3) and (A.6) into (A.2):

$$\partial_t(\rho) + \nabla\cdot(\rho\mathbf{u}) = 0 \tag{A.7}$$

we arrive at the continuity equation i.e. the evolution equation for ρ.

To find the evolution equation for $\mathbf{u}$ consider $-$(A.1)$/\psi+$c.c.:

$$0 = -i\frac{\psi_t}{\psi} - \frac{\nabla^2\psi}{\psi} + |\psi|^2 + c.c. \tag{A.8}$$
$$= -i\partial_t(\ln(\psi)) - \frac{\nabla^2\psi}{\psi} + |\psi|^2 + c.c. \tag{A.9}$$
$$= -i\partial_t(\ln(\psi) - \ln(\psi^*)) - \frac{\nabla^2\psi}{\psi} - \frac{\nabla^2\psi^*}{\psi^*} + 2|\psi|^2 \tag{A.10}$$
$$= -i\partial_t\left(\ln\left(\frac{\psi}{\psi^*}\right)\right) - \frac{\nabla^2\psi}{\psi} - \frac{\nabla^2\psi^*}{\psi^*} + 2|\psi|^2 \tag{A.11}$$

From (A.3) we can see that:

$$\ln\left(\frac{\psi}{\psi^*}\right) = 2i\phi. \tag{A.12}$$

$$\nabla^2\psi = \nabla\cdot\left(\nabla\sqrt{\rho}e^{i\phi} + i\sqrt{\rho}\nabla\phi e^{i\phi}\right) \tag{A.13}$$
$$= \nabla^2\left(\sqrt{\rho}\right)e^{i\phi} + 2\nabla\sqrt{\rho}\cdot\nabla\left(i\phi\right)e^{i\phi} + i\sqrt{\rho}\nabla^2\phi e^{i\phi} + \sqrt{\rho}\left(i\nabla\phi\right)^2 e^{i\phi} \tag{A.14}$$

$$\frac{\nabla^2\psi}{\psi} = \frac{\nabla^2\sqrt{\rho}}{\rho} + 2\frac{\nabla\sqrt{\rho}\cdot\nabla\left(i\phi\right)}{\sqrt{\rho}} + i\nabla^2\phi - \left(\nabla\phi\right)^2 \tag{A.15}$$

$$\frac{\nabla^2\psi}{\psi} + \frac{\nabla^2\psi^*}{\psi^*} = 2\frac{\nabla^2\sqrt{\rho}}{\rho} - 2\left(\nabla\phi\right)^2 \tag{A.16}$$

Bringing (A.11), (A.12) and (A.16) together we arrive at:

$$2\partial_t\phi + \frac{u^2}{2} + 2\rho - 2\frac{\nabla^2\sqrt{\rho}}{\sqrt{\rho}} = 0 \tag{A.17}$$

Now we calculate the divergence of (A.17) and apply, once again, $\mathbf{u} = 2\nabla\phi$ and arrive at the evolution equation for $\mathbf{u}$:

$$\partial\mathbf{u} + \left(\mathbf{u}\cdot\nabla\right)\mathbf{u} + \underbrace{2\nabla\rho}_{A} - \underbrace{2\nabla\left(\frac{\nabla^2\sqrt{\rho}}{\sqrt{\rho}}\right)}_{B} = 0. \tag{A.18}$$

The term which makes the evolution equation (A.18) different from the euler equations is labelled B, this term corresponds to the “quantum pressure". If B was not present the adiabatic index is found by considering the term labelled A. In the usual Euler equations the “classical pressure" appears as P/ρ, since A is the corresponding term here the adiabatic pressure must be ρ^2 thus the index is 2. If the non-linear term is discarded the term A would disappear.

II Conservation calculations

To show that mass is conserved we shall take the derivative and show that it is zero:

$$\dot{M} = \int_V \frac{\partial|\psi|^2}{\partial t} d\mathbf{x} = \int_V \psi \frac{\partial \psi^*}{\partial t} + \psi^* \frac{\partial \psi}{\partial t} d\mathbf{x} \tag{A.19}$$

$$= i \int_V \nabla \cdot (\psi^* \nabla \psi - \psi \nabla \psi^*)\, d\mathbf{x} \tag{A.20}$$

$$= i \int_{\partial V} (\psi^* \nabla \psi - \psi \nabla \psi^*) \cdot \mathbf{n} dS \tag{A.21}$$

$$= 0. \tag{A.22}$$

The second step was Gauss' theorem and the final step is due to the boundary conditions stated either being periodic or the wavefunction going to zero.

We can apply the same method to show energy conservation in a domain with periodic or zero boundary conditions:

$$\dot{H} = \partial_t \int_V \left[|\nabla \psi|^2 + \frac{1}{2}|\psi|^4 \right] d\mathbf{x} \tag{A.23}$$

$$= \int_V \left[(\nabla \psi) \cdot \nabla \partial_t \psi^* + (\partial_t \psi^*)\, \psi |\psi|^2 \right] d\mathbf{x} + c.c. \tag{A.24}$$

$$= \left[\nabla \psi \partial_t \psi^* \right]_{\partial V} + \int_V \left[-\nabla^2 \psi \partial_t \psi^* + (\partial_t \psi^*)\, \psi |\psi|^2 \right] d\mathbf{x} + c.c. \tag{A.25}$$

$$= \int_V (\partial_t \psi^*) \left[-\nabla^2 \psi + \psi |\psi|^2 \right] d\mathbf{x} + c.c. \tag{A.26}$$

$$= \int_V (\partial_t \psi^*) \left[i \partial_t \psi \right] d\mathbf{x} + c.c. \tag{A.27}$$

$$= \int_V i|\partial_t \psi|^2 - i|\partial_t \psi|^2 d\mathbf{x} = 0. \tag{A.28}$$

The first operation was integration by parts and the boundary terms vanish due to the zero or periodic boundary conditions. The fourth operation was substituting in the rhs of the GP equation in place of the time derivative.

III Vortex tracking methods

We define the pseudo-vorticity:

$$\mathbf{j} = \rho\mathbf{v} = \frac{1}{2i}(\psi^*\nabla\psi - \psi\nabla\psi^*) \tag{A.29}$$

$$\omega_{\rho s} = \frac{1}{2}\nabla \times \mathbf{j} \tag{A.30}$$

This is ideal as the pseudo-vorticity is regular at the vortex core, whereas the vorticity is not. To track the vortices we implement a simple algorithm:

Algorithm 1 Vortex tracking

Require: ψ - wavefunction, θ_ω - pseudo-vorticity threshold, C - core size and θ_ρ - density threshold

Calculate pseudo-vorticity: $\omega_{\rho s}(\psi)$
Compute maximum $M_\omega^>$ and its position
$i = 0$
while $M_\omega > \theta_\omega$ **do**
    if $|\psi(P_\omega)|^2 < \theta_\rho$ **then**
        $i = i + 1$
        $V_p^+(i) = P_\omega$
    end if
    $\omega_{\rho s}(\omega_{\rho s}(\psi(P_\omega + C)) > \theta) = 0$
    Compute maximum $M_\omega^>$ and its position P_ω
end while
Compute minimum $M_\omega^<$ and its position P_ω
$i = 0$
while $M_\omega^< < -\theta_\omega$ **do**
    if $|\psi(P_\omega)|^2 < \theta_\rho$ **then**
        $i = i + 1$
        $V_p^-(i) = P_\omega$
    end if
    $\omega_{\rho s}(\omega_{\rho s}(\psi(P_\omega + C)) < -\theta) = 0$
    Compute minimum $M_\omega^<$ and its position
end while
return V_p^-,V_p^+

IV Added mass

A common technique used to calculate the added forces on an object moving or accelerating through a fluid is often referred to as the "Added mass". The idea is to think of the additional forces solely as an additional mass of an object moving in a vacuum. To derive the hydrodynamic mass we consider the forces acting on an object as it accelerates through a fluid. Consider a sphere with surface element δ_S in $3D$ accelerating in any direction with acceleration $\dot{U}$. We denote the radius R of the sphere. Then the force acting on this body will be

$$\mathbf{F} = \int p \; dS, \tag{A.31}$$

with p denoting the pressure of the fluid given by the unsteady (due to the motion of the obstacle) Bernoulli equation:

$$p = -\rho \left(\frac{\partial \phi}{\partial t} + \frac{1}{2} |\nabla \phi|^2 \right) \tag{A.32}$$

The velocity potential for axisymmetric flow around a sphere can be found by solving the Laplace equation with suitable boundary conditions and is given by $\phi = Ucos(\theta)\frac{R^3}{2r^2}$ [13]. In spherical coordinates (r, θ, ϕ), we choose the axis such that F is in the same direction as the acceleration:

$$F = \int -\rho \left(\frac{\partial \phi}{\partial t} + \frac{1}{2} |\nabla \phi|^2 \right) dS \tag{A.33}$$

$$= \int -\rho \left(\frac{\partial \phi}{\partial t}|_{r=R} + \frac{1}{2} |\nabla \phi|^2|_{r=R} \right) 2\pi R^2 \cos(\theta) \sin(\theta) d\theta \tag{A.34}$$

$$= -\frac{2}{3} \rho \pi R^3 \dot{U} \tag{A.35}$$

and in 2D where the velocity potential is $\phi = Ucos(\theta)\frac{R^3}{r}$ [13]:

$$F = \int -\rho\left(\frac{\partial\phi}{\partial t} + \frac{1}{2}|\nabla\phi|^2\right) dS \tag{A.36}$$

$$= \int -\rho\left(\frac{\partial\phi}{\partial t}|_{r=R} + \frac{1}{2}|\nabla\phi|^2|_{r=R}\right) \cos(\theta)d\theta \tag{A.37}$$

$$= -\rho\pi R^2\dot{U} \tag{A.38}$$

In the 2D case the added mass is then $m_a = \rho\pi R^2$.

Appendix B

Rigorous analysis of solutions to Leith model

.i Boundary value problems

For equation (5.2) we are interested in studying the following boundary value problems. Find solutions of equation (5.2) supplemented by the conditions

$$E(k_0) = E_0, \quad E(k_*) = 0, \quad k_* > k_0 \tag{B.1}$$

such that $E(k) > 0$ for $k \in [k_0, k_*)$ (which corresponds to $s = \ln k/k_0 < 0$) and

$$E(k_0) = E_0, \quad E(k_*) = 0, \quad 0 < k_* < k_0 \tag{B.2}$$

for $k \in [k_*, k_0)$ which corresponds to $s < 0$. We will refer to these as Problem 1 and Problem 2 respectively. In an addition, we also consider Problem 3:

$$E(k_0) = E_0, \quad E(k_1) = E_1. \tag{B.3}$$

We show that not for all combinations E_0, E_1, k_* and k_1 Problems 1-3 are solvable.

It will be convenient to write equation (5.6) in an equivalent form:

$$\hat{F}(f) \equiv 2\frac{d}{ds}\left(f^2\frac{df}{ds}\right) + (12z - 19)\, f^2\frac{df}{ds} + Df^3 - 8\nu f^2 = 0. \tag{B.4}$$

Notice that equation (B.4) admits the translation group of transformations

of independent variable $s \to s + b$ where b is a constant with the infinitesimal operator $X = \frac{\partial}{\partial s}$. For the original equation (5.2) this symmetry is transformed into the scaling symmetry. Therefore we set $k_0 = 1$ for the first boundary condition in (B.1). In terms of $f(s)$ the boundary value problems are formulated as solving equation (B.4) with the following boundary conditions. Problem 1f:

$$f(0) = f_0 > 0, \quad f(s_*) = 0, \quad s_* > 0, \tag{B.5}$$

Problem 2f:

$$f(0) = f_0 > 0, \quad f(s_*) = 0, \quad s_* < 0, \tag{B.6}$$

and Problem 3f:

$$f(0) = f_0 > 0, \quad f(s_1) = f_1 > 0. \tag{B.7}$$

To study these boundary value problems, we apply the well-developed methods of the theory of nonlinear ODEs, see e.g. [92]. First of all, we notice that solutions of these problems are (if exist) unique. Also, it is easy to establish that the Kolmogorov solution denoted by $f_{P,0}$ is a super solution of equation (B.4), i.e. $\hat{F}(f_{P,0}) \leq 0$. The same is true for the thermodynamic spectrum $f_{0,Q}$ and for the general solution of the inviscid form of equation (B.4),

$$f_{P,Q}(s) = c^{1/2} e^{(5-2z)s/2} \left(Pe^{-11s/2} + Q\right)^{1/3}. \tag{B.8}$$

.ii Case $z < 2/3$

Let us consider the case $z < 2/3$ which means that $D > 0$ and $12z - 19 < 0$. We will consider equation (B.4) and the phase portrait of the dynamical system (5.10), (5.11) to establish which data guarantees solvability of the Problems 1 and 2. Instead of directly using the boundary conditions (B.5) and (B.6) let us employ a shooting method. Namely, let us supplement equation (B.4) by the initial conditions

$$f(0) = f_0 > 0, \qquad \frac{d}{ds} f \Big|_{s=0} = 0. \tag{B.9}$$

These initial conditions mean that we study the orbits of the dynamical system which start on the line $f+g=0$ of the phase plane (f,g). Note that the direction of velocity $(df/d\tau, dg/d\tau)$ on the line $f+g=0$ is vertically down for $f > f_D$ and vertically up for $f < f_D$, where $f_D = 8\nu/D$. Recall that equation (B.4) has an exact positive solution $f(s) \equiv f_D$ which corresponds to the unstable node $P2$ on the phase plane.

We begin with a preliminarily analysis of the behavior of orbits of the dynamical system (5.10), (5.11).

Lemma .1. *The orbits of the dynamical system (5.10), (5.11) intersecting the line $f+g=0$ with $f \geq 48\nu/5D$ do not approach the fixed point $P1$. Instead, these orbits approach, in finite time, the g-axis without intersecting it, so that $f \to 0, g \to -\infty$ as $s \to s_* > 0$.*

To prove this Lemma, we consider an integral identity obtained by multiplying equation (B.4) by $f^2 df/ds$, integrating over $[0,s]$ and setting $df/ds = 0$ at $s=0$:

$$2\left(f^2\frac{df}{ds}\right)^2(s) + (12z-19)\int_0^s f^4\left(\frac{df}{d\eta}\right)^2 d\eta + \Phi(f) = \Phi(f_0). \qquad \text{(B.10)}$$

where $\Phi(f) = \frac{D}{6}f^6 - \frac{8\nu}{5}f^5$. Function $\Phi(f)$ has zeros at $f=0$ and $f=\frac{48\nu}{5D}$; $\Phi(f) < 0$ for $f \in (0, \frac{48\nu}{5D})$, and $\Phi(f) > 0$ for $f > \frac{48\nu}{5D}$. The minimum of $\Phi(f)$ is achieved at $f = \frac{8\nu}{D}$. First, let us show that at least for $f_0 \geq 48\nu/5D$ the corresponding solutions are decreasing functions up to the intersection with the s-axis. Indeed, since $f_0 \geq 48\nu/5D > 8\nu/D$ the solutions are decreasing functions for small s because $f(s)$ has a local maximum at $s=0$: $f'(0)=0, f''(0) = g'(0) < 0$. Now suppose that $f(s)$ also has a positive minimum at $s>0$ (including the case $f(s) \to \text{const} > 0$ as $s \to \infty$): then the first term in (B.10) is zero, the second term is negative and, therefore, $\Phi(f(s)) > \Phi(f_0)$. But this means that $f(s) > f_0$ which contradicts the assumption that this is a minimum, i.e. has to be less than the maximum. Therefore, there can be no positive minima, as required.

Now let us show that f can vanish at finite point $s = s_*$ only. Assume that $s_* = \infty$: then $df/ds \to 0$ as $s \to \infty$ and the first term of the left-hand side of (B.10) tends to zero. So do the third and the fourth terms

on the left-hand side, whereas the second term is bounded from above by a negative number (in principle it could be $-\infty$ if the integral was divergent). But then we arrive at a contradiction as the right-hand side in (B.10) is positive. Therefore $s_* < \infty$.

By the same argument we see that at the point $s_* < \infty$ where $f(s_*) = 0$ we must have $\lim_{s\to s_*}(f^2 df/ds) = \text{const} \neq 0$ and, therefore, $\lim_{s\to s_*} df(s)/ds = -\infty$. In view of the formula $df/ds = f + g$ we get that $g(s) \to -\infty$ as $s \to s_*$ ($\tau \to \tau^*$). Therefore the corresponding orbits of the dynamical system (5.10), (5.11) cannot approach the equilibrium $P1$ (where $df(s)/ds = 0$), but instead asymptote to the g axis with $g \to -\infty$.

Corollary .1. *At least for $f_0 \geq 48\nu/5D$ there exits $s_* < \infty$ such that the boundary value problem (B.4), (B.5) is solvable. Flux ϵ defined by (5.3) and (5.7) tends to a positive constant as $s \to s_*$.*

Corollary .2. *The boundary value problem (B.4), (B.5) with $s_* = \infty$ has no solutions at least for $f_0 \geq 48\nu/5D$.*

Remark .1. *We show later that the orbits for all $f_0 > f_D$ asymptote to the g-axis, $(f, g) \to (0, -\infty)$.*

On the orbits asymptoting to the g-axis the flux ϵ defined by (5.7) is positive at each s. We see that $\epsilon > 0$ for $df/ds < 0$, which includes the line $g + f = 0$ and below. For the orbits that go to $P1$ (i.e. the heteroclinic orbit H) we have $\epsilon(s_*) = 0$ since at this point $f = df(s)/ds = 0$. For $f_0 \geq 48\nu/5D$ we showed that $\lim_{s\to s_*}(f^2 df/ds) = \text{const} < 0$ (actually, the same is true for all orbits with $f_0 > 8\nu/D$). Thus for small f (and therefore large negative $df/ds \approx g$) we have from (5.7):

$$\lim_{s\to s_*} \epsilon(s) = Ae^{(3z-2)s_*}, \quad A = \text{const} > 0. \tag{B.11}$$

Therefore, $\epsilon(s_*) > 0$, as required. Moreover, $\epsilon(s_*)$ is a decreasing function of s_*.

Remark .2. *Each orbit of (5.10), (5.11) is invariant under shifts along the trajectory $\tau \to \tau + a$ or the translation symmetry (with respect to $s \to s + b$) of equation (B.4). According to formula $E(k) = k^{2z-3} f^2$,*

the translation symmetry generates a one-parametric family of solutions $E(k,b) = e^{b(z-3/2)}E(bk)$ *for each known solution* $E(k)$*. In the other words, each orbit on the* (f,g) *plane corresponds to not just one, but to a one-parametric family of solutions.*

To prove the existence of separatrices, we present a technical result concerning the direction of the vector field on the Kolmogorov line f^K : $g+(1/3+z)f=0$ and thermodynamic line f^T : $g+(z-3/2)f=0$. Notice that f^K is located above of the line $f+g=0$ and below the thermodynamic line which is located in the first quadrant of the phase plane for $z<2/3$. We write $g=g(f)$ where

$$\frac{dg}{df} = -\frac{2(f+g)}{f} - (6z-17/2) - \frac{D}{2(f+g)} + \frac{4\nu}{f+g} \equiv G(f,g).$$

Lemma .2. $G(f,-(1/3+z)f) > -(1/3+z)$ *for the Kolmogorov line and* $G(f,-(z-3/2)f) > -(z-3/2)$ *for the thermodynamic line.*

By simple calculations, we have $G(f,-(1/3+z)f) = -(1/3+z) + 4\nu/((2/3-z)f)$ for the Kolmogorov line and $G(f,-(z-3/2)f) = -(z-3/2)+4\nu/((5/2-z)f)$ for the thermodynamic line. Geometrically Lemma .2 states that along f^K and f^T the flow is directed into the domains $g+(1/3+z)f>0$ and $g+(z-3/2)f>0$ respectively.

Now we show the existence of a heteroclinic connection between the fixed points $P2$ with $P1$.

Lemma .3. *There exists an orbit* H *(a heteroclinic connection) of (5.10), (5.11) which emerges out the unstable node* $P2$ *and goes to the equilibrium* $P1$ *with time.*

Consider a Cauchy problem for equation (B.4) supplemented with the initial data

$$f(0) = f_0 \equiv f_D - \varepsilon, \qquad \frac{d}{ds}f\Big|_{s=0} = f_m < 0, \qquad m = 1,\dots \tag{B.12}$$

for arbitrary small $\varepsilon > 0$. Notice that vertical line $f = f_D - \varepsilon$ intersects the Kolmogorov line on the phase plane and also the orbits obtained in

Lemma .1. First of all, we indicate that for sufficiently small values of $|f_m|$ the orbits, which correspond to solutions of (B.4), (B.12), intersect the line $g + f = 0$ since the direction of the velocity field $(df/ds, dg/ds)$ is directed into $g + f > 0$ for $f < f_D$. Therefore, these solutions achieve local minima. At the same time, there exists f_m such that the corresponding solutions decrease monotonically with time vanishing at some finite points. Indeed, the line $f = f_D - \varepsilon$ always intersects the orbits obtained in Lemma .1 and f_m, together with f_0, fix the coordinates of these intersections. For completeness, we notice that if we take f_m positive and sufficiently large such that we are located above of the Kolmogorov line then solutions of (B.4), (B.12) are increasing functions, see Lemma .2. Therefore, there exists families of orbits with different behaviours on the phase plane and it should be a separatrix which separates them. To prove it, let us consider the set $A = \{f_m,\ f_m < 0\}$ with the properties: the corresponding solution of the Cauchy problem has a positive minimum at $s = s_{min}$. This set is not empty and not a single element set. Moreover, A is bounded below, see the discussion above. It means that inf A exists, which we denote by f_A, and the solution we denote by $f(s; f_A)$. We denote the corresponding orbit by H. According to the definition of the infimum any vicinity of f_A produces solutions both in and outside of A, i.e. $df/ds = 0$ at the boundary $s = s_*$ which, by definition, is where $f = 0$. (We discard possibility for $f(s; f_A) \to \text{const} < \infty$ with $df/ds \to 0$ at $s \to \infty$, as there are no fixed points in the system other than $P1$ and $P2$.) However, the point where $f = df/ds = 0$ is $P1$ and, therefore, orbit H goes to $P1$ and reaches it (as it follows from the asymptotics of solution near $P1$ found in section II.iv) in finite $s = s_*$.

If we now change τ to the inverse time $\hat{\tau} = -\tau$ then H goes to the stable node $P2$. It follows from the Poincaré-Bendixon theorem. Indeed, let us consider a finite area of the (f, g)-plane: the g-axis, the Kolmogorov line, a horizontal line somewhere below $P2$, $g = g_b$ const $< -f_D$ and the vertical line $f = -g_b$. Easy calculation shows that on the boundary of this domain vector field $(df/d\hat{\tau}, dg/d\hat{\tau})$ is either directed into this domain or along the boundary. Note that there is only one orbit passing through $P1$ within the specified domain–the orbit H. The other orbit passing $P1$

is describes motion toward this fixed point (in the reverse time) from outside of the specified domain. This follows from the local structure of this trajectory (and of H) $f \sim g^2$, see equations (5.26) and (5.25). Thus, H cannot return to $P1$ as this would imply leaving the specified domain first, which is impossible by the construction—i.e. H is not a homoclinic orbit. Therefore, H approaches the stable (in the reverse time) node $P2$ and this is a heteroclinic connection.

Corollary .3. *There exists a solution of Problem 1f which vanishes together with the flux ϵ defined by (5.7) at a finite point $s = s_*$. This solution is represented by the orbit H.*

Indeed, since for H we have $f = df/ds = 0$ at $s = s_*$, the right-hand side of (5.7) is zero.

Existence of the orbit H allows us to generalize Lemma .1 to all $f_0 > f_D$ as stated in Remark .1. Indeed, such orbits are bound by H on one side and by the orbits with $f \geq 48\nu/5D$ which approach the g-axis. Thus they also asymptote to the g-axis.

Now let us prove that there exists an orbit U_2 which originates at the fixed point $P2$ and asymptotes to the Kolmogorov line f^K for large τ, see Figure 5.1.

Lemma .4. *There exists an orbit U_2 which emerges out the unstable node $P2$ and transitions to the Kolmogorov line as $\tau \to \infty$*

Consider a Cauchy problem for equation (B.4) supplemented with the initial data

$$f(0) = f_0 = f_D + \varepsilon, \qquad \frac{d}{ds} f \Big|_{s=0} = f_m, \qquad m = 1, \dots . \tag{B.13}$$

Here $\varepsilon > 0$ is arbitrarily small. Note that vertical line $f = f_D + \varepsilon$ intersects the Kolmogorov line on the phase plane. Let us consider the solution $f(s; f_m)$ of (B.4), (B.13). Assume that $f(s; f_m)$ is large at sufficiently large s, namely that there exists $s_0 > 0$ such that $f(s; f_m) \gg f_D$ for $s > s_0$ so that the right-hand side of (B.4) is negligible compared to the last term on

the left-hand side, and in the leading order we have an inviscid equation:

$$2\frac{d}{ds}\left(f^2\frac{df}{ds}\right)+(12z-19)\,f^2\frac{df}{ds}+Df^3=0. \tag{B.14}$$

Solutions of this equation are

$$f_{P,Q}(s)=c^{1/2}e^{(5-2z)s/2}\left(Pe^{-11s/2}+Q\right)^{1/3}. \tag{B.15}$$

They correspond to the warm-cascade solutions (5.4). In view of the theorem of continuous dependence of solutions on the right-hand side applied to equation (B.4), we have that for $f(s_0)/f_D\to\infty$, $f(s)$ converges to $f_{P,Q}(s)$ for $s\geq s_0$ at least in the Hölder norm $C^{2+\alpha}$, $0<\alpha<1$ on each compact interval. Therefore $f(s;f_m)$ converges to $f_{P,Q}(s)$ for $s\geq s_0$.

Function $f_{P,Q}(s)$ is the two-parametric general solution of the inviscid form of the inviscid equation (B.14), where $c>0$ and P, Q are constant parameters. Parameter P is the flux ϵ which is constant on $f_{P,Q}(s)$. Case $Q=0$ gives the Kolmogorov solution $f_{P,0}$ parametrized by P, whereas for $P=0$ we get the thermodynamic solution $f_{0,Q}$ parametrized by temperature Q. For different values of the parameters P and Q we have both increasing and decreasing behavior of $f_{P,Q}(k)$. It follows from (B.15) that the Kolmogorov solution $f_{P,0}$ is positive everywhere and is a solution of the minimal growth among solutions $f_{P,Q}(s)$. If P and Q have different signs, $f_{P,Q}(s)$ vanishes at $s=(2/11)\ln(-P/Q)$. Therefore for the growing $f(s;f_m)$ the corresponding orbits either asymptote to the Kolmogorov line or pass above this line asymptoting to the thermodynamic line as $\tau\to\infty$, as the Q-term in (B.15) is always dominant for large s.

Consider the set $C=\{df(0)/ds=f_m\}$ with the properties: corresponding solutions of the Cauchy problem (B.4), (B.13) have one positive maximum at $s=s_{max}$. On the phase plane (f,g) the points of local maximum of $f(s;f_m)$ are located on line $f+g=0$ for $f>f_D$ and go along this line as f_m grows. Clearly, values of f_m such that the corresponding orbits intersect line $g+f=0$ exist: for example one can take an initial point very close and just above line $g+f=0$. Thus, set C is not empty. Also, set C is bounded from above: at the very least it is bounded by the value f_m corresponding

to the Kolmogorov line. Indeed, the orbits cross the Kolmogorov line from the lower to the upper side, and, therefore, once crossing it will never cross back, see Lemma .2. Therefore, $\sup C < \infty$ exists, let us denote it by f_C, and the solution $f(s; f_C)$ of (B.4), (B.13) is a positive increasing function defined for $s \geq 0$. Orbit U_2, corresponding to $f(s; f_C)$, asymptotes to the Kolmogorov line on the phase plane as $s \to \infty$. Indeed, $f(s; f_C)$ presents the minimally monotonically growing solution as $s \to \infty$ in the sense for $f_m = f_C - \delta$ with arbitrary small $\delta > 0$ the corresponding solution of the Cauchy problem is not a monotonically increasing function. For positive $\delta \to 0$ we have $s_{\max} \to \infty$ and $f(s_{\max}) \to \infty$ so that for $s \sim s_{\max}$ the solution converges to an inviscid solution $f_{P,Q}(s)$ with a finite positive P and negative $Q \to 0$ (see remark .3 below). For negative $\delta \to 0$ we have no maximum, but for large s the solution also converges to an inviscid solution $f_{P,Q}(s)$, now with a finite positive P and positive $Q \to 0$. Therefore, $f(s; f_C) \to f_{P,0}(s)$ for $s \to \infty$. By construction, orbit U_2 is above of the line $g + f = 0$. Also, it remains below the Kolmogorov line, because crossing this line and then asymptoting back to it would contradict the monotonous decrease of $\epsilon(s)$ property.

Let us now show that orbit U_2 emerges out of the unstable node $P2$. Consider a finite domain bounded by the Kolmogorov line, line $g + f = 0$ for $f \geq f_D$, orbit H for $f < f_D$ and a vertical line $f = f_D + \varepsilon$. For the inverse time $\hat{\tau} = -\tau$, the vector field $(df/d\hat{\tau}, dg/d\hat{\tau})$ is directed either inwards or parallel to the boundaries of this domain (e.g. for the Kolmogorov line see Lemma .2). Thus, by the Poincaré-Bendixon theorem the orbit U_2 must approach $P2$. U_2 cannot approach $P1$ since the only orbit in the fourth quadrant that goes to $P1$ is H (see section II.iv).

Remark .3. *We established that there exist a monotonically growing solution $f(s; f_C)$ and converging to $f_{P,0}(s)$ in the Hölder norm $C^{2+\alpha}$ as $s \to \infty$. Respectively, the flux $\epsilon(s; f_C)$ calculated for $f(s; f_C)$ converges to the flux $\epsilon_{P,0}(s)$ for the Kolmogorov solution $f_{P,0}$ as $s \to \infty$. Direct calculation shows that $\epsilon_{P,0}(s) \equiv P$ is a positive constant for all s. Thus $\epsilon(s; f_C) \to P$ as $s \to \infty$. Let us now take $f_m \in C$ sufficiently close to f_C: there exists an interval $[a_m, b_m]$, $a_m > 0$, $b_m < \infty$ where $f(s; f_m) \gg f_D$ or/and*

$|g(s;f_m)| \gg f_D$. *Hence the difference* $|f(s;f_m) - f_{P,Q}(s)|$ *is small in the norm of the Hölder space* $C^{2+\alpha}[a_m, b_m]$ *for some choice of the parameters* P *and* Q*, where* Q *is always a negative quantity. Therefore the flux* $\epsilon(s)$ *tends to constant* P *and* $f_{P,Q}(s)$ *is an asymptotic of* $f(s;f_m)$.

Let us denote by O_I the set of orbits which located below of $H \cup U_2 \cup P2$. By O_{II} we will denote the set of orbits which emerge out $P2$ and located above of $H \cup U_2 \cup P2$. As we will shortly show, the latter set is bounded from above on the (f,g)-plane by yet another separatrix, U_1. The set of orbits in the first quadrant of the (f,g)-plane above U_1 will be called O_{III}.

The flux ϵ is positive on the g-axis and on the line $g + f = 0$ of the fourth quadrant. All orbits from O_{II} can be obtained by starting from different initial points on the Kolmogorov line. Moving backwards in time one can see, by the Poincaré-Bendixon theorem using the domain bounded by $H \cup U_2 \cup P2$ and the Kolmogorov line, that the orbits converge onto $P2$. Moving forwards in time we get solutions $f(s)$ that grow monotonously and, therefore, at large s converge to $f_{P,Q}(s)$ with $Q > 0$. Note that, in spite of the two parameters in $f_{P,Q}(s)$, the respective family of orbits is one-parametric due to the translational symmetry mentioned in Remark .2. But the Q-part always wins in $f_{P,Q}(s)$ over the P-part at large s, so all these orbits asymptote to the thermodynamic line. This applies to the limiting orbit starting at $P1$. In fact we already know, that when run backwards in time the trajectory starting at $P1$ also ends at starting at $P2$—like any orbit from the O_{II} set: this is orbit H. Thus we have proven the following lemma concerning the orbit starting at $P1$ and running forward in time.

Lemma .5. *There exists an orbit* U_1 *of the dynamical system (5.10), (5.11) which emerges out the fixed point* $P1$ *and asymptotes to the thermodynamical line.*

Remark .4. *Orbit* U_1 *starts with zero flux at* $P1$, $\epsilon(0) = 0$, *and asymptotes to* $f_{P,Q}(s)$ *with* $Q > 0$ *and* $P < 0$. *Thus,* U_1 *lies above the thermodynamic line (on which* $\epsilon(s) = 0$*).*

Note that this remark does not contradict the preceding lemma because at large s the Q-term is dominant over the P-term in $f_{P,Q}(s)$ for any finite P and Q.

Thus, U_1 represents an inverse energy cascade solution vanishing, together with the flux, at a finite wave number. The fact that $\epsilon(0) = 0$ follows from (5.7) upon substitution $f = df/ds = 0$. The fact that $\epsilon \to P < 0$ for $s \to \infty$ follows from the fact that $\epsilon(s)$ is always a monotonically decreasing function of s.

Corollary .4. *U_1 realises a solution of Problem 2f which vanishes, together with $f^2 df/ds$ and ϵ, at $s = s^{**}$, $s^{**} < 0$.*

This statement follows from the shift invariance of the solutions. Changing $s \to s + s^{**}$, we shift the point where $s = 0$ to somewhere on U_1 away from $P1$. This will generate the required solution of Problem 2f which vanishes at $s = s^{**}$ with zero flux.

Now, let us consider set O_{III}. It is clear that the O_{III}-orbits represent monotonously increasing $f(s)$ which asymptotes to the inviscid $f_{P,Q}(s)$ solutions with $Q > 0$ and $P < 0$ for $s \to \infty$. However, O_{III} are very different from O_{II} near the left boundary of the s-interval.

Indeed, since $f(s)$ is monotonously growing, moving backwards in time the O_{III}-orbits will reach small values of f such that $f \ll f_D$ and $f \ll g$. Then the dynamical system (5.10) and (5.11) reduces to:

$$\frac{df}{d\tau} = gf, \quad \frac{dg}{d\tau} = -2g^2,$$

solving which we have

$$g = \frac{1}{2(\tau - \tau^*)}, \quad f = C(\tau - \tau^*)^{1/2}, \quad \tau > \tau^*, \tag{B.16}$$

where C is a positive constant.

Thus, the O_{III}-orbits have a sharp left boundary $s_* < 0$, i.e. correspond to solutions of Problem 2f on $s_* < s < 0$ such that $f(s) \to 0$ as $s \to s_*$. In fact, $f(s)$ vanishes at a finite point that follows from (B.16). Indeed, in terms of $f(s)$ the obtained solution reads:

$$f(s) = (4C/9)|s - s_*|^{3/4}. \tag{B.17}$$

Note that at s_* we have $f^2 df/ds = C^2/2$, which means that $\epsilon(s_*)$ is a finite negative number, see (5.7). Therefore, any O_{III}-orbit also corresponds to an inverse energy cascade situation, but now with a finite amount of (negative) flux left at the point s_* where the spectrum turns into zero. For realisability of such a solution one has to put a point sink of energy at the boundary $s = s_*$.

We will now put together the classification of the orbits.

Theorem .1. *$H \cup U_2 \cup P2$ and U_1 divide the phase plane (f, g) ($f > 0$, $-\infty < g < \infty$) into the parts I, II and III with the different behaviours of orbits. In part I orbits emerge out of $P2$ and always asymptote to the negative part of the g-axis. In part II orbits emerge out of $P2$, the fourth quadrant intersecting the f-axis (never intersecting g-axis), and asymptote to the thermodynamic line as $\tau \to \infty$. In part III orbits emerge with $(f, g) \to (0, +\infty)$, go down along the g-axis, and then turn up asymptoting to the thermodynamic line as $\tau \to \infty$.*

Now we will consider how the orbits classified in Theorem .1 could be linked to solutions of Problems 1, 2 and 3, or equivalently 1f, 2f and 3f. It is clear that there exist parameters of these problems for which solutions exist. Below we will show that not for all values of parameters there exist a solution.

Theorem .2. *There exist choices of parameters (E_0, k_*) (of (f_0, s_*)) for which Problem 1 (Problem 1f) is not solvable.*

The Problem 1 is equivalent to the Problem 1f, so we will stick here to the Problem 1f. Initial condition $f(0) = f_0$ corresponds to the points on the vertical line $f = f_0$ on the (f, g)-plane. Only orbits from the O_I family and the orbit H are relevant to the Problem 1f, as only these orbits describe solutions vanishing at a finite right boundary, $s_* > 0$. It is clear that s_* is a monotonously increasing function of g_0 for fixed f_0. Indeed, larger g_0 for fixed f_0 mean smaller negative values of $df/ds(0)$. If such solutions had smaller s_* than the values of s_* corresponding to larger negative $df/ds(0)$ then the two solutions would have to intersect at some $s > 0$, which is impossible due to uniqueness of solution of the Problem 1f (arising by choosing

the intersection point at the right boundary). Secondly, for $g_0 \to -\infty$ at fixed f_0 we have $s_* \to 0$, which follows from the inviscid asymptotics of the solution valid at large $|g|$. Consider the case $f_0 < f_D$. From what we just said it follows that s_* is bounded from above by a finite value corresponding to s_* of the solution generated by the heteroclinic orbit H; let us call it s_{*H}. Thus we have proven that for any $f_0 < f_D$ there exist $0 < s_{*H} < +\infty$ such that the Problem 1f does not have solution with pair (f_0, s_*) if $s_* > s_{*H}$ and have solution if $s_* \leq s_{*H}$. Now consider the case $f_0 \geq f_D$. In this case the value of possible s_* is not bounded: it tends to infinity when (f_0, g_0) approaches to U_2. Thus we have proven that for any $f_0 \geq f_D$ the Problem 1f has solution with pairs (f_0, s_*) for any $s_* > 0$.

Theorem .3. *There exist choices of parameters (E_0, k_*) (of (f_0, s_*)) for which Problem 2 (Problem 2f) is not solvable.*

The relevant orbits for this case are the ones from O_{III} and the separatrix U_1. In the same way as in the previous theorem, one can show that s_* is a monotonously increasing function of g_0 for fixed f_0, and that $s_* \to 0$ for $g_0 \to +\infty$ at fixed f_0. But for any fixed f_0, the value of s_* is bounded from below by some finite $s_* < 0$ corresponding to U_1; let us call it s_{*U}. Thus we have proven that for any f_0 there exist $-\infty < s_{*U} < 0$ such that the Problem 2f does not have solution with pair (f_0, s_*) if $s_* < s_{*U}$ and has solution if $s_* \geq s_{*U}$.

Remark .5. *If we are interested in solutions with finite s_* at which both $f = \epsilon = 0$ then physically it makes sense to generalise the Problem 1f (2f) by postulating $f(s) \equiv 0$ in the range $s_* > s_{*H}$ ($s_* < s_{*U}$).*

Theorem .4. *There exist choices of parameters (E_0, E_1, k_1) (of (f_0, f_1, s_1)) for which Problem 3 (Problem 3f) is not solvable.*

This is the most general problem and relevant solutions may be given by orbits from all three parts of the phase plane. Clearly, in the limit $f_1 \to 0$ Problem 3f transforms into Problem 1f, and in the limit $f_0 \to 0$ and after shifting $s \to s - s_1$ it transforms into Problem 2f. Therefore by continuity we conclude from the previous two theorems that Problem 3f

has no solutions for sufficiently large s_1 and small f_0 or/and f_1. However, for $f_D < f_0 < f_1$ Problem 3f is solvable for any s_1. This follows from the monotonously increasing (decreasing) and unbounded dependence of s_1 on g_0 when the latter is above (below) U_2 when f_0 and f_1 are fixed. Indeed, $s_1 \to 0$ for $g_0 \to \pm\infty$ and $s_1 \to +\infty$ for $(g_0, f_0) \to U_2$. In particular, for large f or/and g the solutions become $f_{P,Q}$ and, using equation (B.8), we find P and Q for any (f_0, f_1, s_1):

$$P = c^{-3/2}\left[f_0^3 - f_1^3 e^{3(z-5/2)s_1}\right] / \left(1 - e^{-11s_1/2}\right), \tag{B.18}$$

$$Q = c^{-3/2}\left[f_0^3 - f_1^3 e^{(3z-2)s_1}\right] / \left(1 - e^{11s_1/2}\right). \tag{B.19}$$

.iii Case $z > 5/2$

In this case, $f(s)$ for the Kolmogorov and the thermodynamic spectra are decreasing. Since $z > 5/2$ then $D > 0$ and equation (B.4) again admits an exact positive solution $f(s) = f_D = 8\nu/D$.

The following technical Lemma will be used later.

Lemma .6. *Solutions of the Cauchy problems for equation (B.4) are always bounded functions together with* $f^2|df/ds|$.

It is easily established from the integral relation arising from (B.4):

$$2\left(f^2\frac{df}{ds}\right)^2(s) + (12z-19)\int_0^s f^4\left(\frac{df}{d\eta}\right)^2 d\eta + \Phi(f(s)) = \Phi(f_0) + 2\left(f^2\frac{df}{ds}\right)^2(0). \tag{B.20}$$

Since now $12z - 19 > 0$, it follows from (B.20) that

$$\Phi(f(s)) < |\Phi(f_0)| + 2\left(f^2\frac{df}{ds}\right)^2(0). \tag{B.21}$$

Therefore $f(s) < K$ where the constant K depends on $f(0)$, $df(0)/ds$, ν and z. The same holds for $f^2|df/ds|$ because $\Phi(f(s)) \geq \Phi(f_D)$.

Lemma .7. *The orbits of the dynamical system (5.10), (5.11) which intersect the line $g + f = 0$ cannot approach the g-axis for $g \leq 0$ as time τ evolves.*

Indeed, according to the formula (5.7), $\epsilon \leq 0$ above and on the thermodynamic line (this includes line $g + f = 0$) and $\epsilon > 0$ otherwise (including the g-axis for $g < 0$). But, according to equation (5.2), $d\epsilon/dk \leq 0$ (hence $d\epsilon/ds \leq 0$). Therefore the orbits starting on the line $g + f = 0$ cannot also approach the g-axis where $\epsilon > 0$ for $g \leq 0$.

Remark .6. *The flux ϵ for orbits which go to the stable node $P2$ takes arbitrary negative values as $k \to \infty$.*

Lemma .8. *There exist orbits (named by O_I-set) of the dynamical system (5.10), (5.11) which approach the g-axis for $g < 0$ of the phase plane (f, g). These orbits are always below of the Kolmogorov line.*

The velocity field $(df/d\tau, dg/d\tau)$ on the g-axis for $g < 0$ are directed down along this axis. By starting from different initial points near by the g-axis, we get orbits which asymptote to this axis with time as follows from the representation (B.16). If we change τ to the reverse time $\hat{\tau} = -\tau$ then these orbits go to infinity never intersecting the Kolmogorov line since the velocity field $G(f, -(1/3 + z)f) < 0$ i.e. is directed into the region $g + (z + 1/3)f < 0$.

Lemma .9. *There exists an orbit S_1 of the dynamical system (5.10), (5.11) which goes from infinity to the fixed point $P1$.*

Again, let us consider a Cauchy problem for the equation (B.4) with the initial data

$$f(0) = f_0 \equiv f_D - \varepsilon \quad \left.\frac{df}{ds}\right|_{s=0} = f_m < 0 \tag{B.22}$$

and proceed as in the case with $z < 2/3$. Consider the set $B = \{f_m < 0\}$ with the properties: the corresponding solutions of the Cauchy problem (B.4), (B.22) achieve a positive minimum at $s = s_{min}$. It is clear that this set is not empty.

Consider an algebraic second-order curve $g = g(f)$ determined by the condition $dg/d\tau = 0$. From (5.11) we have:

$$g = g(f): \quad 2(f+g)^2 + \left(6z - \frac{17}{2}\right) f(f+g) + \frac{D}{2} f^2 - 4\nu f = 0. \quad \text{(B.23)}$$

This curve goes through the fixed point $P1$. There exists a branch $g = g_1(f)$ of $g = g(f)$ which is located below of the Kolmogorov line since $dg/d\tau > 0$ along f^K. The velocity field $(df/d\tau, dg/d\tau)$ restricted on $g_1(f)$ has the components: $df/d\tau < 0$ and $dg/d\tau = 0$. Hence the orbits starting at $g \le g_1(f)$ will always remain in the region $g \le g_1(f)$, which implies $df/ds = g + f < 0$, i.e. $f(s)$ is a monotonously decreasing function. Therefore $f_B = \inf B$ exists: we have $f_B \ge g_1(f_0) + f_0$.

Repeating the same arguments as the ones we used before for the case $z < 2/3$, we get that there exists a solution of (B.4), (B.22) with the following property: the minimum of $f(s; f_B)$ is achieved at a point s_* where again $f = df/ds = 0$. Therefore there exists a solution of Problem 1f such that $f^2 df/ds = 0$ at $s = s_*$. This solution on the phase plane corresponds to an orbit S_1 which goes to $P1$. If we change the time on the inverse time $\hat{\tau}$ then S_1 emerges out the fixed point $P1$ and goes to infinity never intersecting the Kolmogorov line (see Lemma .8) and, therefore, never intersecting the line $g + f = 0$ (c.f. Lemma .7). This orbit corresponds to a monotonously increasing $f(\hat{\tau})$ which asymptotes to the pure Kolmogorov inviscid solution $f_{P,0}$. Here, $Q = 0$ follows from the fact that S_1 remains below the Kolmogorov line (implying $Q \le 0$) and the fact that for $Q < 0$ the solution $f_{P,Q}$ would not be monotonously increasing.

Thus, the orbit S_1 corresponds to a direct energy cascade whose energy flux is gradually decreased by the viscous dissipation, so that both the spectrum and the energy flux turn into zero at a finite wave number $k_* = k_0 e^s$.

Lemma .10. *There exists an orbit H of the dynamical system (5.10), (5.11) connecting $P1$ with $P2$ (a heteroclinic connection).*

Recall that there are always two (and only two) orbits connecting to $P1$, see section II.iv. One of them, entering into $P1$, is the orbit S_1 discussed

above. Let us call the other orbit by H—it is emerging out of $P1$ into the first quadrant. By Lemma .6, $f(s)$ for such an orbit is bounded. By the same Lemma, $|g(s)|$ is bounded too provided that f is bounded from below, which is indeed the case, if we start on H stepping slightly away from $P1$. In this case f cannot approach zero at $g < 0$ because this would mean achieving a positive flux ϵ which is impossible since the staring flux is negative and $\epsilon(s)$ cannot increase. Neither f can approach zero at $g > 0$ because the vector field there is directed toward positive f. Thus, both $f(s)$ and $|g(s)|$ are bounded, and the orbit H goes to the fixed point $P2$ by the Poincaré-Bendixon theorem.

Lemma .11. *The orbits starting at the line $g + f = 0$ approach the g-axis for $g > 0$ in the reverse time, $\hat{\tau} \to \infty$, for $f_0 \geq f_D$.*

In order to prove Lemma .11, we consider the Cauchy problem for equation (B.4)

$$f(0) = f_0, \quad \left.\frac{df}{ds}\right|_{s=0} = 0, \quad s < 0. \tag{B.24}$$

The proof is similar to the case of $z < 2/3$ and is based on the same integral identity (B.10), but now for $s < 0$. In fact, all orbits $f_0 \geq f_D$ approach the g-axis as they approach the g-axis for $f_0 \geq 48\nu/5D$ and cannot intersect the orbit H. Asymptotic analysis of (5.10), (5.11) near the g-axis for $g > 0$ gives again $f \to (4C_1/9)|s - s_*|^{3/4}$ as $s \to s_*$ for a finite s_* and constant C_1 i.e. $f(s)$ vanishes at a finite point.

Lemma .12. *There exists an orbit S_2 of the dynamical system (5.10), (5.11) which goes from infinity to the fixed point $P2$. Orbit S_2 asymptotes to the thermodynamic line in the reverse time, so that $f \to f_{0,Q}$ as $\hat{\tau} \to \infty$.*

Any orbit starting on or above the thermodynamic line and with $f_0 > 0$ will end at $P2$. This can be shown in the same way as in the proof that H goes to $P2$ in Lemma .10. Reversed in time, all these orbits go to the regions where either $f \to \infty$ or/and $|g| \to \infty$, so that $f \to f_{P,Q}$ with $Q > 0$ and P either positive, or negative, or zero. The orbit corresponding to $P = 0$ is S_2: it emanates from $P2$ and asymptotes to the thermodynamic line. Orbits with $P > 0$ asymptote to the Kolmogorov line, because for any

finite positive P and Q the P-part wins in $f_{P,Q}(s)$ at $s \to -\infty$. We will call the set of these orbits O_{II}. Orbits with $P < 0$ correspond to $f(s)$ that vanishes at finite $s = s_* < 0$. We will call the set of these orbits O_{III}.

Remark .7. *The orbits from O_{III} are located above the thermodynamic line and, therefore, characterised by the flux ϵ which is negative. The orbits which approach the g-axis for $g < 0$ (we will call then the O_I-set) lie below the Kolmogorov line can be characterised, for large f or/and g, by negative temperature Q. Note that for the same orbit, the value of Q is usually different near the g-axis from its value for large f.*

Summarising, we have the following classification of the orbits.

Theorem .5. *S_1 and $H \cup S_2 \cup P2$ divide the phase plane (f, g) ($f > 0$, $-\infty < g < \infty$) into parts I, II and III with different behaviors of orbits. In part I (below S_1) the orbits always approach the g-axis for $g < 0$. Between S_1 and $H \cup S_2 \cup P2$, i.e. in II, the orbits go from infinity along S_1 to the stable node $P2$. Some of these orbits have an intermediate asymptotics—the S_2 orbit. Part III contains the orbits located above $H \cup S_2 \cup P2$. For the reverse time $\hat{\tau}$, the orbits emerge out the unstable node $P2$ and go to the first quadrant approaching the g-axis.*

Similarly to how it was done in the case $z < 2/3$, one can prove that the Problems 1, 2 and 3 (and respectively 1f, 2f and 3f) are not solvable for some sets of parameters.

.iv Case $2/3 < z < 5/2$

We have the following three possibilities: $12z - 19 > 0$, $12z - 19 < 0$ and $12z - 19 = 0$.

Consider the case of $12z - 19 \geq 0$ and give a qualitative analysis of the behavior of orbits. If we start on the line $g + f = 0$ then we have from the integral identity (B.10):

$$\Phi(f(s)) \leq \Phi(f_0). \tag{B.25}$$

Since $\Phi(f(s))$ is a negative monotonously decreasing function, it follows from (B.25) that $f(s) > f_0 > 0$. The maximum principle guarantees that no

local maximum of $f(s)$ can be achieved on the interval $(0, \infty)$. Indeed, since $D < 0$, according to (B.4) the second derivative of $f(s)$ cannot be negative at points where $df(s)/ds = 0$. Therefore the solutions $f(s)$ monotonously increase. This can also be easily observed from the phase analysis of the dynamical system (5.10), (5.11). Consider the angle $\Gamma : \{g = 0, g + f = 0\}$, $g < 0$ of the plane (f, g). The direction of the velocity field $(df/d\tau, dg/d\tau)$ restricted on the line $g + f = 0$ is directed into Γ. Therefore orbits cannot leave Γ with time.

Lemma .13. *There exist orbits which approach the g-axis for $g < 0$. Also there exist an orbit S_1 which goes to the fixed point $P1$. This orbit is located below the Kolmogorov line.*

Consider the dynamical system (5.10), (5.11) and the algebraic curve (B.23). This curve goes through the fixed point $P1$. Consider the angle $\Lambda : \{f = 0, g + f = 0\}$ with $g < 0$. The vector field $(df/d\tau, dg/d\tau)$ on the g-axis has components $(0, -g^2)$ and $dg/d\tau > 0$ on $g + f = 0$ except the fixed point $P1$. Therefore there exists a branch $g = g_1(f)$ of $g = g(f)$ which is located inside of Λ. The velocity field $(df/d\tau, dg/d\tau)$ restricted on $g_1(f)$ has the components: $df/d\tau < 0$ and $dg/d\tau = 0$. Hence $(df/d\tau, dg/d\tau)$ is directed into $\Psi_1 : \{f = 0, g = g_1(f)\}$ and orbits do not leave Ψ_1. This means that there exists a set of initial data

$$f(0) = f_0, \quad \left.\frac{df}{ds}\right|_{s=0} = f_m, \quad f_m < 0 \tag{B.26}$$

such that solutions of (B.4), (B.26) are monotonously decreasing functions (because region Ψ_1 is below the line $f + g = 0$). Local solvability of the problem (B.4),(B.26) follows from the theory of ODE. Thus, there exist two families of orbits. The first family O_I presents orbits which cross the curve $g_1(f) = 0$ approaching the g-axis. The second family O_{II} consists of the orbits which go into Γ. Therefore, there must be an orbit S_1 which splits O_I and O_{II}. The existence of S_1 can be proven by using the same arguments as before. Consider a Cauchy problem for the equation (B.4)

with the following condition:

$$f(0) = f_0, \quad \left.\frac{df}{ds}\right|_{s=0} = f_m < 0 \tag{B.27}$$

with arbitrary $f_0 > 0$. Define set $E = \{f_m\}$ with the properties: the corresponding solution of the Cauchy problem has a positive minimum at some $s = s_{min}$. This set is not empty and bounded from below in view of the discussion above. Denote by $f_E = \inf E$ and let $f(s; f_E)$ be a solution of (B.4), (B.27). As before (c.f. the proof of Lemma .3), we conclude that there exists a finite s_* such that $f(s_*; f_E) = 0$ together with $f^2(s; f_E)df(s; f_E)/ds|_{s=s_*}$. This solution corresponds to the orbit S_1 which goes to $P1$. The orbit S_1, and therefore all the orbits from O_I, are always below the Kolmogorov line because the velocity field is crossing this line in the upward direction (i.e. when traced back in time S_1 will not cross the Kolmogorov line).

Lemma .14. *There exist orbits which approach the g-axis for $g > 0$ as the reverse time $\hat{\tau} \to \infty$. Also there exists an orbit U_1 which emerges out the fixed point $P1$. This orbit asymptotes to $f_{P,Q}$ with $Q > 0$ and $P < 0$, and lies above of the thermodynamic line.*

Consider orbits from O_{II}. These orbits go to infinity and, after crossing the line $f + g = 0$, the corresponding $f(\tau)$ monotonously grow to infinity. The orbits cross the thermodynamic line and then asymptote towards it as $\tau \to \infty$. In reverse time $f(\hat{\tau})$ also grows monotonously to infinity after crossing the line $f + g = 0$. The orbits cross the Kolmogorov line and then asymptote towards it as $\hat{\tau} \to \infty$. Thus for each O_{II}-orbit asymptotically the value of the energy flux tends to a positive constant at the right boundary of the s-interval and to a negative constant at the left boundary. Physically, this corresponds to a system with two energy sources at both ends of the wave number range which produce energy fluxes from the boundaries toward the middle of the wave number range, gradually decreased by the viscosity and turning into zero at some point within the wave number range.

The vector field $(df/d\tau, dg/d\tau)$ restricted on the g-axis for $g > 0$ towards to the fixed point $P1$. Therefore there exist orbits which approach the g-axis

with $g > 0$ as the reverse time $\hat{\tau} \to \infty$. We shall denote these orbits by O_{III}. The orbits from O_{III} asymptote to the thermodynamic line as $\tau \to \infty$. The proof is the same as in the case of $z < 2/3$. Notice that $(df/d\tau, dg/d\tau)$ restricted on the second branch $g = g_2(f)$ of the algebraic curve (B.23) is directed into $\Psi_2 : \{g = g_2(f), f = 0\}$ and $g = g_2(f)$ is above of the line $g + f = 0$. This means that orbits from O_{III} are always inside Ψ_2. O_{II} and O_{III} present orbits with different behaviours. The existence of an orbit which splits up O_{II} and O_{III} can be proven by using the same argument as in Lemma .5. We denote this orbit by U_1 and in terms of the reverse time $\hat{\tau}$ the orbit U_1 realizes a solution of Problem 2f such that $s_* < 0$, $|s_*| < \infty$ and $f^2(s)df(s)/ds$ vanishes at $s = s_*$. The family O_{III} corresponds to solutions of Problem 2f which vanish at finite times with $f^2 df/ds \neq 0$ at these points. Here again we use the asymptotic solution $f(s) \approx (4C_1/9)|s - s_*|^{3/4}$ near the g-axis with $g > 0$.

The case $12z - 19 < 0$ is considered similar with the same classification theorem for orbits of the dynamical system. Summarizing the results, we have the following classification of the orbits.

Theorem .6. *The orbits S_1 and U_1 divide the phase plane on I, II and III parts with different behaviors of orbits. The orbits from I go along the separatrix S_1 approaching the g-axis at $g < 0$ with a finite flux, $\epsilon > 0$. Part II consists of the orbits located between S_1 and U_1, the latter representing asymptotes for each of these orbits as $\hat{\tau} \to \infty$ and $\tau \to \infty$ respectively. For these orbits $\epsilon < 0$ as $\tau \to \infty$ and $\epsilon > 0$ as $\hat{\tau} \to \infty$. The set III represents orbits emerging at the first quadrant and approaching U_1 with time. For the reverse time $\hat{\tau}$ these orbits approach the g-axis at $g > 0$ as $\hat{\tau} \to \infty$ with a finite flux, $\epsilon < 0$.*

Similarly to how it was done in the case $z < 2/3$, one can prove that the Problems 1, 2 and 3 (and respectively 1f, 2f and 3f) are not solvable for some sets of parameters.

Remark .8. *Generalising Remark .5 for any z: one can extend the Problem 1f (2f) in which $f(s_*) = \epsilon(s_*) = 0$ by postulating $f(s) \equiv 0$ for s which is greater (less) than the maximal (minimal) allowed s_*.*

Bibliography

[1] http://www.fftw.org.

[2] Abad, M., Guilleumas, M., Mayol, R., Piazza, F., Jezek, D. M., and Smerzi, A. Phase slips and vortex dynamics in Josephson oscillations between Bose-Einstein condensates. *EPL*, 109(4):40005, 2015.

[3] D. Acheson and F. Acheson. *Elementary Fluid Dynamics*. Comparative Pathobiology - Studies in the Postmodern Theory of Education. Clarendon Press, 1990.

[4] M. Albiez, R. Gati, J. Fölling, S. Hunsmann, M. Cristiani, and M. K. Oberthaler. Direct observation of tunneling and nonlinear self-trapping in a single bosonic Josephson junction. *Phys. Rev. Lett.*, 95:010402, Jun 2005.

[5] J. Auer, E. Krotscheck, and S. A. Chin. A fourth-order real-space algorithm for solving local schrödinger equations. *The Journal of Chemical Physics*, 115(15):6841–6846, 2001.

[6] A. W. Baggaley and C. F. Barenghi. Tree method for quantum vortex dynamics. *Journal of Low Temperature Physics*, 166(1):3–20, 2012.

[7] A. Baggaley and C. Barenghi. Spectrum of turbulent kelvin-waves cascade in superfluid helium. *Phys. Rev. B*, 83(13):134509, 2011.

[8] A. W. Baggaley and C. F. Barenghi. Decay of homogeneous two-dimensional quantum turbulence. *Phys. Rev. A*, 97:033601, Mar 2018.

[9] A. W. Baggaley and J. Laurie. Kelvin-wave cascade in the vortex filament model. 89(1):014504, January 2014.

[10] C. F. Barenghi, V. S. L'vov, and P.-E. Roche. Experimental, numerical, and analytical velocity spectra in turbulent quantum fluid. *Proceedings of the National Academy of Sciences*, 111(Supplement 1):4683–4690, 2014.

[11] C. Barenghi and R. Donnelly. Vortex rings in classical and quantum systems. *Fluid Dyn. Res.*, 41(051401), 2009.

[12] C. Barenghi, N. Parker, N. Proukakis, and C. Adams. Decay of quantised vorticity by sound emission. *J. Low Temp. Phys.*, 629(138), 2005.

[13] G. K. Batchelor. *An Introduction to Fluid Dynamics*. Cambridge University Press, Cambridge, 2000.

[14] G. Baym, R. I. Epstein, and B. Link. Dynamics of vortices in neutron stars. *Physica B: Condensed Matter*, 178(1):1–12, 1992.

[15] V. Berezinskii. *Destruction of Long-range Order in One-dimensional and Two-dimensional Systems having a Continuous Symmetry Group I. Classical Systems*, volume 32 of *3*. JETP, 1971.

[16] N. G. Berloff and P. H. Roberts. Capture of an impurity by a vortex line in a Bose condensate. *Phys. Rev. B*, 63(2):024510, January 2001.

[17] G. P. Bewley, D. P. Lathrop, and K. R. Sreenivasan. Superfluid helium: Visualization of quantized vortices. *Nature*, 441(7093):588–588, 2006.

[18] G. P. Bewley, M. S. Paoletti, K. R. Sreenivasan, and D. P. Lathrop. Characterization of reconnecting vortices in superfluid helium. *Proceedings of the National Academy of Sciences*, 105(37):13707, 09 2008.

[19] A. S. Bradley and B. P. Anderson. Energy Spectra of Vortex Distributions in Two-Dimensional Quantum Turbulence. 2(4):041001, October 2012.

[20] A. Burchianti, C. Fort, and M. Modugno. Josephson plasma oscillations and the Gross-Pitaevskii equation: Bogoliubov approach versus two-mode model. *Phys. Rev. A*, 95:023627, Feb 2017.

[21] T. Byrnes, N. Y. Kim, and Y. Yamamoto. Exciton–polariton condensates. *Nature Physics*, 10:803 EP –, 10 2014.

[22] F. S. Cataliotti, S. Burger, C. Fort, P. Maddaloni, F. Minardi, A. Trombettoni, A. Smerzi, and M. Inguscio. Josephson junction arrays with Bose-Einstein condensates. *Science*, 293(5531):843–846, 2001.

[23] Y. A. Chirkunov, S. V. Nazarenko, S. B. Medvedev, and V. N. Grebenev. Invariant solutions for the nonlinear diffusion model of turbulence. *Phys A: Math. Theor.*, 47(18 185501), 2014.

[24] S. Choi, S. A. Morgan, and K. Burnett. Phenomenological damping in trapped atomic Bose-Einstein condensates. *Phys. Rev. A*, 57:4057–4060, May 1998.

[25] C. Cichowlas, P. Bonaïti, F. Debbasch, and M. Brachet. Effective Dissipation and Turbulence in Spectrally Truncated Euler Flows. *Phys. Rev. Letters.*, 95(26):264502, 2005.

[26] A. Cidrim, F. E. A. dos Santos, L. Galantucci, V. S. Bagnato, and C. F. Barenghi. Controlled polarization of two-dimensional quantum turbulence in atomic Bose-Einstein condensates. *Phys. Rev. A*, 93(033651), 2016.

[27] A. Cidrim, A. C. White, A. J. Allen, V. S. Bagnato, and C. F. Barenghi. Vinen turbulence via the decay of multicharged vortices in trapped atomic Bose-Einstein condensates. *Phys. Rev. A*, 96:023617, Aug 2017.

[28] C. Connaughton and S. Nazarenko. A model differential equation for turbulence. *arXiv e-prints*, page physics/0304044, Apr 2003.

[29] M. C. Davis, R. Carretero-Gonzalez, Z. Shi, K. J. H. Law, P. G. Kevrekidis, and B. P. Anderson. Manipulation of vortices by localized

impurities in Bose-Einstein condensates. *Phys. Rev. A*, 80(023604), 2009.

[30] R. Desbuquois, L. Chomaz, T. Yefsah, J. Léonard, J. Beugnon, C. Weitenberg, and J. Dalibard. Superfluid behaviour of a two-dimensional Bose gas. *Nature Physics*, 8:645 EP –, 07 2012.

[31] R. J. Donnelly and P. H. Roberts. Stochastic theory of the interaction of ions and quantized vortices in helium ii. *Proceedings of the Royal Society of London. Series A, Mathematical and Physical Sciences*, 312(1511):519–551, 1969.

[32] R. J. Donnelly. *Quantized Vortices in Helium II*. Cambridge University Press, March 1991.

[33] D. Duda, P. Švančara, M. La Mantia, M. Rotter, and L. Skrbek. Visualization of viscous and quantum flows of liquid ^{4}He due to an oscillating cylinder of rectangular cross section. *Phys. Rev. B*, 92:064519, Aug 2015.

[34] C. P. Ellington, C. van den Berg, A. P. Willmott, and L. R. Thomas. Bottleneck phenomenon in developed turbulence. *Phys.*, 6(1411), 1994.

[35] G. Falkovich and N. Vladimirova. Cascades in nonlocal turbulence. *Phys. Rev. E*, 91:041201, Apr 2015.

[36] A. Fetter and A. Svidzinsky. Vortices in a trapped dilute Bose-Einstein condensate. *J. Phys. Cond. Mat.*, 13(R135), 2001.

[37] R. P. Feynman. Application of quantum mechanics to liquid helium. *Progress in low temperature physics*, 1(1):17–53, 1955.

[38] R. P. Feynman. Chapter II Application of Quantum Mechanics to Liquid Helium. In C. J. Gorter, editor, *Progress in Low Temperature Physics*, volume 1, pages 17–53. Elsevier, 1955.

[39] E. Fonda, D. P. Meichle, N. T. Ouellette, S. Hormoz, and D. P. Lathrop. Direct observation of kelvin waves excited by quantized vortex reconnection. *Proceedings of the National Academy of Sciences*, 111(Supplement 1):4707, 03 2014.

[40] S. Galtier, S. V. Nazarenko, A. C. Newell, and A. Pouquet. A weak turbulence theory for incompressible magnetohydrodynamics. *J. Plasma Phys*, 63(5):447–488, 2000.

[41] G. Gauthier, M. T. Reeves, X. Yu, A. S. Bradley, M. A. Baker, T. A. Bell, H. Rubinsztein-Dunlop, M. J. Davis, and T. W. Neely. Giant vortex clusters in a two-dimensional quantum fluid. *Science*, 364(6447):1264, 06 2019.

[42] V. N. Grebenev, A. Griffin, S. B. Medvedev, and S. V. Nazarenko. Steady states in leith's model of turbulence. 49(36):365501, 2016.

[43] V. N. Grebenev, S. V. N. S. B. Medvedev, I. V. Schwab, and Y. A. Chirkunov. Self-similar solution in leith model of turbulence: anomalous power law and asymptotic analysis. *J. Phys. A: Math. Theor.*, 47(2 025501), 2014.

[44] A. Griffin, G. W. Stagg, N. P. Proukakis, and C. F. Barenghi. Vortex scattering by impurities in a Bose Einstein condensate. *Journal of Physics B: Atomic, Molecular and Optical Physics*, 50(11):115003, 2017.

[45] E. P. Gross. Structure of a quantized vortex in Boson systems. *NUOVO CIMENTO*, XX(3):454–477, 1961.

[46] A. Groszek, T. Simula, D. Paganin, and K. Helmerson. Onsager vortex formation in Bose-Einstein condensates in two-dimensional power-law traps. *Phys. Rev. A*, 93(043614), 2016.

[47] W. Guo, M. La Mantia, D. P. Lathrop, and S. W. Van Sciver. Visualization of two-fluid flows of superfluid helium-4. *Proceedings of the National Academy of Sciences*, 111(Supplement 1):4653–4658, 2014.

[48] S. Gustafson and F. Ting. Dynamic stability and instability of pinned fundamental vortices. *Journal of Nonlinear Science*, 19(4):341–374, 2009.

[49] E. A. L. Henn, J. A. Seman, G. Roati, K. M. F. Magalhães, and V. S. Bagnato. Emergence of Turbulence in an Oscillating Bose-Einstein Condensate. 103(4):045301, July 2009.

[50] E. Herbert, F. Daviaud, B. Dubrulle, S. Nazarenko, and A. Naso. Dual non-kolmogorov cascades in a von kármán flow. 100(4):44003, 2012.

[51] N. Šantić, A. Fusaro, S. Salem, J. Garnier, A. Picozzi, and R. Kaiser. Nonequilibrium precondensation of classical waves in two dimensions propagating through atomic vapors. *Phys. Rev. Lett.*, 120:055301, Feb 2018.

[52] S. P. Johnstone, A. J. Groszek, P. T. Starkey, C. J. Billington, T. P. Simula, and K. Helmerson. Evolution of large-scale flow from turbulence in a two-dimensional superfluid. *Science*, 364(6447):1267, 06 2019.

[53] C. A. Jones and P. H. Roberts. Motions in a Bose condensate axisymmetric solitary waves. *Journal of Physics A: Mathematical and General*, 15(8):2599, 1982.

[54] B. Josephson. Possible new effects in superconductive tunnelling. *Physics Letters*, 1(7):251 – 253, 1962.

[55] P. Kapitza. Viscosity of liquid helium below the lambda-point. *Nature*, 141(3558):74–74, 1938.

[56] T. W. B. Kibble. Some implications of a cosmological phase transition. *Physics Reports*, 67(1):183–199, 1980.

[57] A. Kolmogorov. The Local Structure of Turbulence in Incompressible Viscous Fluid for Very Large Reynolds' Numbers. *Akademiia Nauk SSSR Doklady*, 30:301–305, 1941.

[58] J. M. Kosterlitz and D. J. Thouless. Ordering, metastability and phase transitions in two-dimensional systems. *Journal of Physics C: Solid State Physics*, 6(7):1181–1203, apr 1973.

[59] G. Krstulovic and M. Brachet. Energy cascade with small-scale thermalization, counterflow metastability, and anomalous velocity of vortex rings in Fourier-truncated Gross-Pitaevskii equation. *Phys. Rev. E*, 83:066311, Jun 2011.

[60] G. Krstulovic. Kelvin-wave cascade and dissipation in low-temperature superfluid vortices. 86(5):055301, November 2012.

[61] E. A. Kuznetsov and S. K. Turitsyn. Soliton instability and collapse in media with defocusing nonlinearity. *Zhurnal Eksperimental noi i Teoreticheskoi Fiziki*, 94:119–129, 07 1988.

[62] W. J. Kwon, G. Moon, J. Choi, S. Seo, and Y. Shin. Relaxation of superfluid turbulence in highly oblate Bose-Einstein condensates. *Phys. Rev. A*, 90(063627), 2014.

[63] H. Lamb. *Hydrodynamics*. University Press, 1916.

[64] C. Leith. Diffusion approximation to inertial energy transfer in isotropic turbulence. *Phys. Fluids*, 10(1409), 1967.

[65] S. Levy, E. Lahoud, I. Shomroni, and J. Steinhauer. The a.c. and d.c. Josephson effects in a Bose-Einstein condensate. *Nature*, 449(7162):579–583, 10 2007.

[66] R. Lopes, C. Eigen, N. Navon, D. Clément, R. P. Smith, and Z. Hadzibabic. Quantum depletion of a homogeneous Bose-Einstein condensate. *Phys. Rev. Lett.*, 119:190404, Nov 2017.

[67] V. S. Lvov, S. V. Nazarenko, and G. E. Volovik. Energy spectra of developed superfluid turbulence. *J. Exper. Theor. Phys. Letters*, 80(7):479–483, 2004.

[68] V. S. L'vov, S. V. Nazarenko, and O. Rudenko. Bottleneck crossover between classical and quantum superfluid turbulence. *Phys. Rev. B*, 76:024520, Jul 2007.

[69] K. W. Madison, F. Chevy, W. Wohlleben, and J. Dalibard. Vortex formation in a stirred Bose-Einstein condensate. *Phys. Rev. Lett.*, 84:806–809, Jan 2000.

[70] M. R. Matthews, B. P. Anderson, P. C. Haljan, D. S. Hall, C. E. Wieman, and E. A. Cornell. Vortices in a Bose-Einstein condensate. *Phys. Rev. Lett.*, 83:2498–2501, Sep 1999.

[71] J. Maurer and P. Tabeling. Local investigation of superfluid turbulence. 43(1):29, July 1998.

[72] S. McGee and M. Holland. Rotational dynamics of vortices in confined Bose-Einstein condensates. *Phys. Rev. A*, 63(043608), 2001.

[73] C. Michel, O. Boughdad, M. Albert, P.-É. Larré, and M. Bellec. Superfluid motion and drag-force cancellation in a fluid of light. *Nature Communications*, 9(1):2108, 2018.

[74] V. A. Mironov and L. A. Smirnov. Scattering of two-dimensional dark quasi-solitons by smooth inhomogeneities in a Bose-Einstein condensate. *Physics of Wave Phenomena*, 21(1):62–67, Jan 2013.

[75] M. E. Mossman, M. A. Hoefer, K. Julien, P. G. Kevrekidis, and P. Engels. Dissipative shock waves generated by a quantum-mechanical piston. *Nature Communications*, 9(1):4665, 2018.

[76] M. Möttönen, T. Mizushima, T. Isoshima, M. M. Salomaa, and K. Machida. Splitting of a doubly quantized vortex through intertwining in Bose-Einstein condensates. *Phys. Rev. A*, 68:023611, Aug 2003.

[77] N. Navon, A. L. Gaunt, R. P. Smith, and Z. Hadzibabic. Emergence of a turbulent cascade in a quantum gas. *Nature*, 539:72 EP –, 11 2016.

[78] S. Nazarenko and M. Onorato. Wave turbulence and vortices in Bose–Einstein condensation. 219(1):1–12, July 2006.

[79] S. Nazarenko and M. Onorato. Freely decaying turbulence and Bose–Einstein condensation in Gross–Pitaevski model. *J. Low Temp. Phys.*, 146(31), 2007.

[80] S. Nazarenko. Wave turbulence. *Lecture Notes in Physics*, 2011.

[81] S. Nazarenko. *Wave Turbulence*. Springer, 2011 edition, February 2011.

[82] T. W. Neely, A. S. Bradley, E. C. Samson, S. J. Rooney, E. M. Wright, K. J. H. Law, R. Carretero-González, P. G. Kevrekidis, M. J. Davis, and B. P. Anderson. Characteristics of Two-Dimensional Quantum Turbulence in a Compressible Superfluid. *Phys. Rev. Lett.*, 111(23):235301, December 2013.

[83] A. Newell. *Nonlinear optics*. CRC Press, 2018.

[84] C. Nore, M. Abid, and M. Brachet. Kolmogorov turbulence in low-temperature superflows. 78(20):3896–3899, May 1997.

[85] C. Nore, M. Abid, and M. E. Brachet. Decaying kolmogorov turbulence in a model of superflow. 9(9):2644–2669, September 1997.

[86] R. Numasato, M. Tsubota, and V. L'vov. Direct energy cascade in two-dimensional compressible quantum turbulence. *Physical Review A*, 81, 02 2010.

[87] L. Onsager. Statistical hydrodynamics. *Nuovo Cimento*, 6(2):281, 1949.

[88] R. Pandit, D. Banerjee, A. Bhatnagar, M. Brachet, A. Gupta, D. Mitra, N. Pal, P. Perlekar, S. S. Ray, V. Shukla, and D. Vincenzi. An overview of the statistical properties of two-dimensional turbulence in fluids with particles, conducting fluids, fluids with polymer additives, binary-fluid mixtures, and superfluids. *Phys. Fluids*, 29(11):111112, 2017.

[89] L. P. Pitaevskii. Vortex lines in an imperfect Bose gas. *Soviet Physics JETP*, 13(2):451–454, 1961.

[90] L. P. Pitaevskii and S. Stringari. *Bose-Einstein Condensation*. Oxford University Press, 2003.

[91] L. F. Richardson and W. N. Shaw. The supply of energy from and to atmospheric eddies. *Proceedings of the Royal Society of London. Series A, Containing Papers of a Mathematical and Physical Character*, 97(686):354–373, 2019/09/21 1920.

[92] A. A. Samarskii, V. A. Galaktionov, S. P. Kurdyumov, and A. D. Mikhailov. Blow-up in quasilinear parabolic equation. *Berlin, New York: Walter de Gruyter*, page 533, 1995.

[93] K. Schwarz. Three-dimensional vortex dynamics in superfluid ^{4}He: Line-line and line-boundary interactions. 31(9):5782–5804, May 1985.

[94] K. W. Schwarz. Three-dimensional vortex dynamics in superfluid ^{4}He: Homogeneous superfluid turbulence. *Phys. Rev. B*, 38:2398–2417, Aug 1988.

[95] Y. Shin, M. Saba, M. Vengalattore, T. A. Pasquini, C. Sanner, A. E. Leanhardt, M. Prentiss, D. E. Pritchard, and W. Ketterle. Dynamical instability of a doubly quantized vortex in a Bose-Einstein condensate. *Phys. Rev. Lett.*, 93:160406, Oct 2004.

[96] V. Shukla, M. Brachet, and R. Pandit. Turbulence in the two-dimensional Fourier-truncated Gross-Pitaevskii equation. *New J. Phys.*, 15(11):113025, 2013.

[97] V. Shukla, M. Brachet, and R. Pandit. Sticking transition in a minimal model for the collisions of active particles in quantum fluids. *Phys. Rev. A*, 94:041602, Oct 2016.

[98] V. Shukla, P. D. Mininni, G. Krstulovic, P. C. di Leoni, and M. E. Brachet. Quantitative estimation of effective viscosity in quantum turbulence. *Phys. Rev. A*, 99:043605, Apr 2019.

[99] V. Shukla, A. Gupta, and R. Pandit. Homogeneous isotropic superfluid turbulence in two dimensions: Inverse and forward cascades in the Hall-Vinen-Bekharevich-Khalatnikov model. *Phys. Rev. B*, 92(10):104510, September 2015.

[100] V. Shukla, R. Pandit, and M.-E. Brachet. Particles and fields in superfluids: Insights from the two-dimensional Gross-Pitaevskii equation. *Physical Review A*, 97, 10 2017.

[101] L. Skrbek and W. Vinen. The use of vibrating structures in the study of quantum turbulence. In *Progress in Low Temperature Physics*, volume 16, pages 195–246. Elsevier, 2009.

[102] L. Smirnov and A. Smirnov. Scattering of two-dimensional dark solitons by a single quantum vortex in a Bose-Einstein condensate. *Phys. Rev.A*, 92:013636, 2015.

[103] D. Sorensen, R. Lehoucq, C. Yang, and K. Maschhoff. Arpack-an implementation of the implicitly restarted arnoldi method for computing a few selected eigenvalues and corresponding eigenvectors of a large sparse matrix, 1996.

[104] G. Spagnolli, G. Semeghini, L. Masi, G. Ferioli, A. Trenkwalder, S. Coop, M. Landini, L. Pezzè, G. Modugno, M. Inguscio, A. Smerzi, and M. Fattori. Crossing over from attractive to repulsive interactions in a tunneling bosonic Josephson junction. *Phys. Rev. Lett.*, 118:230403, Jun 2017.

[105] G. Stagg, A. Allen, N. Parker, and C. Barenghi. Generation and decay of two-dimensional quantum turbulence in a trapped Bose-Einstein condensate. *Phys. Rev. A*, 91(013612), 2015.

[106] K. Suthar, A. Roy, and D. Angom. Acoustic radiation from vortex barrier interaction in atomic Bose Einstein condensate. *Journal of Physics B: Atomic, Molecular and Optical Physics*, 47(13):135301, 2014.

[107] T. K. T. Aioi, T. Kishimoto, and H. Saito. Propagation of sound in a Bose-Einstein condensate. *Phys. Rev. X*, 1(021003), 2011.

[108] G. I. Taylor. Statistical theory of turbulence. *Proceedings of the Royal Society of London. Series A - Mathematical and Physical Sciences*, 151(873):421–444, 2019/11/27 1935.

[109] R. Teles, F. dos Santos, and V. Bagnato. Stability change of a multi-charged vortex due to coupling with quadrupole mode. *arXiv e-prints*, page arXiv:1505.06227, May 2015.

[110] S. Thalabard, S. V. Nazarenko, S. Galtier, and S. B. Medvedev. Anomalous spectral laws in differential models of turbulence. *J. Phys. A: Math. Theor.*, 48(28 285501), 2015.

[111] A. Tonomura, H. Kasai, O. Kamimura, T. Matsuda, K. Harada, J. Shimoyama, K. Kishio, and K. Kitazawa. Motion of vortices in superconductors. *Nature*, 397(6717):308–309, 1999.

[112] D. Tritton. *Physical Fluid Dynamics*. Oxford Science Publ. Clarendon Press, 1988.

[113] M. Tsubota, T. Araki, and C. F. Barenghi. Rotating superfluid turbulence. *Phys. Rev. Lett.*, 90:205301, May 2003.

[114] G. Valtolina, A. Burchianti, A. Amico, E. Neri, K. Xhani, J. A. Seman, A. Trombettoni, A. Smerzi, M. Zaccanti, M. Inguscio, and G. Roati. Josephson effect in fermionic superfluids across the BEC-BCS crossover. *Science*, 350(6267):1505–1508, 2015.

[115] E. Varga, C. F. Barenghi, Y. A. Sergeev, and L. Skrbek. Backreaction of tracer particles on vortex tangle in helium ii counterflow. *Journal of Low Temperature Physics*, 183(3):215–221, 2016.

[116] A. Villois, G. Krstulovic, D. Proment, and H. Salman. A vortex filament tracking method for the Gross–Pitaevskii model of a superfluid. *Journal of Physics A: Mathematical and Theoretical*, 49(41):415502, sep 2016.

[117] W. F. Vinen. The detection of single quanta of circulation in liquid helium ii. *Proceedings of the Royal Society of London. Series A, Mathematical and Physical Sciences*, 260(1301):218–236, 1961.

[118] L. Warszawski, A. Melatos, and N. G. Berloff. Unpinning triggers for superfluid vortex avalanches. *Phys. Rev. B*, 85:104503, Mar 2012.

[119] J. B. Weiss and J. C. McWilliams. Nonergodicity of point vortices. *Physics of Fluids A: Fluid Dynamics*, 3(5):835–844, 2019/06/26 1991.

[120] A. C. White, B. P. Anderson, and V. S. Bagnato. Vortices and turbulence in trapped atomic condensates. *Proceedings of the National Academy of Sciences*, 111(1):4719–4726, 2014.

[121] G. A. Williams, K. DeConde, and R. E. Packard. Positive-ion trapping on vortex lines in rotating he ii. *Phys. Rev. Lett.*, 34:924–926, Apr 1975.

[122] P. D. Williams. Increased light, moderate, and severe clear-air turbulence in response to climate change. *Advances in Atmospheric Sciences*, 34(5):576–586, 2017.

[123] A. W. Woods. Turbulent plumes in nature. *Annual Review of Fluid Mechanics*, 42(1):391–412, 2019/09/21 2009.

[124] K. Xhani, E. Neri, L. Galantucci, F. Scazza, A. Burchianti, K.-L. Lee, C. Barenghi, A. Trombettoni, M. Inguscio, M. Zaccanti, et al. Critical transport and vortex dynamics in a thin atomic Josephson junction. *arXiv preprint arXiv:1905.08893*, 2019.

[125] R. M. B. Young and P. L. Read. Forward and inverse kinetic energy cascades in jupiter's turbulent weather layer. *Nature Physics*, 13:1135 EP –, 08 2017.

[126] V. E. Zakharov. Stability of periodic waves of finite amplitude on the surface of a deep fluid. *Journal of Applied Mechanics and Technical Physics*, 9(2):190–194, Mar 1968.

[127] D. E. Zmeev, F. Pakpour, P. M. Walmsley, A. I. Golov, W. Guo, D. N. McKinsey, G. G. Ihas, P. V. E. McClintock, S. N. Fisher, and W. F. Vinen. Excimers He_2^* as Tracers of Quantum Turbulence in ^{4}He in the $T = 0$ Limit. *Phys. Rev. Lett.*, 110:175303, Apr 2013.

[128] W. H. Zurek. Cosmological experiments in superfluid helium? *Nature*, 317(6037):505–508, 1985.